

2014

Assessing change in the Earth's land surface albedo with moderate resolution satellite imagery

<https://hdl.handle.net/2144/15403>

Downloaded from DSpace Repository, DSpace Institution's institutional repository

BOSTON UNIVERSITY
GRADUATE SCHOOL OF ARTS AND SCIENCES

Dissertation

**ASSESSING CHANGE IN THE EARTH'S LAND SURFACE ALBEDO
WITH MODERATE RESOLUTION SATELLITE IMAGERY**

by

QINGSONG SUN

B.S., Qingdao Technological University, 2006
M.S., Beijing Normal University, 2010

Submitted in partial fulfillment of the
requirements for the degree of
Doctor of Philosophy

2014

Approved by

First Reader

Crystal Schaaf, Ph.D.
Research Professor of Earth & Environment

Second Reader

Alan Strahler, Ph.D.
Professor of Earth & Environment

Third Reader

Curtis Woodcock, Ph.D.
Professor of Earth & Environment

Fourth Reader

Nathan Phillips, Ph.D.
Professor of Earth & Environment

Fifth Reader

Feng Gao, Ph.D.
Research Physical Scientist
US Dept. of Agriculture, USDA-ARS Hydrology and Remote Sensing
Laboratory

ACKNOWLEDGMENTS

I would like to express my deep appreciation to Dr. Crystal Schaaf, for the excellent guidance and great points she provided to me. I would like to thank Dr. Alan Strahler, for helping me to develop my background in Remote Sensing. I would also like to thank my committee members, Dr. Curtis Woodcock, Dr. Nathan Phillips, and Dr. Feng Gao, for their thought-provoking suggestions.

I would like to thank Dr. Zhuosen Wang, who provided me with suggestions and assessment data. I would like to thank Dr. Feng Zhao and Dr. Qingling Zhang, who contributed to the early version of the gap-filling code. I would also like to thank Dr. Yanmin Shuai, Dr. Xiaoyuan Yang, Dr. Tian Yao, Dr. Yun Yang, Zhan Li, JiHyun Kim, Angela Erb, Ian Paynter, Eddie Saenz, Yan Liu, and Shabnam Rouhani, for their feedback on various aspects of this project.

Finally, I would like to thank my parents, and my sisters, because they were there for me in so many ways. At the end I would like to thank my wife, who has always been my support while I pursued this final degree.

**ASSESSING CHANGE IN THE EARTH'S LAND SURFACE ALBEDO
WITH MODERATE RESOLUTION SATELLITE IMAGERY**

QINGSONG SUN

Boston University Graduate School of Arts and Sciences, 2014

Major Professor: Crystal Schaaf, Research Professor of Earth & Environment

ABSTRACT

Land surface albedo describes the proportion of incident solar radiant flux that is reflected from the Earth's surface and therefore is a crucial parameter in modeling and monitoring attempts to capture the current climate, hydrological, and biogeochemical cycles and predict future scenarios. Due to the temporal variability and spatial heterogeneity of land surface albedo, remote sensing offers the only realistic method of monitoring albedo on a global scale. While the distribution of bright, highly reflective surfaces (clouds, snow, deserts) govern the vast majority of the fluctuation, variations in the intrinsic surface albedo due to natural and human disturbances such as urban development, fire, pests, harvesting, grazing, flooding, and erosion, as well as the natural seasonal rhythm of vegetation phenology, play a significant role as well. The development of times series of global snow-free and cloud-free albedo from remotely sensed observations over the past decade and a half offers a unique opportunity to monitor and assess the impact of these alterations to the Earth's land surface.

By utilizing multiple satellite records from the MODerate-resolution Imaging Spectroradiometer (MODIS), the Multi-angle Imaging Spectroradiometer (MISR) and the Visible Infrared Imaging Radiometer Suite (VIIRS) instruments, and developing

innovative spectral conversion coefficients and temporal gap-filling strategies, it has been possible to utilize the strengths of the various sensors to improve the spatial and temporal coverage of global land surface albedo retrievals. The availability of these products is particularly important in tropical regions where cloud cover obscures the forest for significant periods. In the Amazon, field ecologists have noted that some areas of the forest ecosystem respond rapidly with foliage growth at the beginning of the dry season, when sunlight can finally penetrate fully to the surface and have suggested this phenomenon can continue until reductions in water availability (particularly in times of drought) impact the growth cycle. While it has been difficult to capture this variability from individual optical satellite sensors, the temporally gap-filled albedo products developed during this research are used in a case study to monitor the Amazon during the dry season and identify the extent of these regions of foliage growth.

TABLE OF CONTENTS

ACKNOWLEDGMENTS	iv
ABSTRACT.....	v
TABLE OF CONTENTS.....	vii
LIST OF TABLES	ix
LIST OF FIGURES	x
LIST OF ABBREVIATIONS.....	xvi
1. INTRODUCTION	1
2. GLOBAL GAP-FILLED SNOW-FREE LAND SURFACE BRDF PRODUCTS FOR MODELING AND ASSESSING THE IMPACT OF CHANGE IN THE EARTH'S LAND SURFACE ALBEDO	7
2.1 MODIS MCD43D Product	7
2.2 Methods.....	9
2.3 Assessment.....	19
2.4 Discussion.....	26
3. NARROW TO BROAD BAND CONVERSIONS BASED ON SATELLITE HYPER SPECTRAL DATA	28
3.1 Data	28
3.2 Methods.....	31
3.3 Results.....	35

3.4	Assessment.....	37
3.5	Discussion.....	56
4.	DATA FUSION OF MODIS, MISR, AND VIIRS	58
4.1	Data.....	59
4.2	Methods.....	60
4.3	Discussion.....	63
4.4	Conclusion	79
5.	ASSESSMENT OF THE IMPACT OF CHANGES IN THE INTRINSIC LAND SURFACE ALBEDO	81
5.1	Data.....	82
5.2	Discussion.....	84
5.3	Conclusion	96
6.	SUMMARY	98
	BIBLIOGRAPHY.....	102
	CURRICULUM VITAE.....	111

LIST OF TABLES

Table 1 Comparison between the new (upper) and the current operational (lower) N2B	35
Table 2 selected flux network sites	39
Table 3 Spectral specifications of MODIS, MISR, and VIIRS	60
Table 4 Statistics of MODIS (Terra)-MISR data fusion.....	64
Table 5 Statistics of the MODIS (Aqua)-VIIRS data fusion	69

LIST OF FIGURES

Figure 1 Seasonality of the three BRDF parameters for different land cover types. Green: Deciduous Broadleaf Forest, blue: Mixed Forest, red: Open Shrublands, yellow: Grasslands. X axis: day of year. Values are averaged from a 5 degree latitude band at 55 °N from MCD43D near infrared (NIR) band BRDF parameters, 2010. 10

Figure 2 Cloud contamination in Amazon and West Africa. The picture is RGB composite of White Sky Albedo (WSA) band 1 (red), band 4 (green), and band 3 (blue) for day of year (DOY) 249, 2010. 13

Figure 3 Mask for the outlier removal algorithm. The colors indicate number of high quality pixels in the 76-period time series: black 0, red 1-25, blue 26-50, green 51-76. Data for this picture are from QA in Red band, 2010..... 15

Figure 4 Outlier removal algorithm effect on the Amazon. Column 1: RGB composite of WSA DOY 233, 2010. Column 2: QA of the WSA for red band (green: high-quality retrievals, maroon: temporally filled values, blue: spatially fitted values, yellow: spatially smoothed). First row: no outlier removal method has been applied. Middle row: outlier removal has been applied only for the lower quality values (no mask is used). Last row: outlier removal applied with the mask. 16

Figure 5 Outlier removal algorithm effect for Africa. (a) Before removal, (b) after removal. DOY 225, 2010..... 17

Figure 6 Gap-filled, cloud-free, seasonal snow free, true color composite of 30arc second WSA, DOY 193, 2010. 19

Figure 7 QA flags associated with the gap-filled image above for band 1 (green: high-quality retrievals, maroon: temporally filled values, blue: spatially fitted values, yellow: spatially smoothed, magenta: spatial fill between 80N-90N, and coral: linear fit between 70-82SZA).	19
Figure 8 Original high quality values VS (a): temporal fitted, (b): spatial fitted, (c): spatially smoothed, and (d): histogram of the gap-filled data minus the original data (NIR band, 2010).	21
Figure 9 Mean of original and gap-filled WSA in NIR band of DOY 001, 2010 as a function of latitude. X: latitude. Y primary: albedo (for lines and points), secondary: number of pixels in units of millions (for areas). Greens: original in MCD43D, reds: gap-filled	23
Figure 10 same as Figure 9 but for DOY 193, 2010.....	23
Figure 11 Mean of original and gap-filled WSA in NIR band in 2010 as a function of day of year. Number of pixel is in unit of 10,000.....	24
Figure 12 same as Figure 11 but for Mixed Forest, and number of pixels in unit of millions.	24
Figure 13 same as Figure 11 but for Open Shrublands, and number of pixels in unit of millions.	25
Figure 14 same as Figure 11 but for Grasslands, and number of pixels in unit of millions.	25
Figure 15 BRDF shapes at the principle plane for the original high quality (green) vs. the gap-filled (red) from a selected pixel in NIR band. SZN is set to 30 °.....	26

Figure 16 Spectral responses for MODIS band 1 (in red color) and Hyperion band 27-32 (green). The Hyperion spectral response function is modelled by a Gaussian function of eq. (10).....	29
Figure 17 Vertical streaks in the Hyperion data (left), and the data after streak removal (right)	31
Figure 18 Regression result for VIS	36
Figure 19 Regression result for NIR.....	37
Figure 20 Regression result for Shortwave.....	37
Figure 21 Correlations between ground albedo and MODIS SW Albedo calculated by the new N2B (left) and the current operational N2B (right).....	40
Figure 22 Scatter plot of the shortwave albedo calculated by the new N2B versus that calculated by the current N2B.....	41
Figure 23 Ground shortwave albedo VS. MODIS N2B albedo.....	56
Figure 24 True color composite of nadir MISR BRF accumulated between 185 and 200, 2001.....	64
Figure 25 True color composite of MISR derived WSA (full inversion only) for 185, 2001.....	65
Figure 26 QA flags for MODIS Terra-only (top) and MODIS-MISR (middle), and synergistic flags (bottom) for MODIS band 1. QA Green: full inversion, Red: magnitude inversion. Synergistic flags Green: <i>a priori</i> synergism, Red: direct synergism. Left column: DOY 025, right: 185.	66
Figure 26 continued for MODIS band 2.	67

Figure 26 continued for MODIS band 4	68
Figure 27 Observations of MODIS Aqua (plus) and VIIRS (circle) accumulated between 185 and 200, 2012. Red stars are sun positions. Left is selected from tile h19v07, and right is tile h12v03	69
Figure 28 QA and synergistic flags for MODIS-VIIRS band 1. Left: DOY 025, right: 185	70
Figure 28 continued for MODIS band 2	71
Figure 28 continued for MODIS band 3	72
Figure 28 continued for MODIS band 4	73
Figure 28 continued for MODIS band 5	74
Figure 28 continued for MODIS band 6	75
Figure 28 continued for MODIS band 7	76
Figure 29 WSA NIR (band 2) derived from MODIS Aqua-only for 025, 2012	77
Figure 30 WSA NIR derived from MOIS Aqua and VIIRS for 025, 2012	77
Figure 31 QA flags for Terra-Aqua (top) and Terra-Aqua-VIIRS (bottom) BRDF retrieval for band 2. Left: 025, 2012, Right: 185, 2012.....	79
Figure 32 Location of the tiles h11v09 and h12v09	82
Figure 33 Monthly composite of daily V006 MCD43A NBAR at a solar zenith angle of 30 degree for tiles h11v09 & h12v09 for DOY 151-180 (June), 2005.....	83
Figure 34 Monthly composite of daily V006 MCD43A NBAR at a solar zenith angle of 30 degree for tiles h11v09 & h12v09 for DOY 181-210 (July), 2005	83

Figure 35 Monthly composite of daily V006 MCD43A NBAR at a solar zenith angle of 30 degree for tiles h11v09 & h12v09 for DOY 211-240 (August), 2005.....	84
Figure 36 Monthly composite of daily V006 MCD43A NBAR at a solar zenith angle of 30 degree for tiles h11v09 & h12v09 for DOY 241-270 (Sept.), 2005	84
Figure 37 Δ EVI of July – June.....	85
Figure 38 Δ EVI of August – June.....	86
Figure 39 Δ EVI of September – June	86
Figure 40 Subset of study area.....	88
Figure 41 Number of high quality retrievals of V005 MCD43D through the year 2005 .	88
Figure 42 Longitude EVI profiles of the gap-filled dataset for Amazon forests. Figure 41 is projected to the XY plane, and the Amazon NBAR map is projected to the YZ plane for reference. From the XY plane we can roughly see how many dry months are in the year for a profile, and from the YZ plane we can see where a profile is located and what forest pixels it crosses.	89
Figure 43 Latitude EVI profiles of Amazon forests	90
Figure 44 Δ EVI of 2004 – 2003 for longitude profiles.....	92
Figure 45 Δ EVI of 2005 – 2004 for longitude profiles.....	92
Figure 46 Δ EVI of 2006 – 2005 for longitude profiles.....	93
Figure 47 Δ EVI of 2007 – 2006 for longitude profiles.....	93
Figure 48 Time series of average EVI of the entire Amazon forest of the gap filled dataset	94

Figure 49 Monthly precipitation rate for Amazon. Data are from The Tropical Rainfall Measuring Mission (TRMM) Monthly 0.5 x 0.5 3A12 (v007). Each time period is averaged from area between 5 °N - 15 °S, and 75 °W - 50 °W.....	94
Figure 50 Precipitation 2005 JAS standardized anomalies. Data are from TRMM monthly precipitation data (3B43) of 2001-2005.....	95
Figure 51 Time series of average EVI of the drought-stricken pixels.....	95
Figure 52 Time series of average WSA in NIR band of the entire Amazon forest of the gap filled dataset.	96

LIST OF ABBREVIATIONS

AOD	Aerosol Optical Depth
AVHRR	Advanced Very High Resolution Radiometer
BHR	Bi-Hemispherical Reflectance
BOA	Bottom-of-Atmosphere
BRF	Bidirectional Reflectance Factor
BRDF	Bidirectional Reflectance Distribution Function
BSA	Black Sky Albedo
BSRN	Baseline Surface Radiation Network
CCP	Canadian Carbon Program
CMG	Climate Modeling Grid
DHR	Directional-Hemispherical Reflectance
DOY	Day of Year
EVI	Enhanced Vegetation Index
FWHM	Full Width Half Maximum
IGBP	International Geosphere-Biosphere Programme
IMECC	Infrastructure for Measurements of the European Carbon Cycle
IPCC	Intergovernmental Panel on Climate Change
ITCZ	Inter-Tropical Convergence Zone
LAI	Leaf Area Index
LTER	Long Term Ecological Research
MODIS	Moderate-Resolution Imaging Spectroradiometer

MISR.....	Multi-angle Imaging SpectroRadiometer
N2B.....	Narrow-to-Broadband
NBAR.....	Nadir-BRDF Adjusted Reflectance
NIR.....	Near infrared
POLDER.....	POLarization and Directionality of the Earth's Reflectances
QA.....	Quality Assessment
RMSE.....	Root Mean Square Error
RTLSR.....	RossThick-LiSparseReciprocal
SOM.....	Space-Oblique Mercator
SURFRAD.....	Surface Radiation Network
SW.....	Short Wave
SZA.....	Solar Zenith Angles
TOA.....	Top-of-Atmosphere
VIIRS.....	Visible Infrared Imaging Radiometer Suite
WSA.....	White Sky Albedo

CHAPTER ONE

1. INTRODUCTION

Land surface albedo, the proportion of incident radiant flux that is reflected, is used to describe the Earth's radiative energy budget and the exchange of radiative energy between the atmosphere and the land surface. The energy absorbed by the Earth affects surface temperature, photosynthesis, plant growth, evaporation, snow melt, etc. Thus, albedo is a crucial climate parameter and is therefore required by climate, biogeochemical, hydrological, and weather forecast models at a variety of spatial and temporal scales (Charney et al., 1977; Dickinson and Hanson, 1984; Wang et al., 2004; Lacaze et al., 2006; Rahman et al., 1993; Martonchik 1997, 2002; Morcrette et al., 2008; Schaaf et al., 2002, 2008, 2011). The role of disturbance and land use change, while recognized as a potentially important impact on radiative forcing in the newly released 5th Assessment Report of the Intergovernmental Panel on Climate Change (IPCC 2013), is also recognized as a poorly understood factor requiring further research.

Remote sensing provides the only viable way to capture land surface albedo on a global scale. As multi-angle data from remote sensing sensors such as AVHRR (Advanced Very High Resolution Radiometer), POLDER (POLarization and Directionality of the Earth's Reflectances), MISR (Multi-angle Imaging SpectroRadiometer), and MODIS (Moderate-Resolution Imaging Spectroradiometer), have become available, the retrieval of remotely sensed measures of reflectance anisotropy has been adopted as the most flexible method to accurately derive surface albedo (Strugnell and Lucht, 2001; Strugnell et al., 2001; Hu et al., 2000; d'Entremont et

al., 1999; Privette et al., 1997; Leroy et al., 1997; Schaaf et al., 2002, 2008, 2011; Lucht et al., 2000a; Wanner et al., 1997).

MODIS is capable of providing multiple angular observations to sample the Bidirectional Reflectance Distribution Function (BRDF) of each location on the Earth's surface. Directional observations accumulated during a 16-day period are used to derive fine resolution (500m) land surface BRDF, albedo, and NBAR (Nadir-BRDF Adjusted Reflectance) products (Schaaf et al., 2002; 2011), which have been validated by various rigorous assessment efforts (Lucht et al., 2000; Jin et al., 2003a, b; Salomon et al., 2006; Román et al., 2009; Cescatti et al., 2012; Wang et al., 2012; 2014). The MODIS BRDF products can be used to establish surface vegetation structure and roughness (Hill et al., 2008; 2011a, b; Chopping et al., 2010; 2011; Jiao et al., 2014), while the albedo product been used widely in modeling communities (Myhre et al., 2005; Roesch et al., 2004; Wang et al., 2004; Oleson et al., 2003; Zhou et al., 2003; Morcrette et al., 2008; Lawrence and Chase 2007, 2009, 2010). The NBAR and vegetation indices derived from NBAR are the primary inputs to the MODIS land cover and phenology products and are also being used for regional crop and range monitoring applications.

However, data gaps caused by cloud cover or ephemeral snow cover have reduced the application of the operational MODIS anisotropy products. In the Inter-Tropical Convergence Zone (ITCZ) dominated regions, clouds may last for several months and cause major gaps in the anisotropy products. Clouds in India and Southeast Asia during

monsoon seasons and seasonal snow at high latitudes can also contaminate the BRDF/albedo products and limit their utilizations in modeling studies.

Therefore, the purpose of this research is to assess the variation in intrinsic albedo on the Earth's albedo over the past decade and a half by developing and applying the highest quality global cloud-free, snow-free BRDF/albedo/NBAR products possible from remotely sensed sources. Although the development of these cloud-free, snow-free albedo products from optical sensors remains a difficult challenge, this effort will primarily utilize the MODIS 30arc second anisotropy product, augmented where possible with other contemporaneous multi-angle derived values such as MISR and more recently VIIRS. Previous more spatially coarse resolution gap-filling efforts have been made on the MODIS V004 albedo product (Moody et al., 2005, 2008) rather than the underlying BRDF product. A similar approach to albedo gap-filling was also applied to the 0.05degree (3 arc minute) MODIS V005 Climate Modeling Grid product (Zhang, 2009). In this research, we apply temporal fitting techniques based on yearly vegetation phenology and spatial fitting techniques to the global 30arc-second V005 MCD43D BRDF product to compensate for missing data and to estimate snow-free situations.

Global gap-filled snow-free BRDF parameters, two intrinsic albedos of White Sky Albedo and Black Sky albedo (at local solar noon), and the Nadir BRDF-Adjusted Reflectance (NBAR) are provided. Actual albedo (or blue sky albedo) can be further produced from the gap-filled White Sky Albedo and Black Sky Albedo combined with aerosol optical depth (AOD) information, such as the MOD04 aerosol product. The AOD

can be used to simulate the fraction of diffuse downward flux by 6S (Second Simulation of a Satellite Signal in the Solar Spectrum). If the fraction of diffuse downward flux is known, the blue sky albedo can be calculated by equation (1)

$$a_{blue}(\theta, \Lambda) = f_d(\theta, \Lambda)a_{ws}(\Lambda) + (1 - f_d(\theta, \Lambda))a_{bs}(\theta, \Lambda) \quad (1)$$

where $a_{blue}(\theta, \Lambda)$ is the blue sky albedo at SZA θ for band Λ ; a_{ws} is the white sky albedo; a_{bs} is the black sky albedo at SZA θ ; f_d is the fraction of diffuse downward flux. This equation treats the downwelling diffuse radiation as isotropic. Román et al. (2010) improved this formulation by incorporating anisotropic diffuse illumination and multiple scattering between the surface and atmosphere, which has been shown to be more accurate than eq. (1), especially for snow covered (bright) land surface. Note that this gap-filled product remains a cloud-free product and should not be used under extremely turbid atmospheric conditions.

To further improve the broadband albedo in the gap-filled dataset, new narrow-to-broad band conversion coefficients has been developed based on satellite hyperspectral data. The operational coefficients were derived by Liang et al. (1999 and 2000) and are based mainly on laboratory acquired spectra of several land cover types. Since the laboratory spectra are usually collected from a single leaf, they may not represent the spectral characteristics of a pixel at remote sensing scales. The Hyperion onboard EO-1 has been providing hyperspectral data since 2001, as such, it is possible to develop new satellite-based narrow-to-broad band coefficients to compensate for the limitations of laboratory spectra.

Combining data from multiple sensors is another strategy that can improve the BRDF retrievals (and thus increase the number of high quality observations available for a gap filled product) by adding complementary viewing geometries (Jin et al., 2002; Samain et al., 2006). Jin et al. (2002) developed a synergistic approach of integrating BRDF parameters derived from MISR as a priori information with MODIS observations to derive a posteriori BRDF parameters. This method can reduce the relative bidirectional reflectance factor (BRF) prediction error by up to 10% (Jin et al., 2002). In this research, observations of MODIS, MISR and VIIRS (Visible Infrared Imaging Radiometer Suite) will be fused using similar methods to improve the data quality and increase the number of high quality pixels, particularly for the time period when only MODIS-Terra information was available (2000-2002) and as a contingency the future when Terra observations are no longer available (~2017 - 2020) .

Once these enhanced quality BRDF products are in place, assessments of the primary intrinsic land surface albedo and vegetation phenology variations that have occurred over the past decade and a half can be undertaken. This gap-filled product represents a major step forward in many respects. The gap-filled dataset provides not only the intrinsic albedo of the land surface, but also the gap-filled BRDF parameters. This allows modelers to calculate albedo and surface reflectance at any desired viewing angle and solar zenith angle and thus further derive vegetation indices. The higher temporal resolution of the gap-filled dataset (8-day as opposed to 16-day) provides modelers increased confidence in the product and the flexibility of computing albedo at interim periods of only a few days. And the higher spatial resolution (30 arc second) than

previous gap-filled datasets (1 arc min, Moody et al., 2005; 3 arc min, Zhang 2009) is closer to the scale of ground measurements, and makes it more useful to capture the dynamics of the change on the Earth's surface.

Due to the excessive cloudiness, optical satellite data are always spatially and temporally incomplete for Amazon. And because of this lack of available high quality satellite, many aspects of the dynamics of the Amazon forest are under debates (Huete et al., 2006; Brando et al., 2010; Xiao et al., 2006; Myneni et al., 2007, Saleska et al., 2007, Samanta et al., 2010). In this research, we will explorer using the gap-filled BRDF dataset to monitor the phenology change of the Amazon forests.

CHAPTER TWO

2. GLOBAL GAP-FILLED SNOW-FREE LAND SURFACE BRDF PRODUCTS FOR MODELING AND ASSESSING THE IMPACT OF CHANGE IN THE EARTH'S LAND SURFACE ALBEDO

Land surface albedo is required globally by climate modeling, biogeochemical modeling, and numerical weather prediction communities (Charney et al., 1977; Dickinson and Hanson, 1984; Wang et al., 2004; Morcrette et al., 2008; Lacaze et al., 2006; Rahman et al., 1993; Martonchik 1997, 2002; Schaaf et al., 2002, 2008, 2011). However, data gaps caused by cloud cover or ephemeral snow cover have limited the application of the albedo product. In this effort, gap-filling techniques similar to those previously applied to the MODIS albedo (Moody et al., 2005, 2008) and MODIS Leaf Area Index (LAI) products (Gao et al., 2008) are applied to the MODIS MCD43D anisotropy product to develop a spatially and temporally complete global snow-free BRDF dataset to monitor and assess changes in the Earth's intrinsic land surface albedo.

2.1 MODIS MCD43D Product

The MODIS is capable of providing multiple angular observations to sample the BRDF of each location on the entire Earth's surface. The operational MODIS BRDF/Albedo algorithm (eq. (2)) makes use of a linear combination of an isotropic parameter and two kernels (Roujean et al., 1992): the RossThick kernel which is derived from radiative transfer models (Ross, 1981), and the LiSparseReciprocal kernel which is based on surface scattering and geometric optical mutual shadowing (Li and Strahler, 1992).

$$R(\theta, \nu, \phi, \Lambda) = f_{iso}(\Lambda) + f_{geo}(\Lambda)k_{geo}(\theta, \nu, \phi) + f_{vol}(\Lambda)k_{vol}(\theta, \nu, \phi) \quad (2)$$

Where R represents the surface reflectance in wave band Λ ; θ, ν, ϕ are the solar zenith, view zenith and relative azimuth angles; k_{geo} and k_{vol} are the LiSparseReciprocal and RossThick kernels; and $f_{iso}(\Lambda)$, $f_{geo}(\Lambda)$, and $f_{vol}(\Lambda)$ are the kernel weights, which are to be derived by inverting the model against MODIS multiple angular directional observations. Once the three kernel weights have been retrieved, reflectance $R(\theta, \nu, \phi, \Lambda)$ at any view-solar angle combinations can be calculated by equation (2). Integrating the R over all view angles, a directional-hemispherical reflectance (DHR, or black-sky albedo) can be derived by equation (3).

$$a_{bs}(\theta, \Lambda) = \frac{1}{\pi} \int_0^{2\pi} \int_0^{\pi/2} R(\theta, \nu, \phi, \Lambda) \sin(\nu) \cos(\nu) d\nu d\phi \quad (3)$$

Further integration of the $a_{bs}(\theta, \Lambda)$ over all solar zenith angles results in a bi-hemispherical reflectance (BHR, or white sky albedo) using equation (4).

$$a_{ws}(\Lambda) = 2 \int_0^{\pi/2} a_{bs}(\theta, \Lambda) \sin(\theta) \cos(\theta) d\theta \quad (4)$$

This RossThick-LiSparseReciprocal (RTLSR) model has been tested and works well with MODIS reflectance data for deriving land surface anisotropy of various land covers (Lucht et al., 2000; Maignan et al., 2004).

The MOD43D product (V005) provides the three kernel weights for the RossThick-LiSparseReciprocal model at a 30arc second resolution in Climate Modeling Grid (CMG) projection every 8 days based on a 16-day retrieval period (Schaaf et al., 2002, 2008). Data are available for 7 MODIS land bands (0.47 μm , 0.55 μm , 0.67 μm ,

0.86 μm , 1.24 μm , 1.64 μm , 2.1 μm) and 3 broad bands (the shortwave band (0.3-5.0 μm), a visible band (0.3 μm -0.7 μm) and a near-infrared band (0.7-5.0 μm)). Quality Assessment (QA) and snow status are provided for each pixel to indicate inversion quality and snow condition.

2.2 Methods

Temporal fit

The software package, TIMESAT was developed to analyze time series remote sensing data (Jonsson and Eklundh, 2002, 2004). The asymmetric Gaussian fitting method in this package was used to produce spatially and temporally continuous MODIS LAI (Gao et al., 2008) based on yearly vegetation phenology. In this research, similar temporal fitting techniques have been applied to the MCD43D BRDF parameters to compensate for missing data and to estimate snow-free situations (Fang et al., 2007). Just as Albedo and NBAR, the three BRDF parameters also exhibit seasonality (Figure 1), which is the basis for fitting with the TIMESAT package.

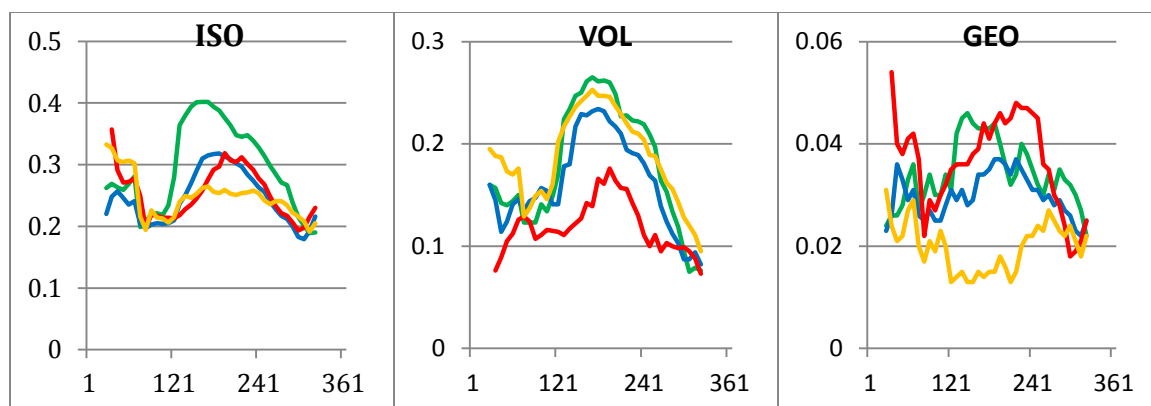


Figure 1 Seasonality of the three BRDF parameters for different land cover types. Green: Deciduous Broadleaf Forest, blue: Mixed Forest, red: Open Shrublands, yellow: Grasslands. X axis: day of year. Values are averaged from a 5 degree latitude band at 55° N from MCD43D near infrared (NIR) band BRDF parameters, 2010.

A total of 76 of the 8-day periods are used to form the time series for the temporal fit with 46 from the processing year of interest, 15 from the end of the previous year, and 15 from the beginning of the next year.

High quality data (QA = 0 or 1) drives the fit of the temporal curves. Data are weighted by their QA when the asymmetric Gaussian functions are applied. Pixels with ephemeral snow (detected by the snow flag of MCD43D34) are removed to generate a snow-free product. To avoid a TIMESAT failure due to insufficient high-quality data in the time series caused by cloud or ephemeral snow, a linear interpolation is employed to fill the no-data values. A low-quality QA is assigned to these interpolated values to make sure the fit is primarily driven by high quality data and the low quality data in the time series only serve as a first guess to condition the temporal fit. These low quality data will be replaced with the refined estimations from the asymmetric Gaussian functions. High-quality data from MCD43D are unchanged during the temporal fitting.

Most of the gaps (more than 97% of the available land pixels) can be filled with the temporal fit procedure. However, if there are very few valid values (for example one or two) in the entire 76 period time series, the temporal fit is not able to handle the gap filling and thus further spatial fits are applied to the remaining 2-3%.

Spatial fit

A spatial fit method is employed for the small regions of the world where a temporal curve cannot be generated due to seasonal or persistent cloud cover. In the spatial fit, mean value of the nearby pixels with the same land cover types is calculated and used as a basic shape for the phenology curve. The no-data pixels are then filled by this basic shape but adjusted by available data points in the time series (eq. (5) and (6)). This method can be only applied to pixels that have at least one valid value in the time series to adjust the mean phenology shape from nearby pixels. The International Geosphere-Biosphere Programme (IGBP) land cover of V005 MCD12Q1 re-projected to CMG grid and aggregated to 30 arc second is used as the classification map in the spatial fit

$$F = \sum_{i=1}^n V_i M_i W t_i / \sum_{i=1}^n M_i M_i W t_i \quad (5)$$

$$V_j = F * M_j \quad (j \in [1, 76 - n]) \quad (6)$$

Where F is adjusting factor, n is the number of available values in the time series, V_i is valid value in the time series, $W t_i$ is the weight of the value according to its QA, and M_i is the mean of nearby pixels. V_j is the gaps to be filled.

The mean of nearby pixels is calculated from pixels with the same land cover type within 1 degree latitude band centered by the latitude of the gap pixel. The yearly V005 MODIS land cover product MCD12Q1 (the IGBP layer) is used as the classification map.

Spatial smoothing

To ensure a gap-free product, a spatial smoothing method is applied to the pixels that still remain with no-data whatsoever after the temporal fit and spatial fit. In this step, the no-data pixels are filled by the mean value of nearby pixels with the same land cover type. The mean of nearby pixels is calculated by the same method mentioned in Spatial Fit.

SZA extension

The MCD43 product is not recommended for solar zenith angles (SZA) beyond 70 degrees. However the MODIS Atmosphere Team has a requirement for albedos at SZAs of up to 82 degree for their cloud properties product. Therefore the data for those areas that exceed the 70 degree SZA are filled linearly with temporal data from other 8-day retrievals at lower solar zenith angles.

Cloud contamination removal for ITCZ

In some regions, in particular Amazon and equatorial West Africa, the original V005 MCD43D was somewhat contaminated by residual cloud cover (Figure 2). This occurred when the 500m standard BRDF product (MCD43A1) is averaged and re-projected to form the 30arc second V005 MCD43D parameters. In the averaging process, the quality flag of the 30arc second average represents the majority flag of the underlying

500m pixels. This strategy works well in most parts of the world but in these ITCZ dominated regions of the world, there are so few high quality values that even pixels flagged as majority high quality may have some residual cloud contamination (three high quality pixels and one cloud contaminated poor quality pixel will still generate a slightly contaminated majority high quality value).

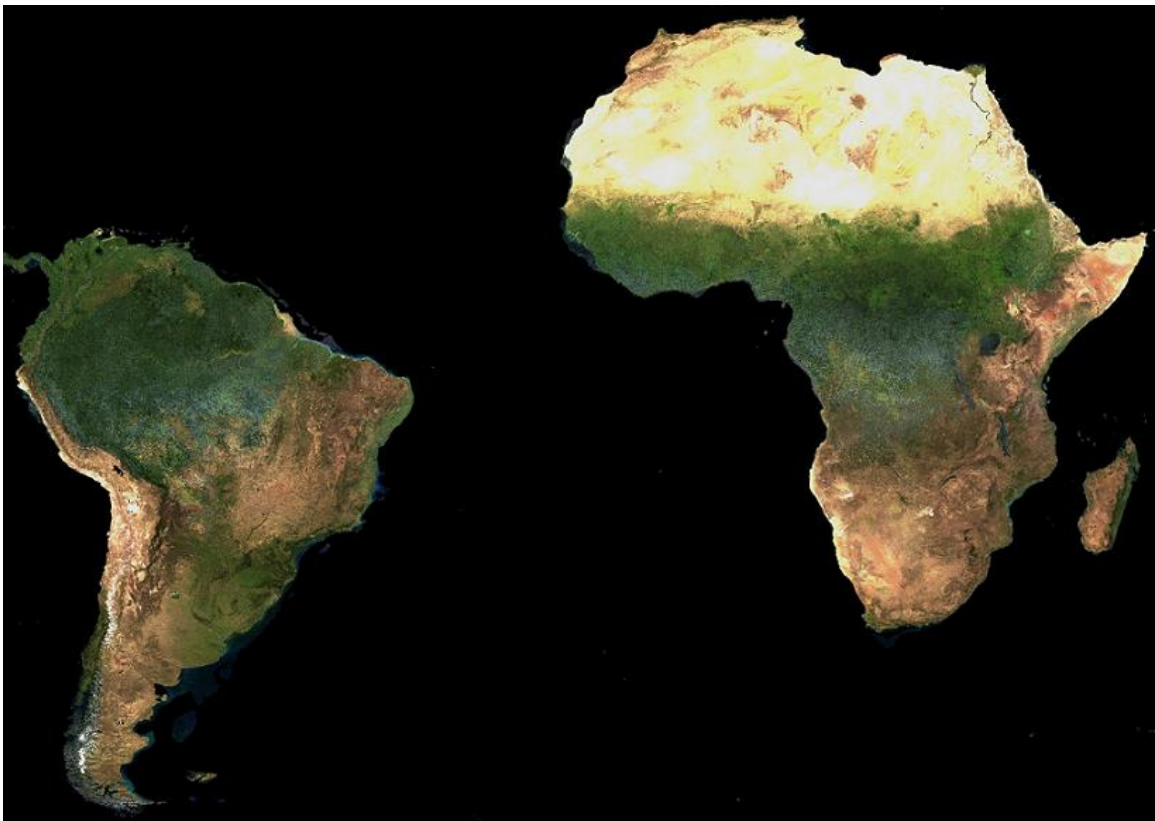


Figure 2 Cloud contamination in Amazon and West Africa. The picture is RGB composite of White Sky Albedo (WSA) band 1 (red), band 4 (green), and band 3 (blue) for day of year (DOY) 249, 2010.

An outlier removal algorithm (Leys, C., et al 2013) is applied on South America and Africa aimed to eliminate cloud contamination. To identify the ITCZ dominated regions, a mask is developed based on the number of high-quality pixels in the time series (Figure 3). Pixels with number of high quality values less than one-third (25) of the 76

time periods are considered as ITCZ dominated regions (red color in Figure 3) and are filtered by the outlier removal algorithm before getting into temporal fit. Because there are so few high quality pixels in this region, even a high quality flagged value in the V005 MCD43D is more likely to be contaminated by residual clouds, so the outlier removal algorithm is also applied on all the values including high quality values. By comparing with Figure 2, this region roughly overlaps with the cloud contaminated areas in Amazon and West Africa. Pixels with more than one-third but fewer than two-third (50) of high quality values in the time series are considered as ITCZ affected area (blue color). Since there are a few more high quality pixels available, fewer pixels are apt to be contaminated when averaging, therefore the algorithm checks outliers with a more conservative threshold for this region. Pixels with more than two-third of high quality values are considered not affected by the ITCZ and the outlier removal method is not applied here (green color).

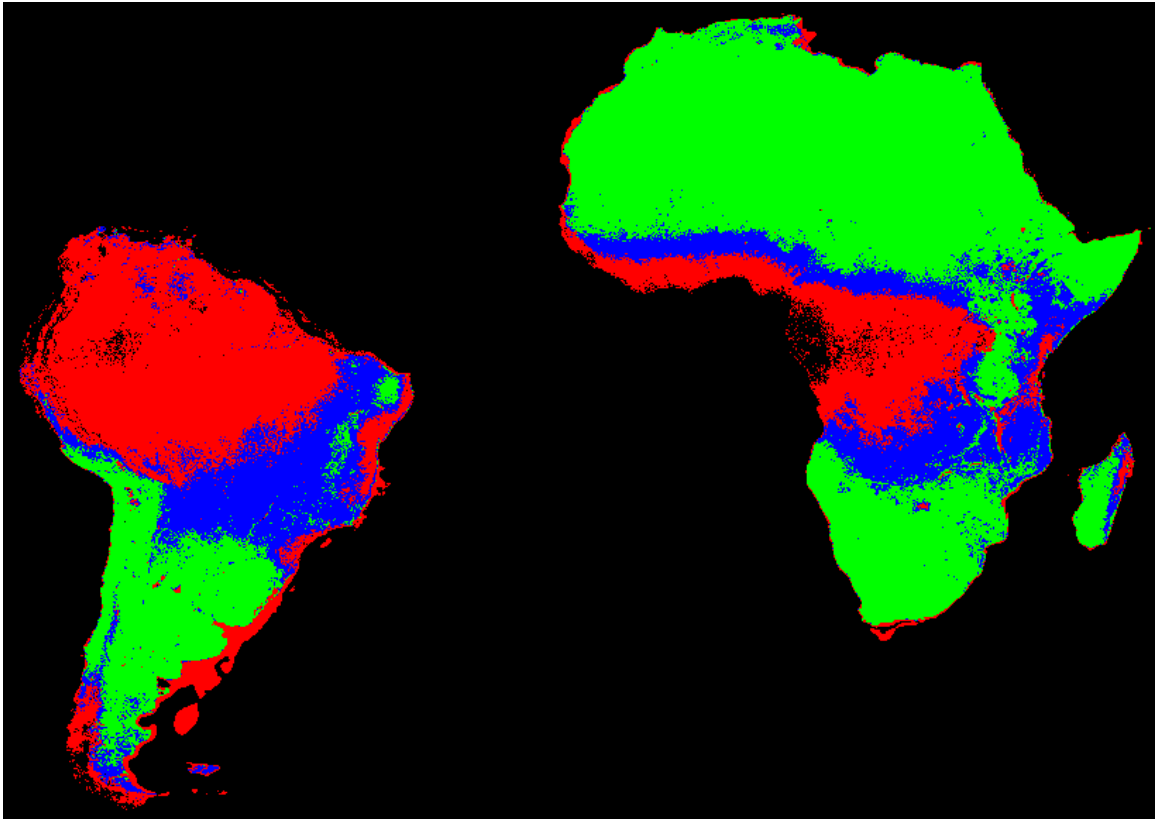


Figure 3 Mask for the outlier removal algorithm. The colors indicate number of high quality pixels in the 76-period time series: black 0, red 1-25, blue 26-50, green 51-76. Data for this picture are from QA in Red band, 2010.

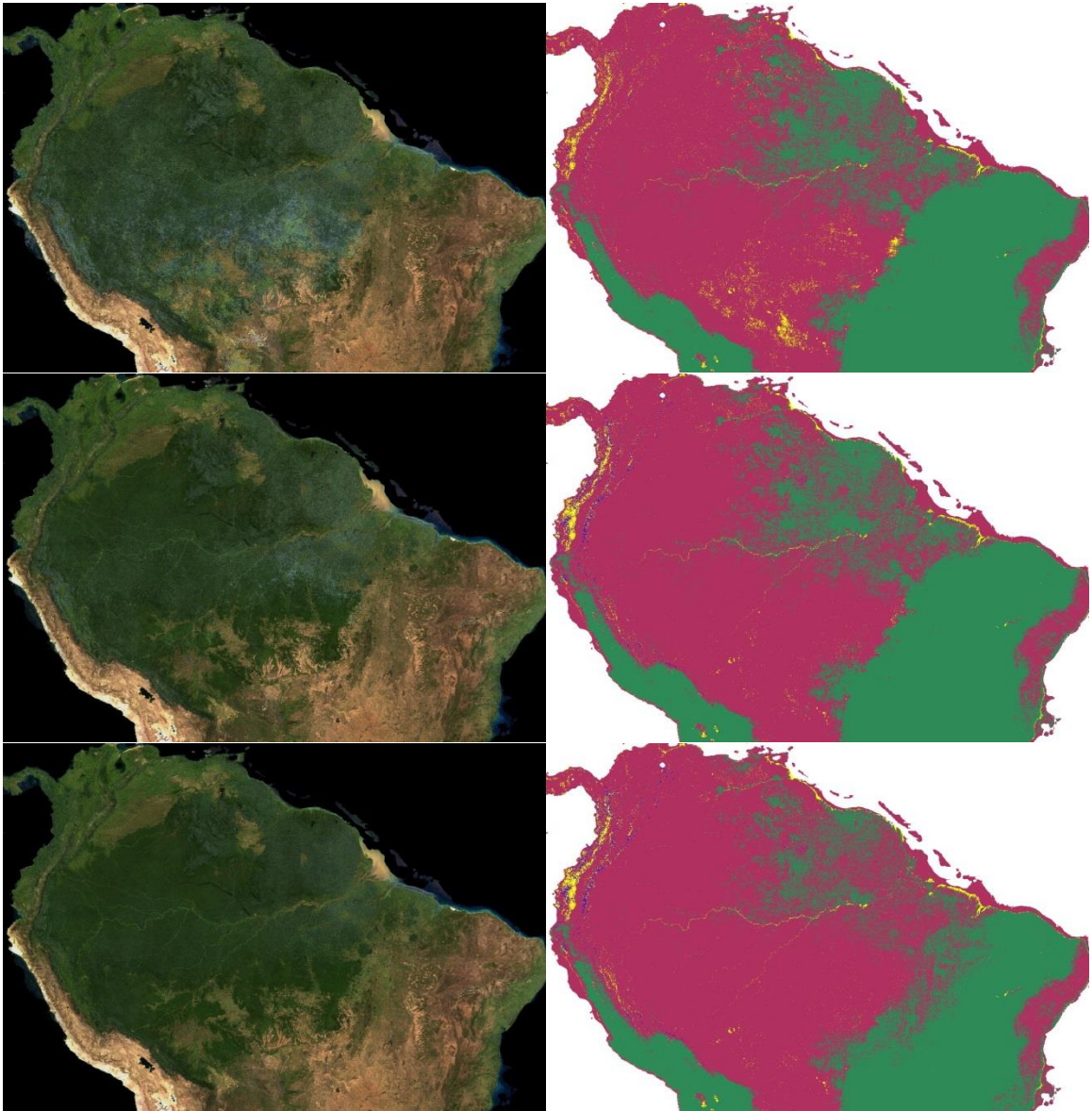


Figure 4 Outlier removal algorithm effect on the Amazon. **Column 1:** RGB composite of WSA DOY 233, 2010. **Column 2:** QA of the WSA for red band (green: high-quality retrievals, maroon: temporally filled values, blue: spatially fitted values, yellow: spatially smoothed). **First row:** no outlier removal method has been applied. **Middle row:** outlier removal has been applied only for the lower quality values (no mask is used). **Last row:** outlier removal applied with the mask.



Figure 5 Outlier removal algorithm effect for Africa. (a) Before removal, (b) after removal. DOY 225, 2010.

Figure 4 and Figure 5 show the performance of the outlier removal method.

Without removing outliers, we can see obvious cloud contamination in the Amazon for the WSA at DOY 233, 2010 (Figure 4, first row). If only outliers with low quality flags are removed, the cloud contamination can still be detected in some areas (Figure 4, middle row). By using the masked outlier removal method we can see that the obvious clouds are cleared and the other areas are not affected significantly (the color tone of the uncontaminated areas does not change significantly from the original picture) (Figure 4, last row).

By comparing the QA pictures in Figure 4 we see (in a qualitative sense) that there are more spatially smoothed pixels in the no-outlier-removed scene. This is because spatial smoothing is the last of the gap-filling procedures, and at that point a WSA value check is performed and if a pixel's WSA is three times larger than nearby mean WSA, this pixel will be filled with the spatial smoothing method. Cloud contamination can cause this happen and make more spatially smoothed pixels. From the following assessment, we demonstrate that the temporal fit is much more accurate than spatial smoothing so we conclude that the outlier removal algorithm is indeed improving the

gap-filled data quality. And we can also track how many high quality pixels are removed by comparing the QA maps. Almost all the high quality values which are removed are from the ITCZ dominated area. The outlier removal algorithm uses more conservative criteria for high quality values to maximize the preservation of high quality values from the MCD43D.

Due to a processing error, the entire region between 80N and 90N in the V005 MCD43D was not reprocessed. Therefore, for the convenience of users, we fill that region with the mean values of the land cover types computed from the region between 70N-80N.

As a result, we are able to generate a global gap-filled, snow-free BRDF/Albedo/NBAR with QA (Figure 6 and Figure 7) at 30 arc second spatial resolution and 8-day temporal resolution in 7 MODIS bands (0.47um, 0.55um, 0.67um, 0.86um, 1.24um, 1.64um, 2.1um), and three broad bands (0.3um -0.7um, 0.7-5.0um, and 0.3-5.0um) for the entire time period from 2000 to 2013.

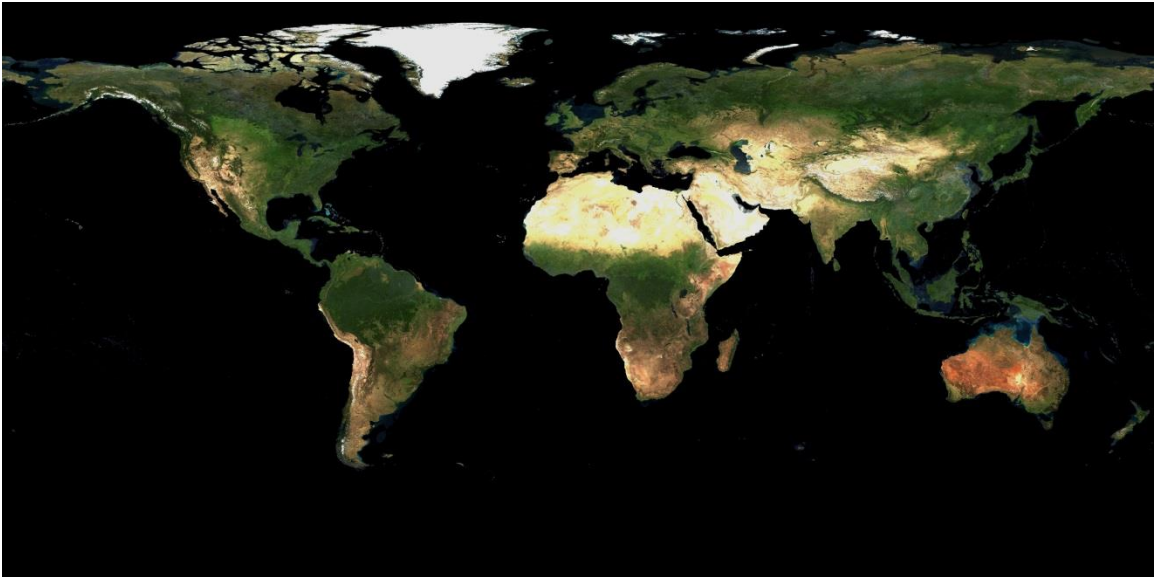


Figure 6 Gap-filled, cloud-free, seasonal snow free, true color composite of 30arc second WSA, DOY 193, 2010.

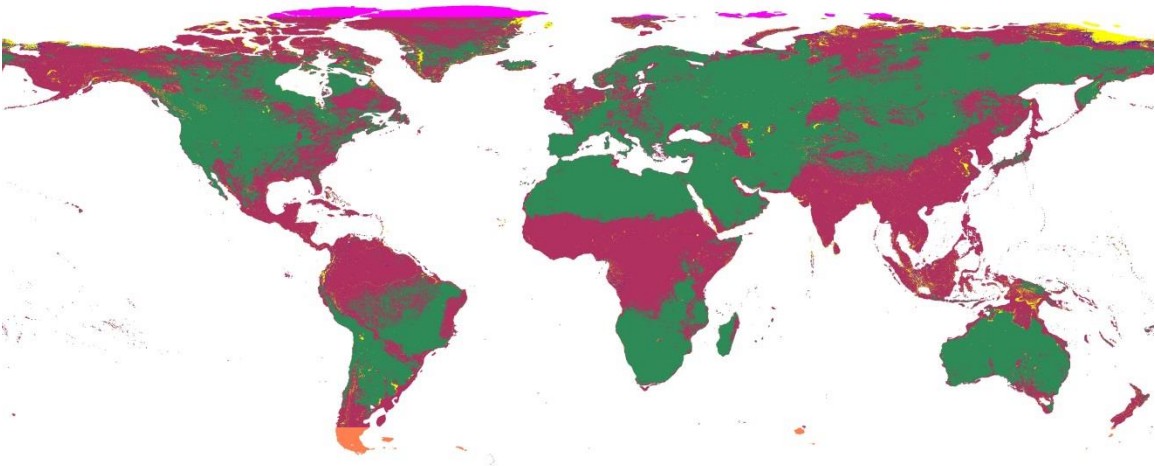


Figure 7 QA flags associated with the gap-filled image above for band 1 (green: high-quality retrievals, maroon: temporally filled values, blue: spatially fitted values, yellow: spatially smoothed, magenta: spatial fill between 80N-90N, and coral: linear fit between 70-82SZA).

2.3 Assessment

To estimate the accuracy of these gap-filling methods, 2% of all the land pixels are randomly selected and for each selected pixel one high-quality value is randomly taken

out from the time series and replaced with a fill value. The gap-filling techniques are then applied and WSA calculated from the gap-filled parameters are compared with the original high-quality values that been removed. The band 2 (NIR) of 2010 is chosen for this assessment because it should have the largest errors due to the large value variations for vegetation in this channel.

The temporal fit shows a good accuracy (RMSE=0.024, N=3462982) and linear relationship between the gap filled and removed values (Figure 8), while the spatial fit result is also good (RMSE=0.007, N=526) but there are fewer spatial fitted pixels to evaluate. The spatial smoothing is the last step to ensure a gap-free product and as it utilizes mean value of nearby pixels directly without any adjustment from the information from the pixel itself, it is not unexpected that spatial smoothing results in the lowest accuracy (RMSE=0.029, N=24683). However, the number of gaps filled by spatial smoothing is only about 2%. The histogram of the differences between the gap-filled and the original values shows a normal distribution, with a mean value of 0.005 and a standard deviation 0.026 (as would be expected).

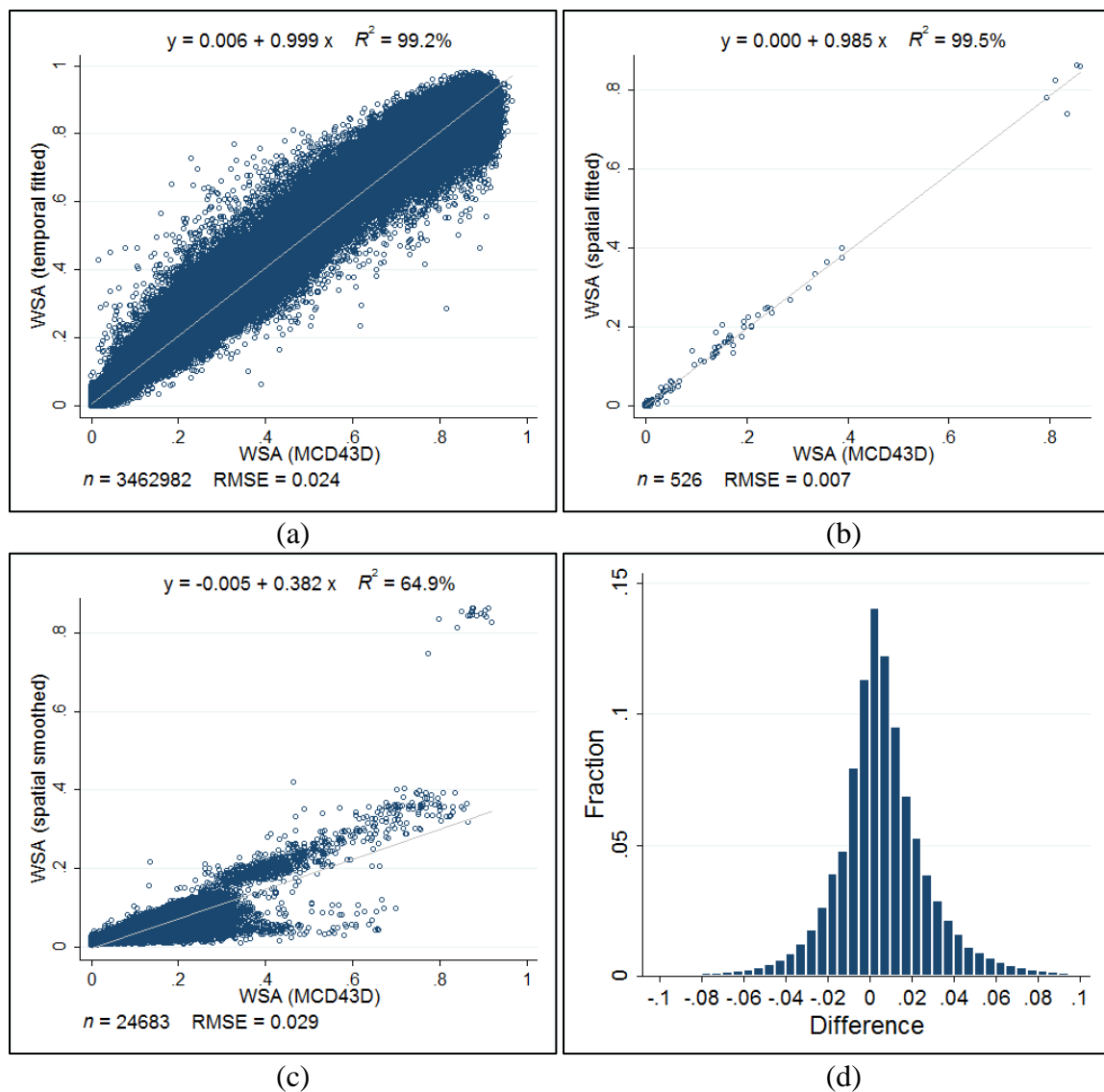


Figure 8 Original high quality values VS (a): temporal fitted, (b): spatial fitted, (c): spatially smoothed, and (d): histogram of the gap-filled data minus the original data (NIR band, 2010).

Averages of WSA in NIR band in 2010 for two-latitude bands are calculated for every land cover type for both gap-filled and original values. The four land cover types of Deciduous Broadleaf Forest, Mixed Forest, Open Shrublands, and Grasslands are selected to compare how the gap-filled values agree with the original values. From Figure 9 and Figure 10 we can see the spatial distributions of these land cover types: Deciduous

Broadleaf Forest is primarily located between 15° - 60° N and 15° - 30° S; Mixed Forest occurs mostly between 15° - 60° N; Open Shrublands are distributed all over the world but peak at 70° N and 30° S; and most of the Grasslands fall between 30° - 60° N. We can see in general that the gap-filled values agree well with the original values, although the gap-filled Mixed Forest pixels at 33° S result in lower values than the original data (Figure 9, upper right). This is because there are so few values (only hundreds) in the two-latitude band so the mean may be biased by outliers. The Grasslands also display higher values than the original data between 60° - 90° S, but there are so few such pixels in this 30 degree latitude band, that this effect may also be caused by classification errors in the classification map.

For each selected land cover type, some latitudes are chosen according to their spatial distribution to show the phenology curves. For the Deciduous Broadleaf Forest (Figure 11) we can see earlier an green up in lower latitudes, and reverse seasonality in southern hemisphere. The gap-filled curve agrees well with the original one, and is smoother than the original one. Small variations occur when there are relatively fewer gap-filled (thus temporally smoothed) pixels. The trend is the same for Mixed Forest (Figure 12), Open Shrublands (Figure 13) and Grasslands (Figure 14), and unsurprisingly the gap-filled values match the original values better when both have adequate numbers of pixels, indicating that the mismatch is caused by an insufficient number of pixels present for this class in that latitude band to actually reflect meaningful means for this land cover type.

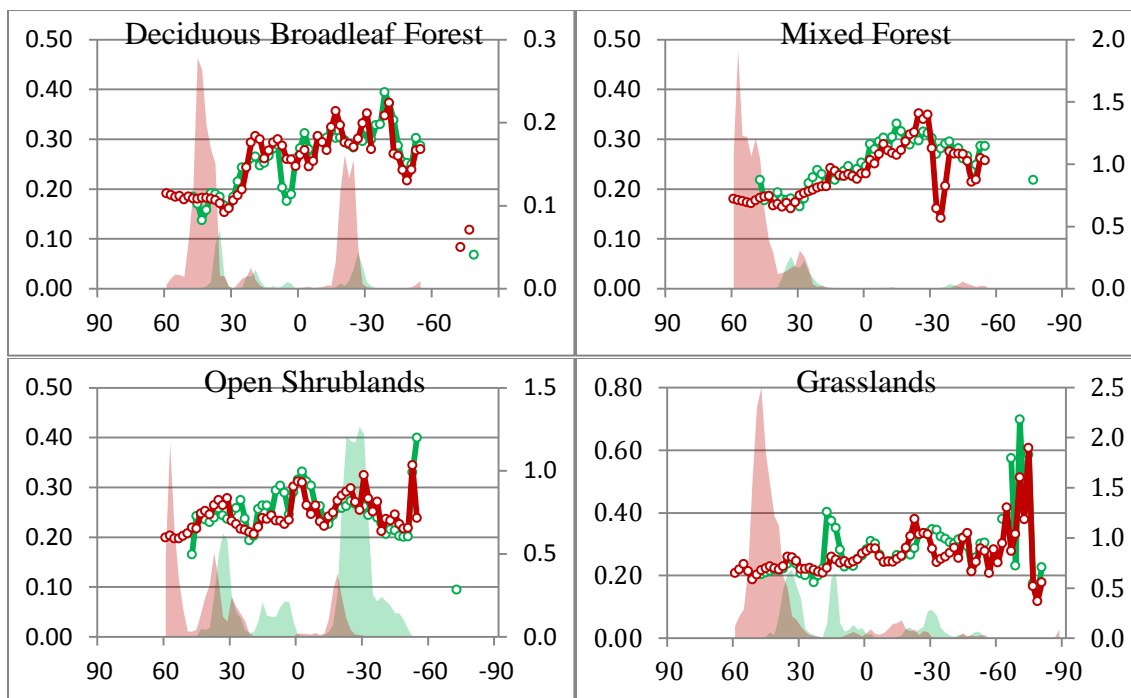


Figure 9 Mean of original and gap-filled WSA in NIR band of DOY 001, 2010 as a function of latitude. X: latitude. Y primary: albedo (for lines and points), secondary: number of pixels in units of millions (for areas). Greens: original in MCD43D, reds: gap-filled

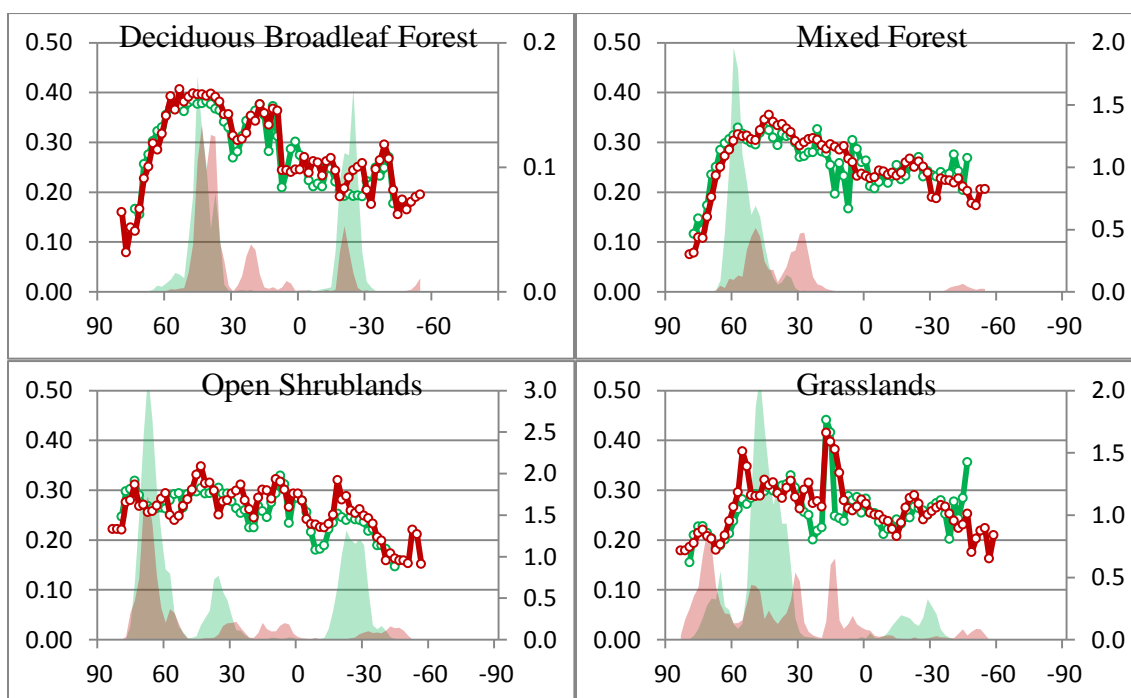


Figure 10 same as Figure 9 but for DOY 193, 2010.

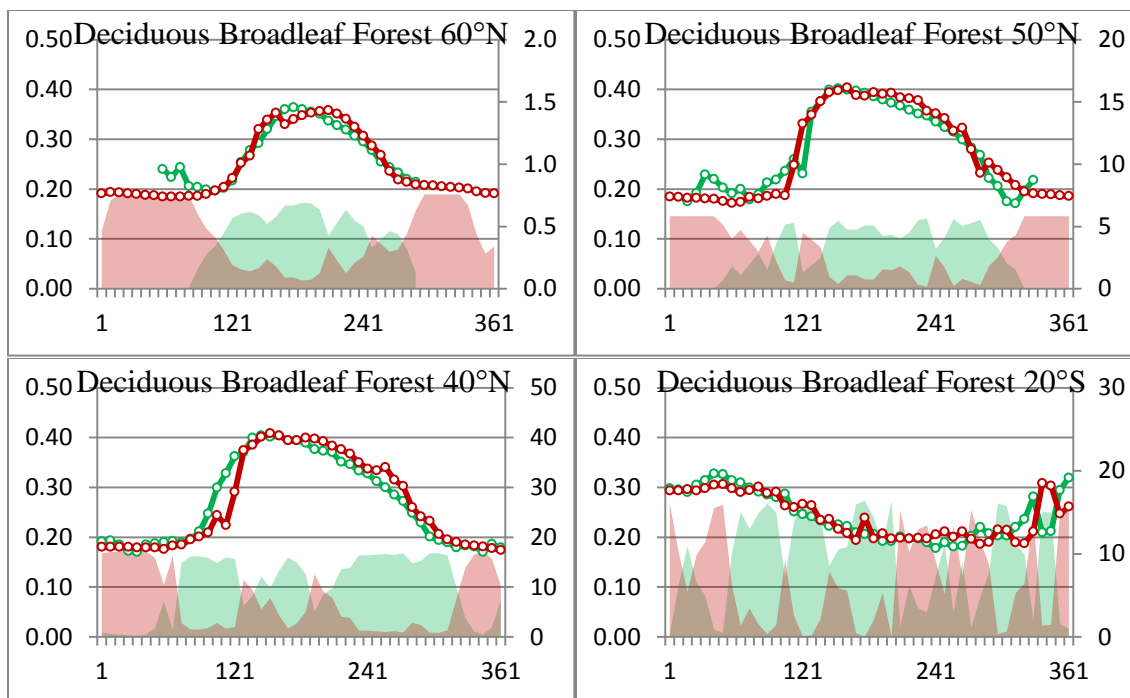


Figure 11 Mean of original and gap-filled WSA in NIR band in 2010 as a function of day of year. Number of pixel is in unit of 10,000.

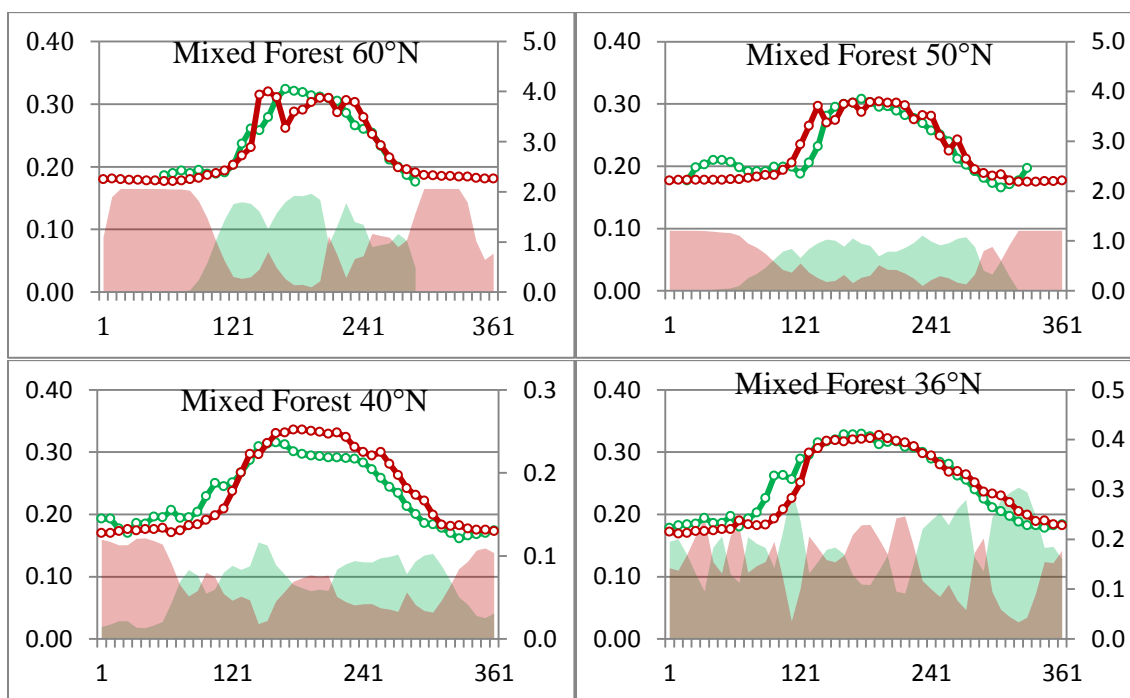


Figure 12 same as Figure 11 but for Mixed Forest, and number of pixels in unit of millions.

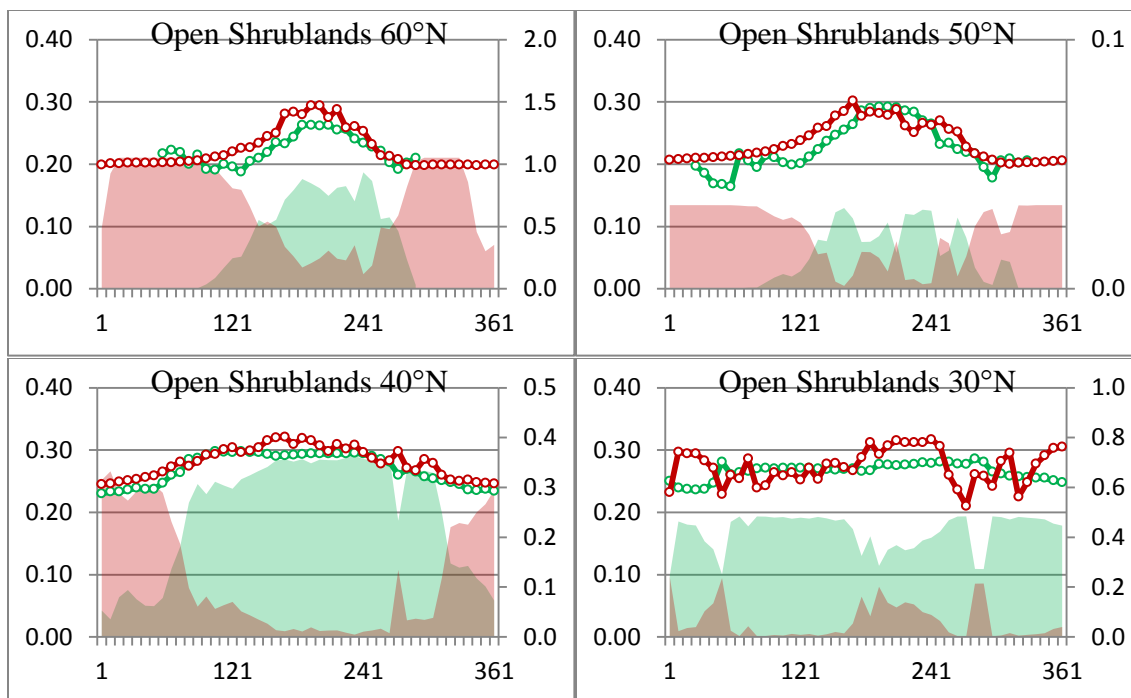


Figure 13 same as Figure 11 but for Open Shrublands, and number of pixels in unit of millions.

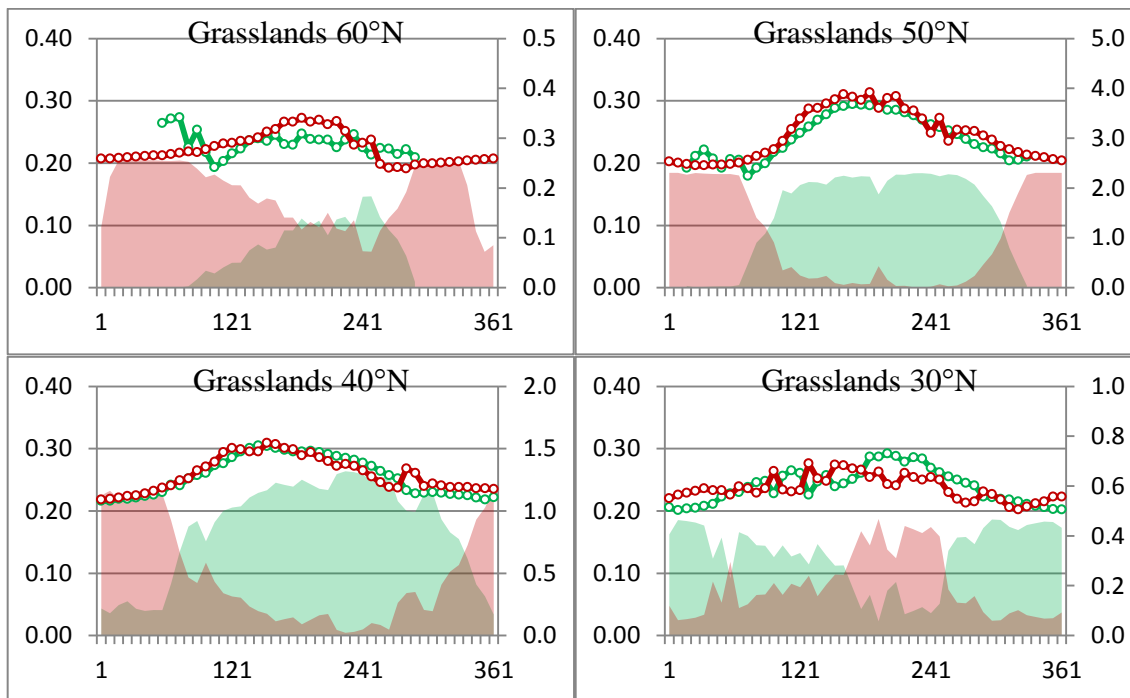


Figure 14 same as Figure 11 but for Grasslands, and number of pixels in unit of millions.

The BRDF shapes of a selected pixel are compared for the original high quality versus the gap-filled (Figure 15). This pixel was selected because the difference between the original and the gap-filled WSA is 0.026, which is the standard deviation between all the original high quality values and the gap-filled values (Figure 8, d). This figure shows the BRDF shapes of the gap-filled pixels and the original high quality pixels are close at lower SZN.

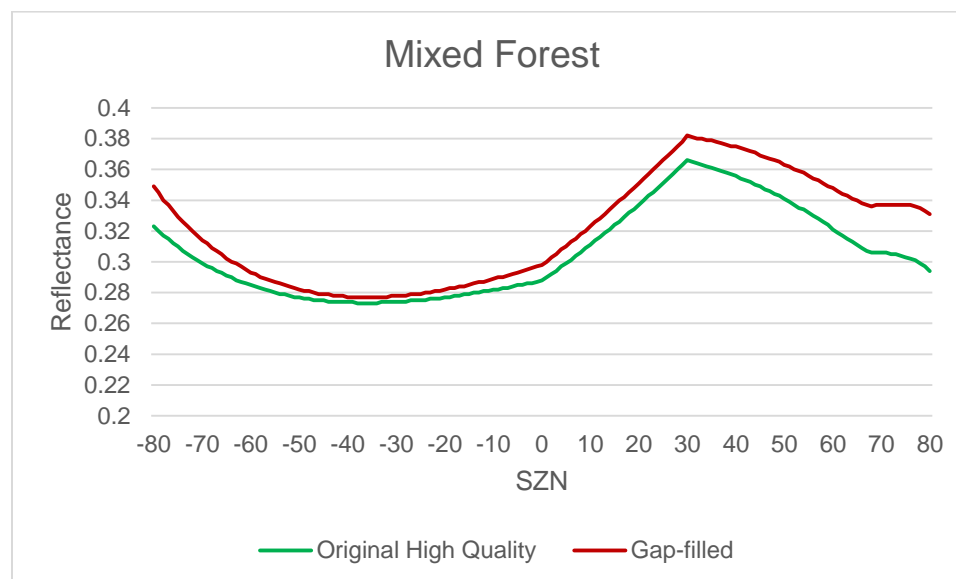


Figure 15 BRDF shapes at the principle plane for the original high quality (green) vs. the gap-filled (red) from a selected pixel in NIR band. SZN is set to 30 °.

2.4 Discussion

The spatially and temporally complete snow-free BRDF/Albedo can largely facilitate modelers who require gap-free albedo as an input. However, due to larger errors and bias for the temporally and spatially smoothed data, users should still pay attention to the QA flags provided when using the BRDF/Albedo dataset.

The MCD43D will be processed daily in V006. The daily BRDF will still be derived by the 16-day window, but the day of interest will be the center date of the 16

days, and the BRDF inversion will be weighted by the vicinity to the day of interest. The establishment of the gap filling techniques for the V005 product will all be applicable to the daily product, and the daily product will make the gap-filling easier because it can provide more high quality BRDF retrievals to constrain the temporal fit.

CHAPTER THREE

3. NARROW TO BROAD BAND CONVERSIONS BASED ON SATELLITE HYPERSENSPECTRAL DATA

Broadband albedo represents the fraction of total solar radiation that is reflected by the surface and is a crucial variable for the climate modeling. Liang et al. (1999 and 2000) have developed coefficients to convert spectral albedo to broadband albedo for a series of eight different satellite sensors mainly based on laboratory spectra of several land cover types. Since the laboratory spectra are usually collected from single leaves, the values may not represent the spectral characteristics of a pixel at remote sensing scales. As the Hyperion onboard EO-1 has been providing hyperspectral data since 2001, it is possible to develop new satellite derived narrow-to-broadband (N2B) coefficients to verify that the laboratory spectra really captures the diversity of land cover types and spatial representation. In this project we are utilizing the Hyperion derived N2B coefficients to prepare MODIS and VIIRS broadband albedos.

3.1 Data

The Hyperion collects observations in 242 spectral bands (196 are unique and usable) from 0.4 to 2.4 μm at a 30m resolution. The FWHM (Full Width Half Maximum) of Hyperion bands is approximately 11 nm and the spacing between band centers of approximately 10 nm (Figure 16).

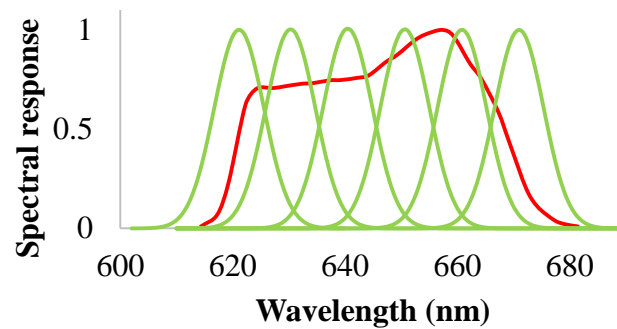


Figure 16 Spectral responses for MODIS band 1 (in red color) and Hyperion band 27-32 (green). The Hyperion spectral response function is modelled by a Gaussian function of eq. (10).

For this study, 43 cloud-free scenes of Hyperion data were randomly selected from all over the world covering different land cover types including forest, savanna, shrub, desert, crop, urban, etc.

Data Preprocessing

Several pre-processing steps are required before atmospherically correcting the Hyperion data. The Hyperion sensor has a single telescope but two spectrometers – one for the VNIR and the other for the SWIR data. The VNIR spectrometer provides 70 bands and the SWIR offers 172 bands providing 242 total potential bands. Some of these spectral channels (band number 1-7, 58-70 from VNIR, and 71-76, 225-242 from SWIR) are not calibrated due to low signal to noise, which leaves 198 usable bands. There are 2 pairs of channels that overlap between the two main detectors sets (56-57 from VNIR and 77-78 from SWIR). We keep the two bands (56-57) from VNIR and discard the 77-78 bands from SWIR so now there are 196 usable and unique bands left. Band selection is required to pick up the 196 unique bands: 8-57, and 79-224 before further processing.

Hyperion is a “pushbroom” scanner. For a line of pixels in a waveband, there are 256 pixels or sensors, which can lead to a non-uniform spectral response and thus both the central wavelength and FWHM can vary across the line – this is called a spectral “smile”. Using a single wavelength/FWHM for the 256 pixels will result in errors. However, wavelength & FWHM information is provided for each pixel in the associated metadata. In this study, we extract the central wavelength and FWHM information for every pixel, so there is no need to correct for the “smile” effect.

Another common problem for pushbroom systems is vertical streaking, which is also caused by the non-uniform spectral responses of the 256 pixels. In this effort, the column streaks are removed by adjusting each column with a gain and an offset according to the entire image statistics. The mean and standard deviation are calculated for the whole image, and then each column is balanced to make the statistics agree with the whole image statistics (Notes from a Hyperion workshop <ftp://ftp.eoc.csiro.au/pub/djupp/Hyperion/Workshop/>). The effects of the de-streaking method are shown in Figure 17.

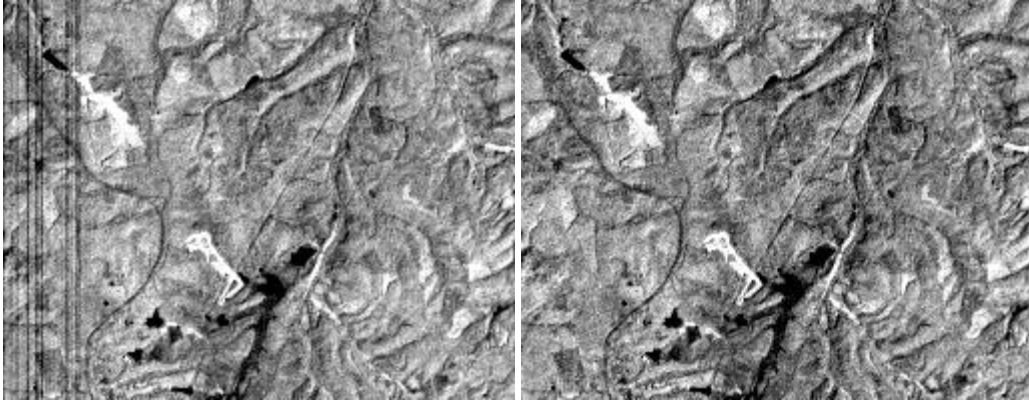


Figure 17 Vertical streaks in the Hyperion data (left), and the data after streak removal (right)

Due to water absorption, there are never values for the water absorption bands between 1350nm to 1480nm and 1800nm to 1970nm in the atmospherically corrected Hyperion surface reflectance data. Although this has little effect on the integration of the wavebands for calculation of a broadband albedo because the downward flux in these regions is nearly zero, but a linear interpolation is still employed to fill the gaps in the spectra to facilitate further computations.

3.2 Methods

Once the Hyperion examples have been de-streaked, generally quality controlled, and atmospherically corrected they can be used to develop narrow to broadband coefficients for moderate resolution sensors such as MODIS and VIIRS. We use the Hyperion hyperspectral bands to simulate the MODIS bands and the broad bands, then run regression analysis between the MODIS albedos and the broadband albedos to derive N2B coefficients. First, to simulate the MODIS bands, Given a MODIS spectral response function $f(\lambda)$, the efficient wavelength λ_{eff} can be calculated by eq. (7) (Nikolakopoulos et al., 2008).

$$\lambda_{eff} = \frac{\int \lambda f(\lambda) d\lambda}{\int f(\lambda) d\lambda} \quad (7)$$

And the efficient band width w_{eff} is calculated by eq. (8).

$$w_{eff} = \frac{\int f(\lambda) d\lambda}{\lambda_{eff}} \quad (8)$$

The Hyperion-to-MODIS conversion coefficients weight wt_i for each Hyperion band i is calculated by eq. (9) (Nikolakopoulos et al., 2007).

$$wt_i = \int g_i(\lambda) f(\lambda) d\lambda \quad (9)$$

Where $g_i(\lambda)$ is the i th Hyperion band's response at wave length λ , and is modelled as the Gaussian Function of eq. (10).

$$g_i(\lambda) = \frac{1}{\sqrt{2\pi\sigma_i^2}} e^{-\frac{(\lambda-\lambda_i)^2}{2\sigma_i^2}} \quad (10)$$

Where λ_i is the center wave length of Hyperion band i , and σ_i is related to the FWHM by eq. (11).

$$\sigma_i = \frac{FWHM_i}{2\sqrt{2\ln 2}} \quad (11)$$

The summation of the coefficients weight wt_i should be equal to the efficient MODIS band width, so the wt_i should be normalized by a factor of eq. (12).

$$c = \frac{w_{eff}}{\sum_i wt_i} \quad (12)$$

The Hyperion-to-Broadband coefficient weights can also be calculated using eq. (7) - (12) by defining three virtual spectral response functions:

$$f_{vis}(\lambda) = 1, \lambda \in [300, 700]nm \quad (13)$$

$$f_{nir}(\lambda) = 1, \lambda \in [700, 5000]nm \quad (14)$$

$$f_{sw}(\lambda) = 1, \lambda \in [300, 5000]nm \quad (15)$$

Hyperion center wave length and FWHM are provided per each pixel each band.

So, given Hyperion spectral albedo a_i , downward flux d_i , and the MODIS spectral response function, we can simulate the seven MODIS band albedos as well as the three broadband albedo (0.3-0.7, 0.7-5.0, 0.3-5.0 μm) with eq. (16).

$$a = \frac{\sum_i a_i d_i FWHM_i w t_i}{\sum_i d_i FWHM_i w t_i} \quad (16)$$

Where a is the albedo for the first 7 MODIS bands or one of the broadband albedo depending on the appropriate coefficient weight $w t_i$ used.

Next, atmospheric correction is required to derive Hyperion surface reflectance. Here we assume the land surface is Lambertian to simplify the atmospheric correction process. And in the Lambertian case, a narrow band albedo numerically equals the surface reflectance, so we can use eq. (16) to derive the MODIS albedos and broadband albedos. In this research, we use MODTRAN to do atmospheric correction and calculate downward irradiance from Hyperion L1R Top-of-Atmosphere (TOA) radiance data (<http://glovis.usgs.gov/>).

According to four-stream radiative transfer theory (Verhoef and Bach, 2003), for a homogeneous Lambertian surface:

$$L = \frac{E_s^0 \cos \theta_s}{\pi} \left[\rho_{so} + \frac{(\tau_{ss} + \tau_{sd}) a (\tau_{do} + \tau_{oo})}{1 - a \rho_{dd}} \right] \quad (17)$$

Where L is the radiance observed by the sensor, E_s^0 is TOA solar irradiance, θ_s is solar zenith angle, ρ_{so} is TOA atmospheric bidirectional reflectance, τ_{ss} is direct atmospheric

transmittance in the direction of the sun, τ_{sd} is diffuse atmospheric transmittance for solar incidence, τ_{do} is directional atmospheric transmittance for diffuse incidence, τ_{oo} is direct atmospheric transmittance in the direction of viewing, a is the surface albedo (or surface reflectance in the Lambertian case), and ρ_{dd} is the (Bottom-of-Atmosphere) BOA spherical albedo of the atmosphere. By running MODTRAN with $a = 0.0, 0.5,$ and $1.0,$ the values of $E_s^0, \rho_{so}, \tau_{ss}, \tau_{sd}, \tau_{do}, \tau_{oo},$ and ρ_{dd} can be derived (details can be found in Verhoef and Bach, 2003) and then be used to calculate the surface reflectance for any given TOA radiance. Also, we can calculate the downward flux by using the two equations:

$$E_{direct} = \tau_{ss} E_s^0 \cos\theta_s \quad (18)$$

$$E_{diffuse} = E_s^0 \cos\theta_s \frac{\tau_{sd} + \tau_{ss} \overline{r_{sd}} \rho_{dd}}{1 - \overline{r_{dd}} \rho_{dd}} \quad (19)$$

Where $\overline{r_{sd}}$ is average surroundings diffuse reflectance for solar incidence, and $\overline{r_{dd}}$ is average surroundings diffuse reflectance for diffuse incidence. Assume the land surface is homogeneous and $\overline{r_{dd}} = \overline{r_{sd}} = a$ then we can also calculate the downward direct and diffuse flux by the same three runs of MODTRAN.

For the MODTRAN runs, one of the 5 possible atmosphere models (tropical atmosphere, mid-latitude summer, mid-latitude winter, sub-arctic summer, and sub-arctic winter) is selected based on the latitude/longitude and acquisition time of the Hyperion data, and the RURAL model is generally chosen for the aerosol model. The MODTRAN default water vapor column and aerosol optical depth are used. The sun-view geometry is extracted from the Hyperion metadata.

The Hyperion TOA radiance is first aggregated to 500m to simulate the MODIS spatial resolution. And then for each pixel, the outputs (.7sc) of the 3 MODTRAN runs are integrated to the 196 selected Hyperion bands based on the per-pixel wave length and FWHM. Equation (17) is solved to calculate the surface reflectance and downward flux. At the last, a linear regression analysis is conducted to derive the narrow to broad band conversion coefficients based on equations (20), (21), and (22). Each of the aggregated pixels provides a sample for the regression analysis.

$$a_{vis} = \sum_{i \in (1, 3, 4)} c_i a_i + C_{vis} \quad (20)$$

$$a_{nir} = \sum_{i \in (2, 5, 6, 7)} c_i a_i + C_{nir} \quad (21)$$

$$a_{sw} = \sum_{i \in [1, 7]} c_i a_i + C_{sw} \quad (22)$$

3.3 Results

The regression analysis results are shown in Table 1. The current operational coefficients (Liang et al., 1999) are also listed for comparison. Because no Hyperion snow data are used in this research, the new N2B coefficients are for non-snow pixels only. The operational MODIS Albedo product use separate N2B coefficients to derive snow broadband albedo (Stroeve et al., 2005).

Table 1 Comparison between the new (upper) and the current operational (lower) N2B

New	Band1	Band2	Band3	Band4	Band5	Band6	Band7	Constant
VIS	0.3692		0.3355	0.3038				0.0002
NIR		0.4657			0.3210	-0.0794	0.2552	0.0024
SW	0.2480	0.1969	-0.0562	0.3008	0.2153	-0.0362	0.0694	-0.0054
Current								
VIS	0.3265		0.4364	0.2366				-0.0019
NIR		0.5447			0.1363	0.0469	0.2536	-0.0068
SW	0.3973	0.2382	0.3489	-0.2655	0.1604	-0.0138	0.0682	0.0036

After the regression analysis, the converted albedo (broadband albedo converted from the MODIS albedo using the new N2B coefficients, y axis in Figure 18) versus the simulated broadband albedo (x axis in Figure 18) are plotted (Figure 18, Figure 19, Figure 20). The VIS broadband albedo provides the best regression result of $R^2 = 0.9996$ (Figure 18), while the R^2 for the NIR and short wave broadbands is 0.9864 (Figure 19) and 0.9948 (Figure 20) respectively. From the NIR and shortwave (SW) results we can see branches with different slopes in the scatter plots, which might be correlated to the different spectral curve shapes of different land cover types. However, in this research we aim to develop a group of simple conversion coefficients which is universal for all non-snow land cover types so users do not have to first complete land cover classifications, so we just mix these pixels and take the average of the trends.

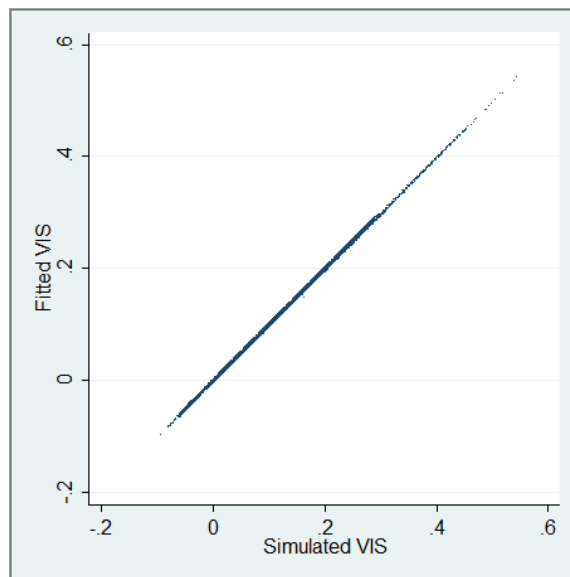


Figure 18 Regression result for VIS

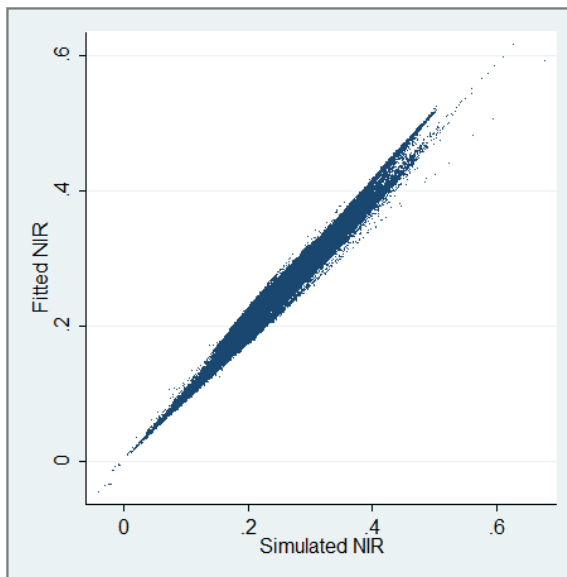


Figure 19 Regression result for NIR

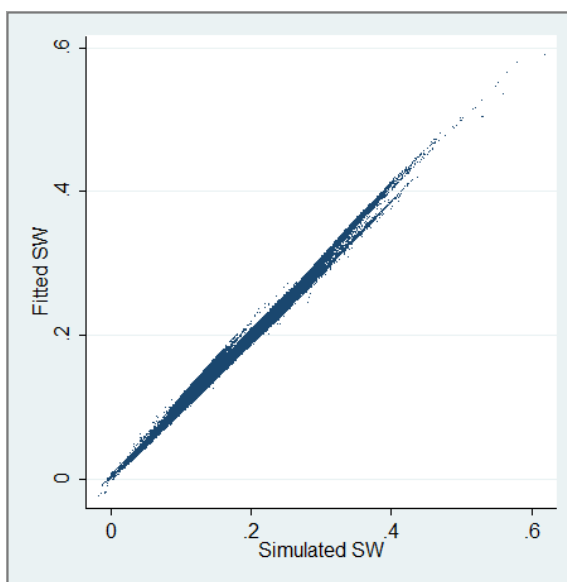


Figure 20 Regression result for Shortwave

3.4 Assessment

Ground shortwave albedo are collected from multiple flux networks: the Canadian Carbon Program (CCP, http://fluxnet.ornl.gov/site_list/Network/3), the Infrastructure for Measurements of the European Carbon Cycle (IMECC, <http://imecc.ipsl.jussieu.fr/>), the

AmeriFlux (<http://ameriflux.ornl.gov/>), the OzFlux (<http://www.ozflux.org.au/>), the CarboAfrica (http://www.carboafrica.net/index_en.asp), the Surface Radiation Network (SURFRAD, <http://www.esrl.noaa.gov/gmd/grad/surfrad/>), the Baseline Surface Radiation Network (BSRN, <http://www.bsrn.awi.de/>), and the Long Term Ecological Research (LTER, <http://www.lternet.edu/>) (Table 2). These are actual broadband blue sky albedo quantities (as collected by radiometers or albedometers) and are characteristic of the atmosphere at the time of acquisition. The MODIS values must be converted from intrinsic surface quantities (black sky albedo and white sky albedo) at spectral bands to blue sky actual albedos at the broad bands. Ground sites with good representativeness (Román et al., 2009, 2010; Cescatti et al., 2012) are selected because comparing satellite albedo with ground measurements is significantly affected by footprint mismatch and heterogeneity of the land surface.

MODIS V006 daily albedo is processed and extracted for each flux site, and then MODIS narrow band albedo values are converted to broadband shortwave blue sky albedos using the Román et al. (2010)'s method. AOD data from the MODIS 10km AOD product (MOD04) are used to derive the sky light diffuse fraction from a pre-calculated lookup table. For some sites at which AOD data are not available, a uniform climatological value of 0.2 AOD is used. The MODIS shortwave albedo is calculated by the new N2B coefficients and by the current operational coefficients from lab spectra (Liang et al., 1999) separately and then these are both compared with the ground albedo.

Table 2 selected flux network sites

Site Name	Latitude	Longitude	Land Type	Flux Networks
BC-Campbell River 1949 Douglas-fir	49.867	-125.334	Evergreen Needleleaf Forest	CCP
SK-1998 Fire	54.092	-106.005	Evergreen Needleleaf Forest	CCP
Wetzstein	50.454	11.458	Evergreen Needleleaf Forest	IMECC
Griffin- Aberfeldy-Scotland	56.607	-3.798	Evergreen Needleleaf Forest	AmeriFlux
Tumbarumba	-35.656	148.152	Evergreen Broadleaf Forest	OzFlux
Hesse Forest- Sarrebourg	48.674	7.066	Deciduous Broadleaf Forest	IMECC
Walker Branch	35.959	-84.287	Deciduous Broadleaf Forest	AmeriFlux
SK-1989 Fire	54.254	-105.878	Mixed Forests	CCP
Bily Kriz- Beskidy Mountains	49.502	18.537	Mixed Forests	IMECC
Hainich	51.079	10.452	Mixed Forests	IMECC
Harvard Forest	42.538	-72.172	Mixed Forest	Ameriflux
Las Majadas del Tietar	39.942	-5.773	Closed Shrublands	IMECC
Skukuza	-25.020	31.497	Savannas	CarboAfrica
El Saler-Sueca	39.276	-0.315	Croplands	IMECC
Dripsey	51.987	-8.752	Grasslands	IMECC
Fort Peck	48.308	-105.102	Grasslands	SURFRAD
Boulder	40.050	-105.010	Grasslands	BSRN
Cottonwood	43.950	-101.847	Grasslands	AmeriFlux
Barrow	71.323	-156.609	Tundra	BSRN
Imnaviat	68.613	-149.312	Tundra	LTER
Desert Rock	36.620	-116.020	Desert	SURFRAD

Although the new N2B coefficients assign different weights to the seven MODIS narrow bands, the results are very close to the current operational conversion coefficients (Figure 21, Figure 22, and Figure 23). From Figure 23 we can see the MODIS V006 daily albedo match the ground measurements very well. The SW albedo calculated by the new N2B usually overlap the values calculated from the current operational lab spectral

derived coefficients, but sometimes a little bit larger during the growing season. However it agrees with the ground albedo better for some sites. For example, for the Harvard Forest site (number 18 of Figure 23), the two MODIS SW albedos overlap between DOY 90 and 120, and both agree with the ground albedo values well. From DOY 120 to 200, the new N2B calculated albedo are larger than the operational SW albedo, but are closer to the ground truth. Similar trends can be found at sites EL 2009 and Hesse 2004. For the site WalkerBranch 2005, the new N2B results are larger in the growing season, but both of the MODIS SW albedos are a little larger than the ground measurements. At the Wetzstein 2005 site, the MODIS SW albedo shift away from the ground albedo. However, for this site, a climatological AOD of 0.2 was used when calculating broadband albedo, which is probably one of the reasons for the mismatch.

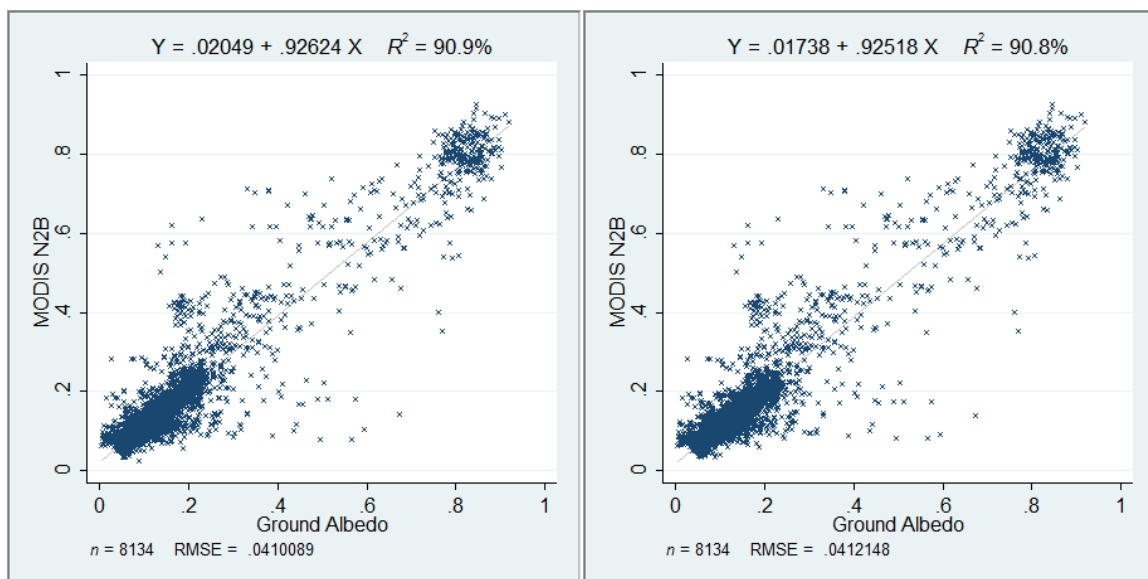


Figure 21 Correlations between ground albedo and MODIS SW Albedo calculated by the new N2B (left) and the current operational N2B (right)

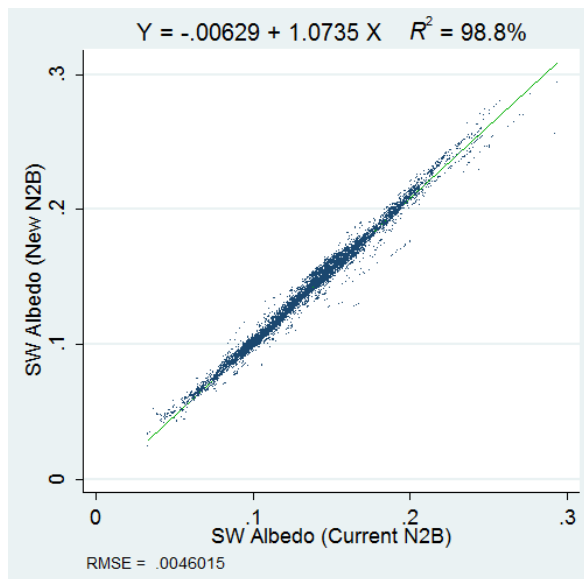
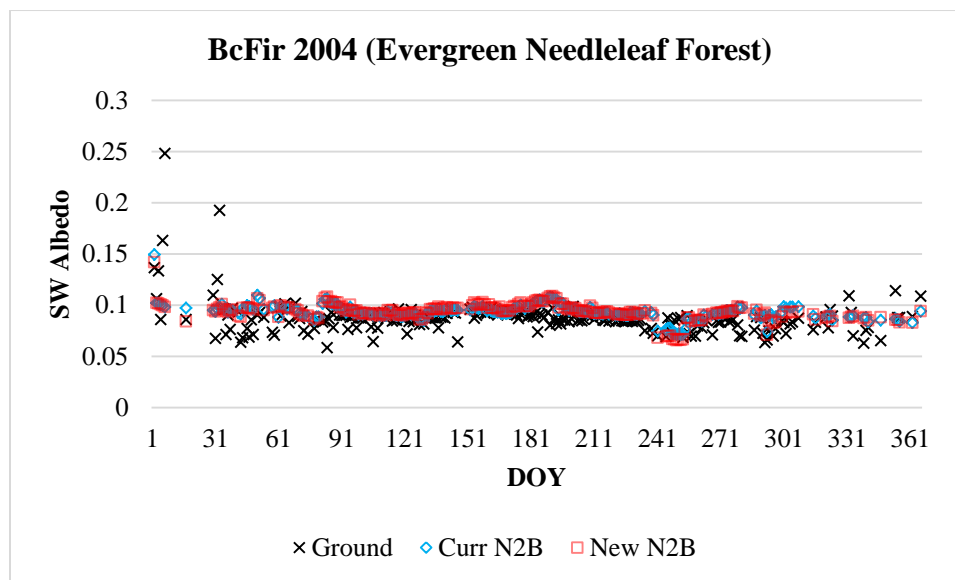
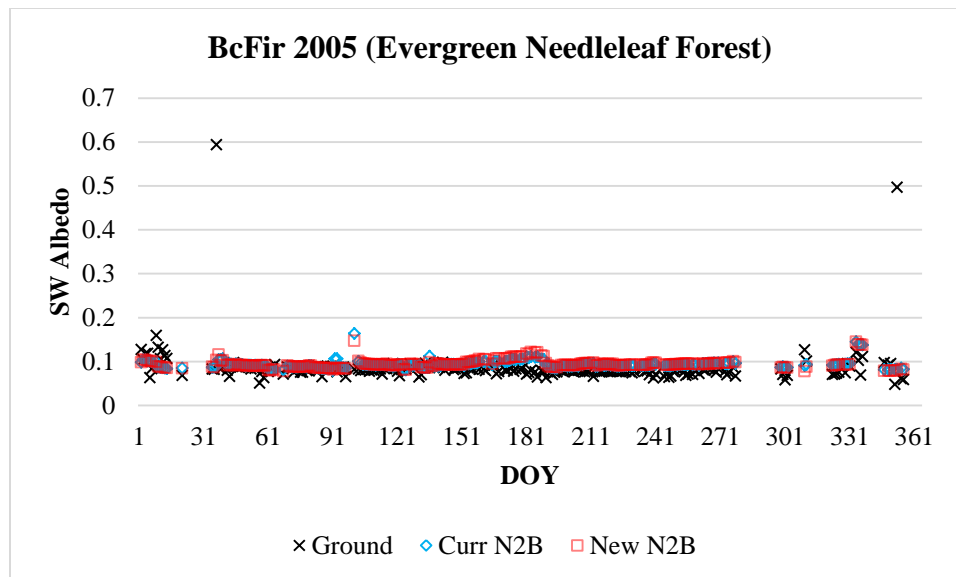


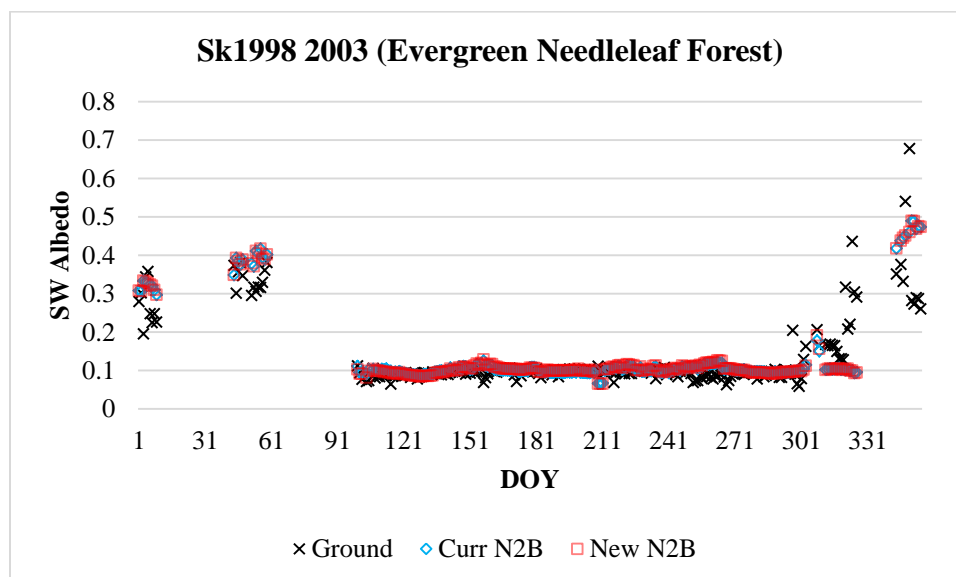
Figure 22 Scatter plot of the shortwave albedo calculated by the new N2B versus that calculated by the current N2B.



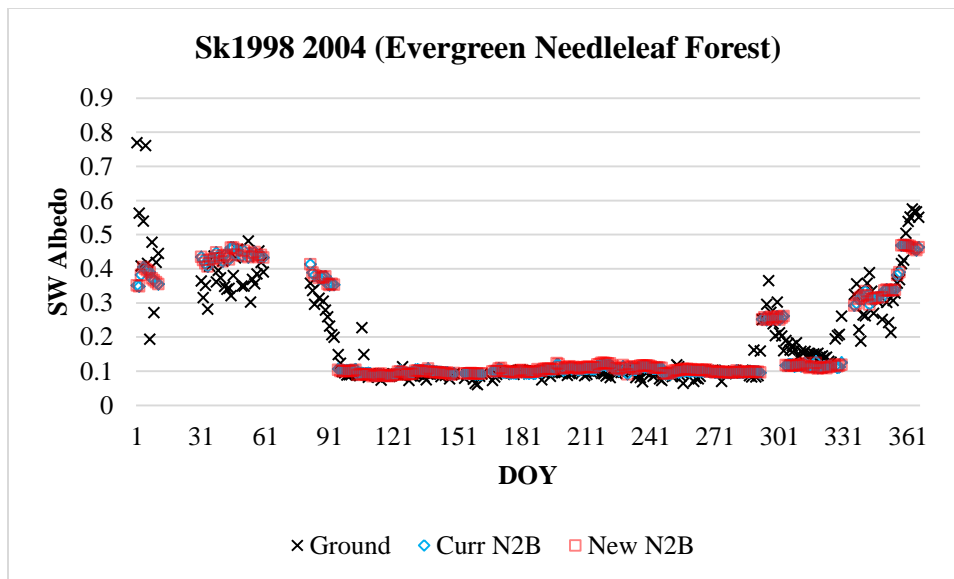
(1)



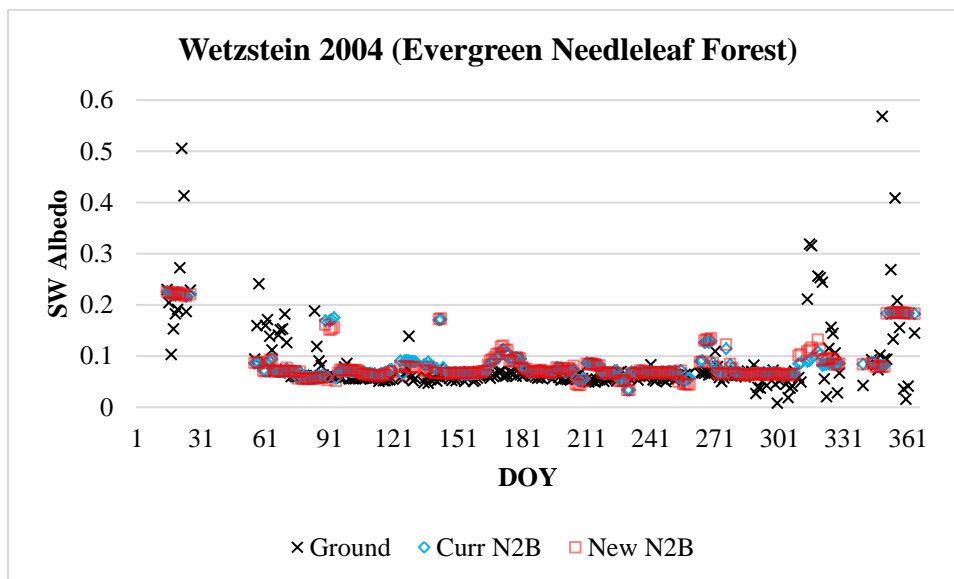
(2)



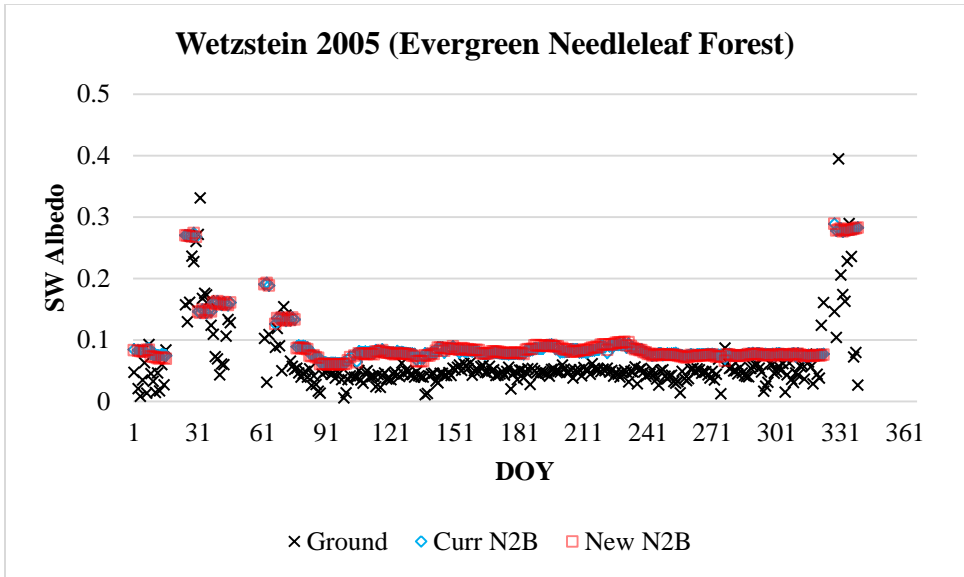
(3)



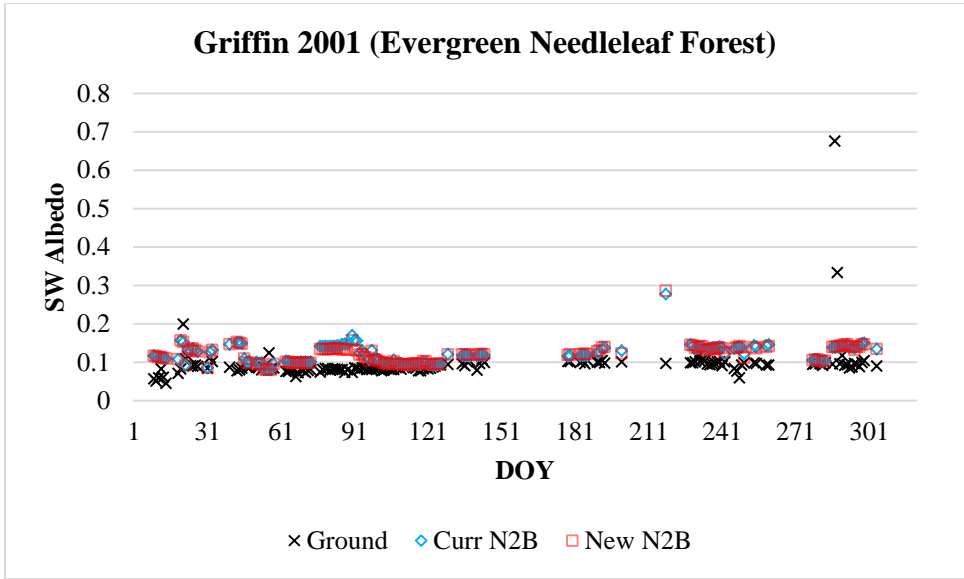
(4)



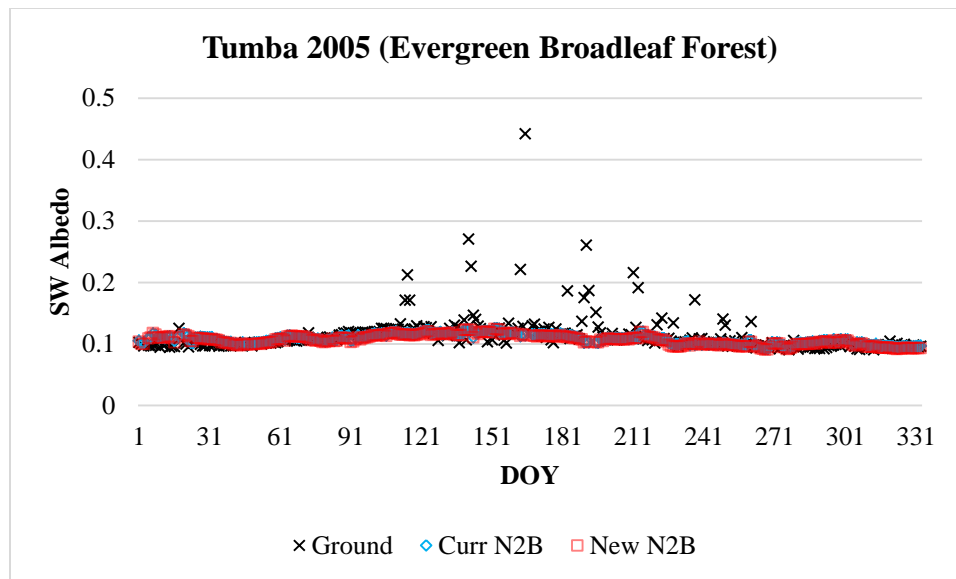
(5)



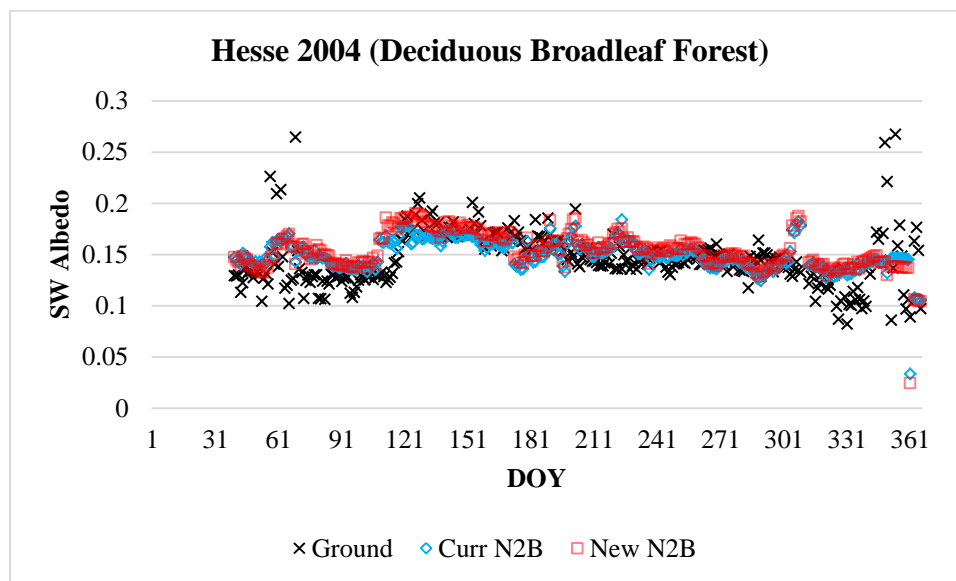
(6)



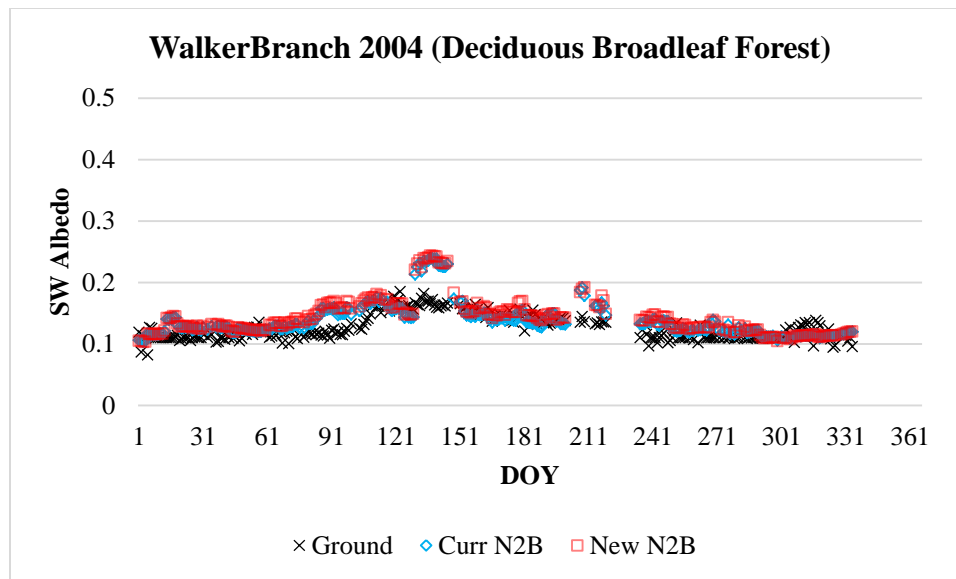
(7)



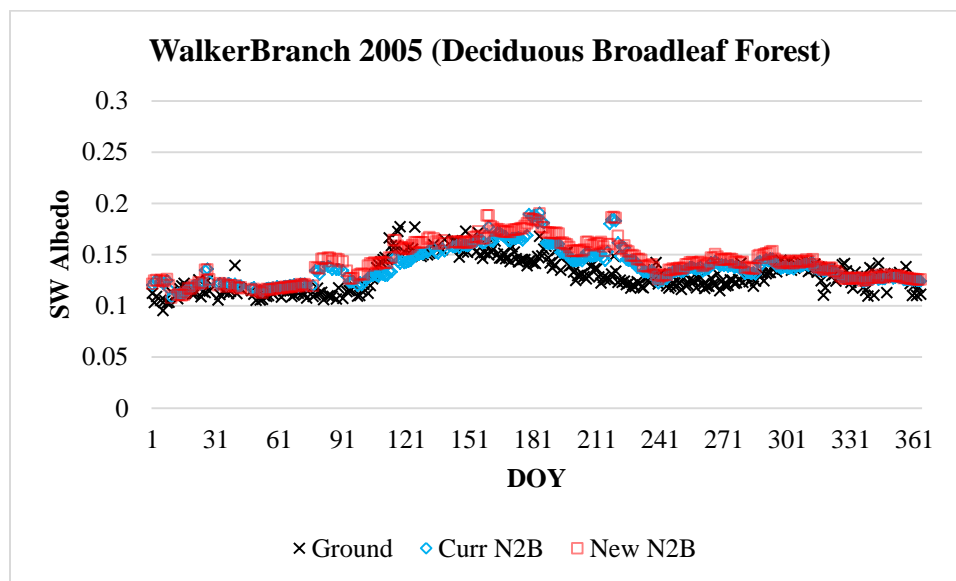
(8)



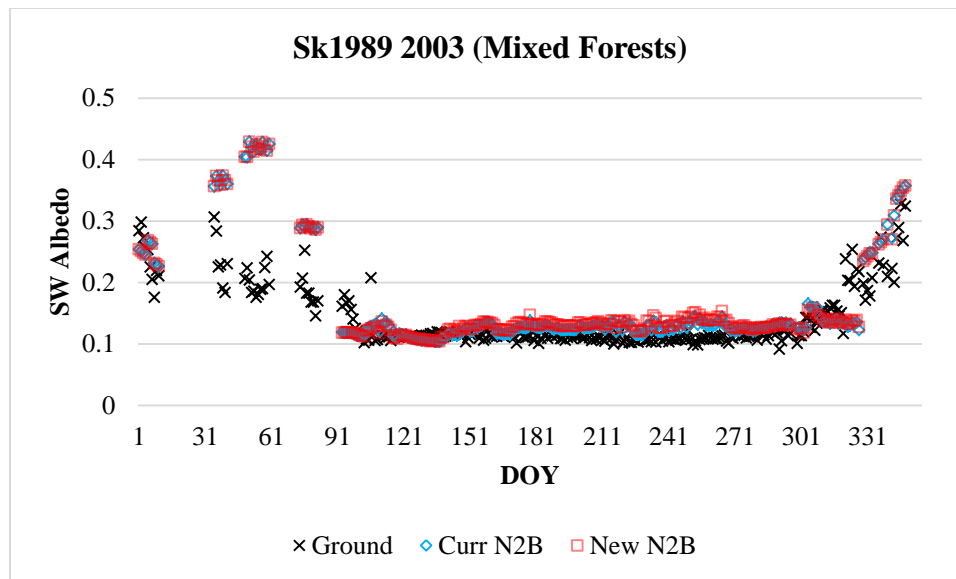
(9)



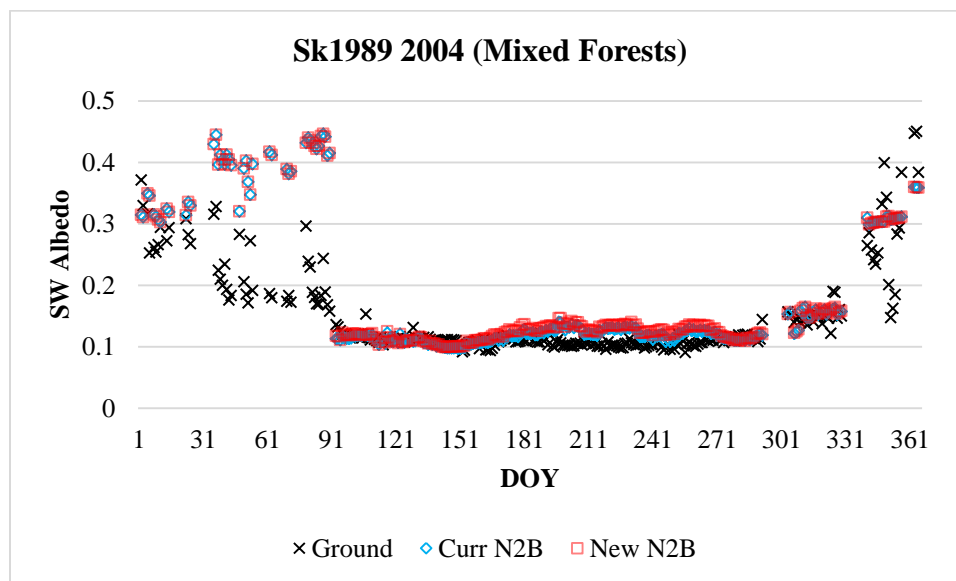
(10)



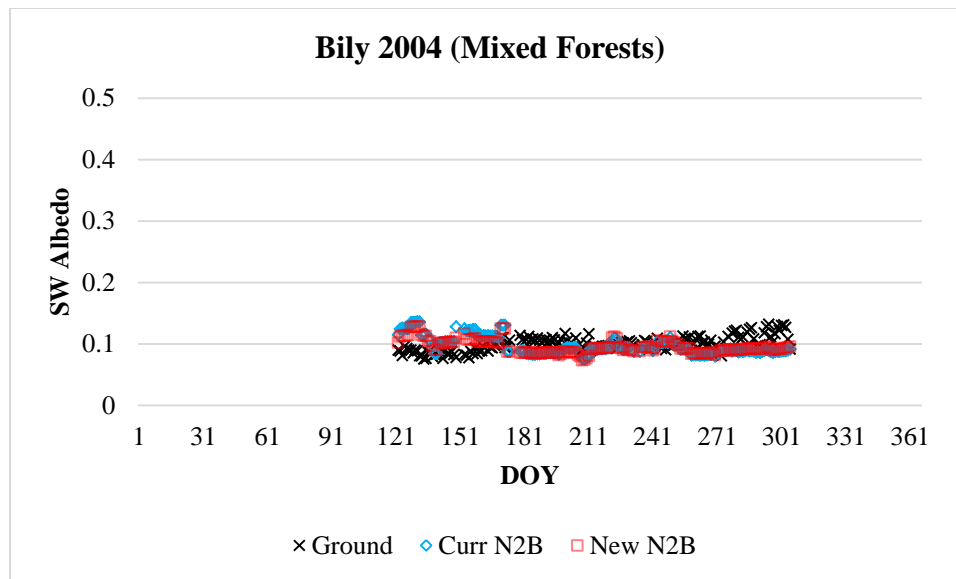
(11)



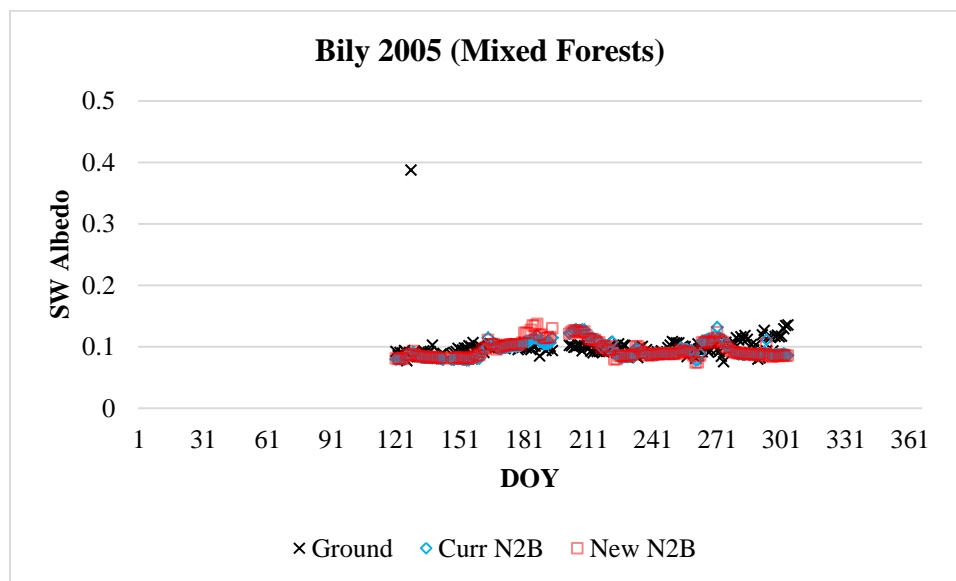
(12)



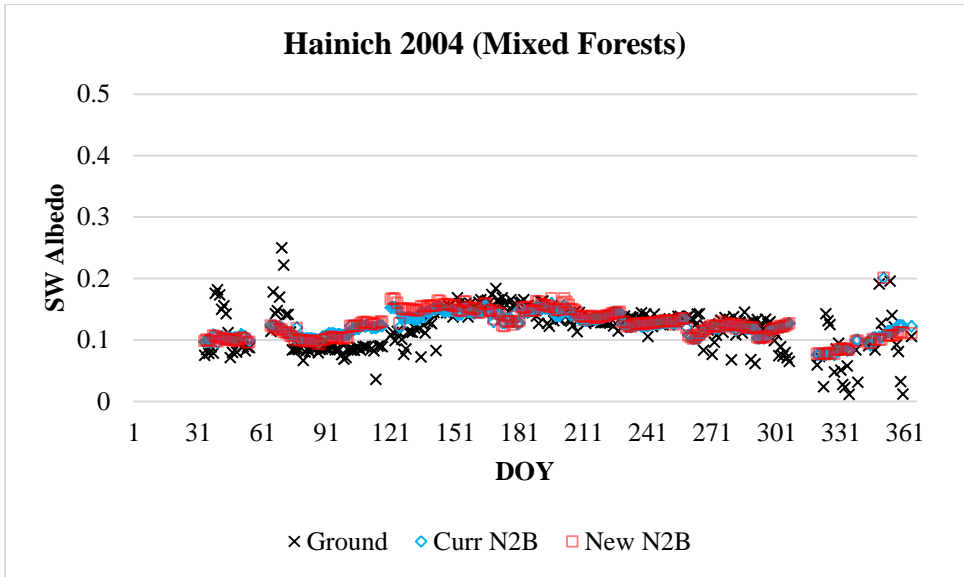
(13)



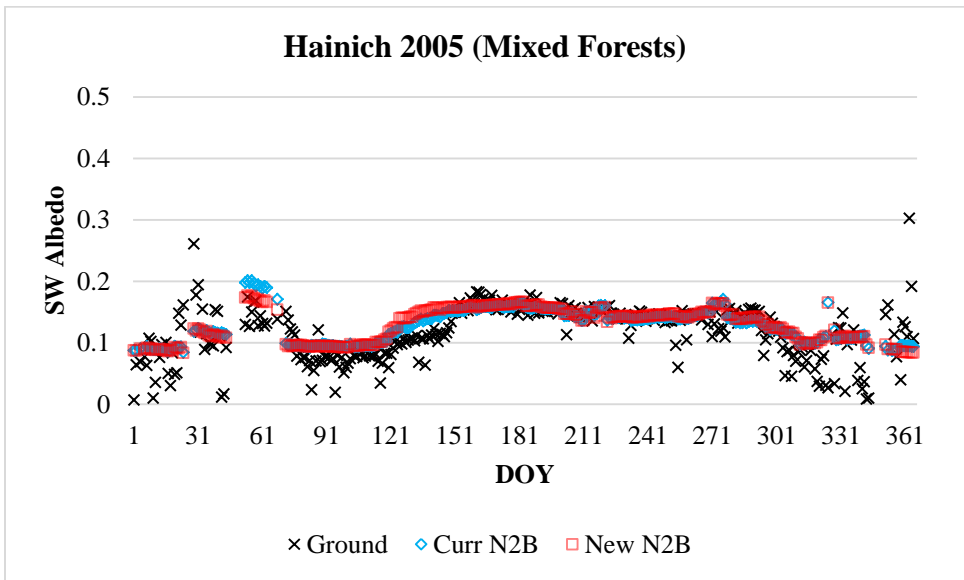
(14)



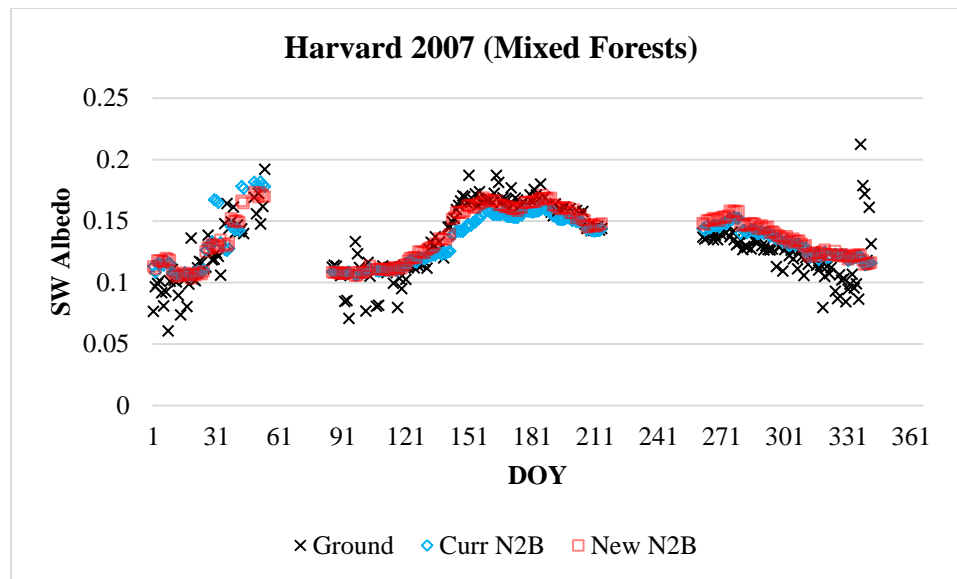
(15)



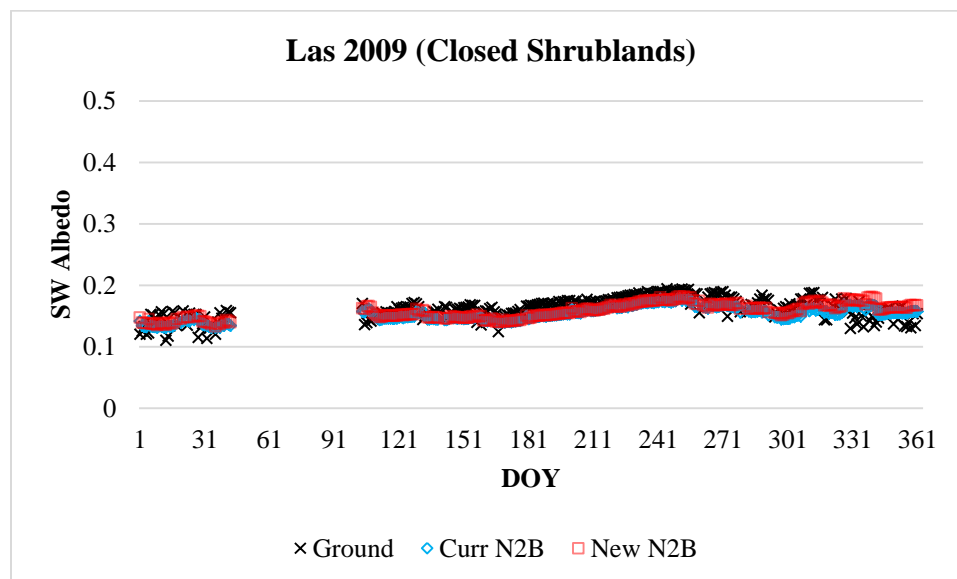
(16)



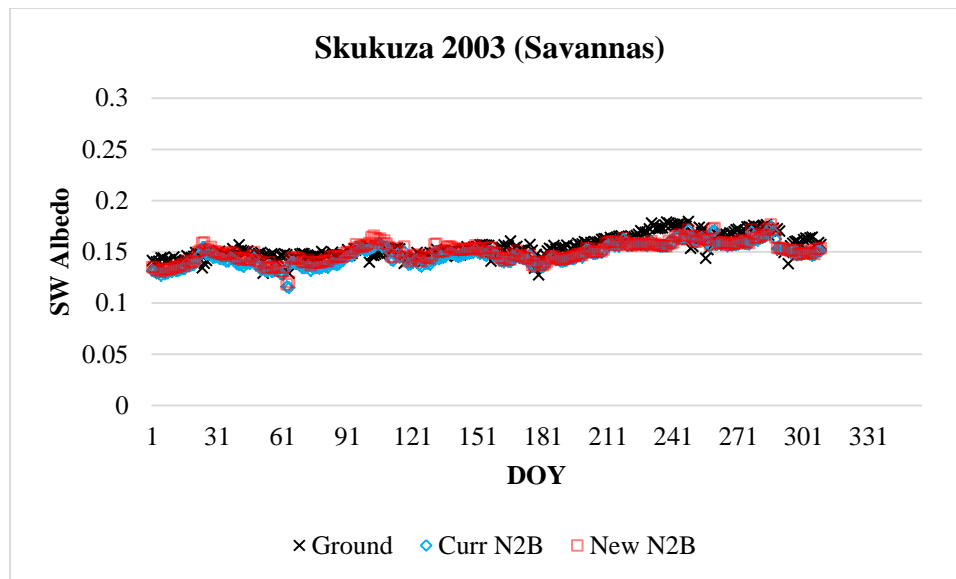
(17)



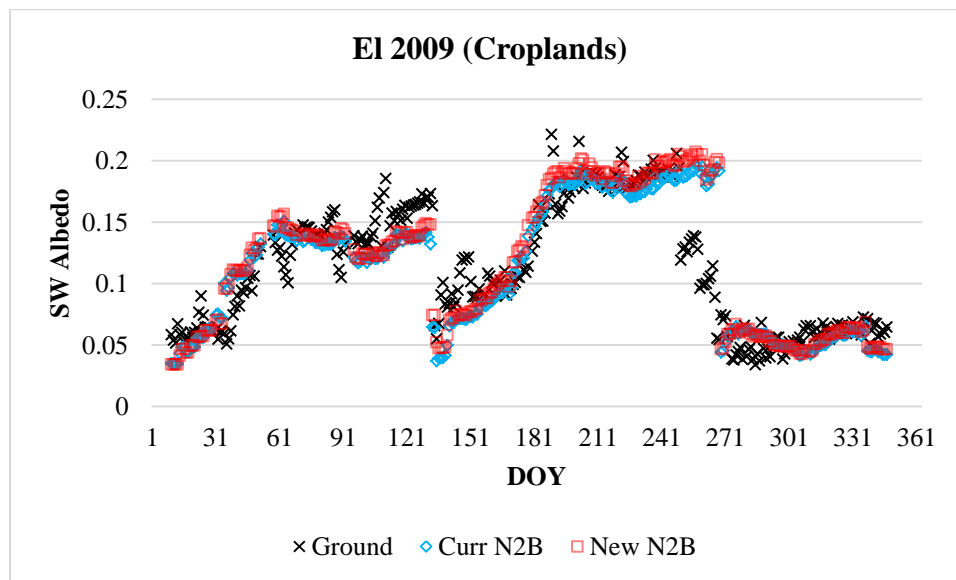
(18)



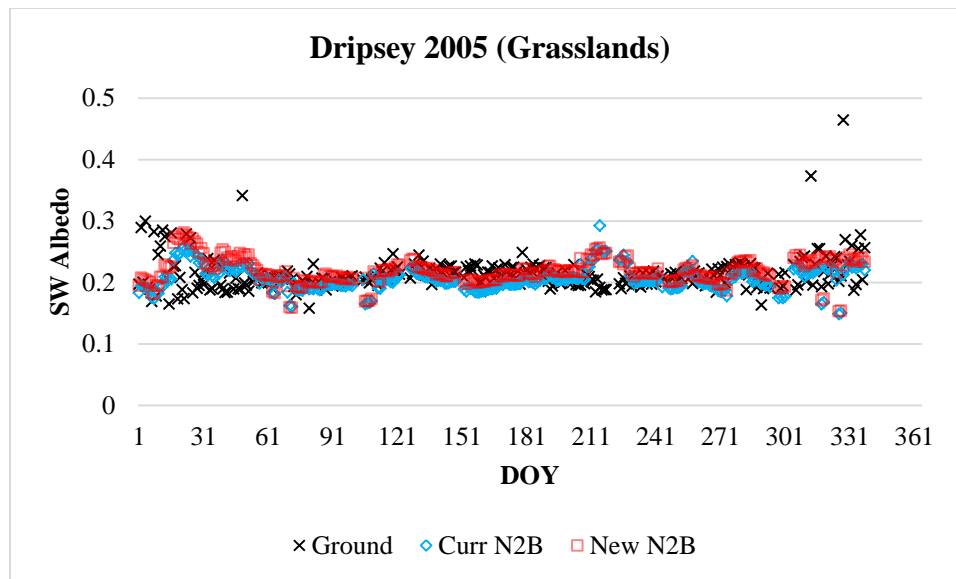
(19)



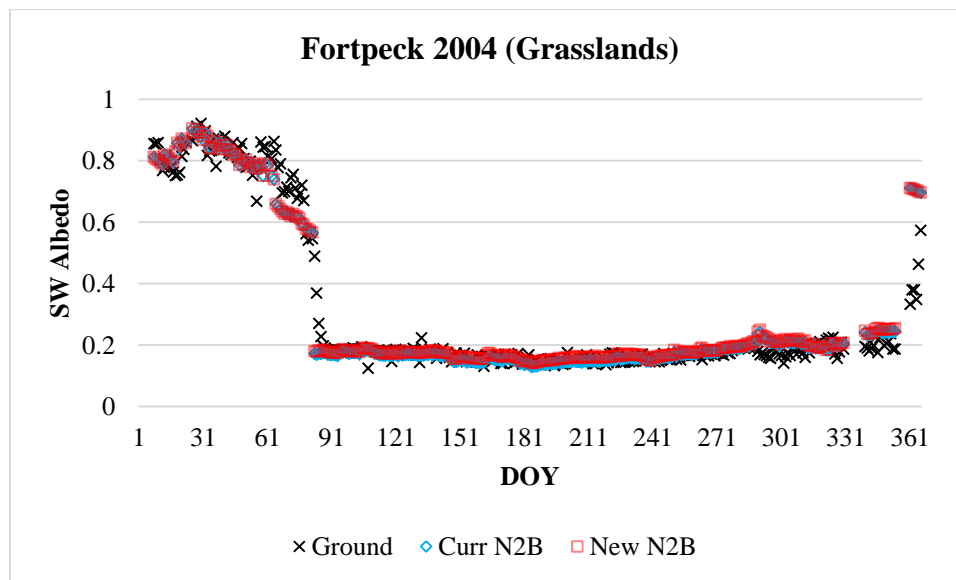
(20)



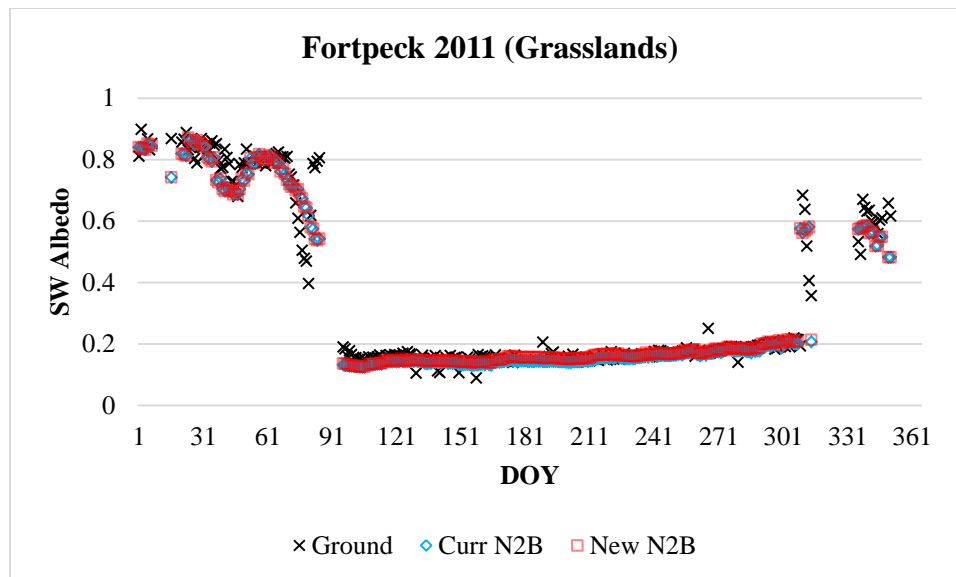
(21)



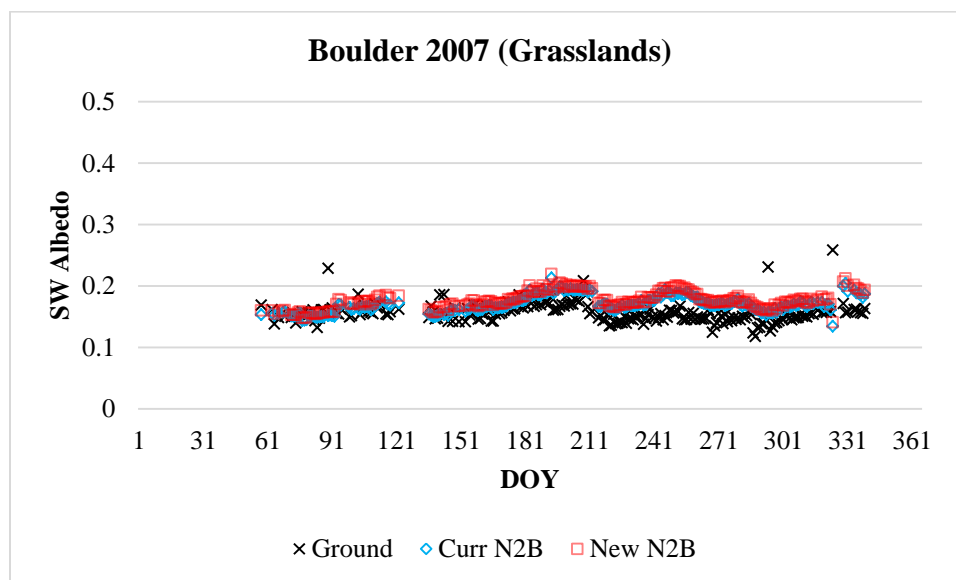
(22)



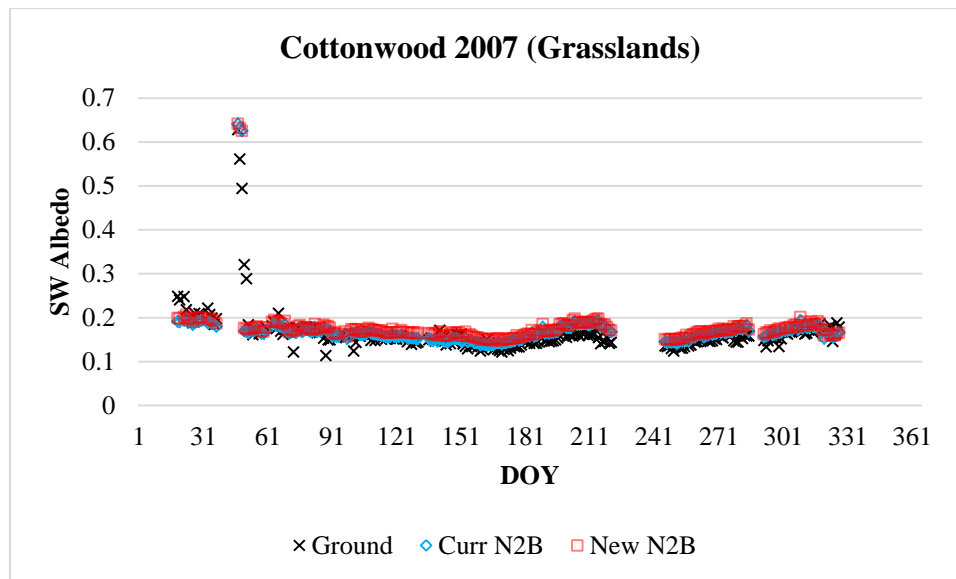
(23)



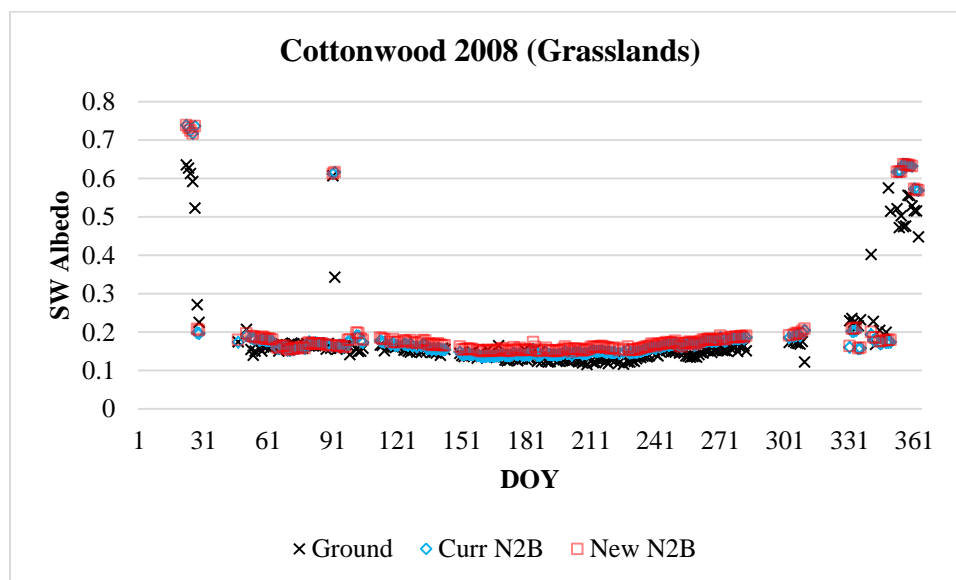
(24)



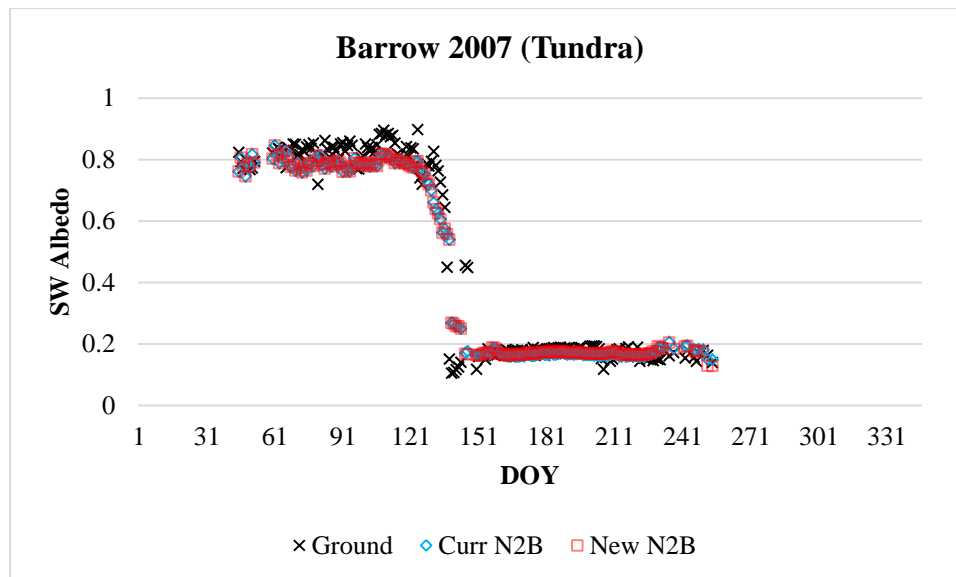
(25)



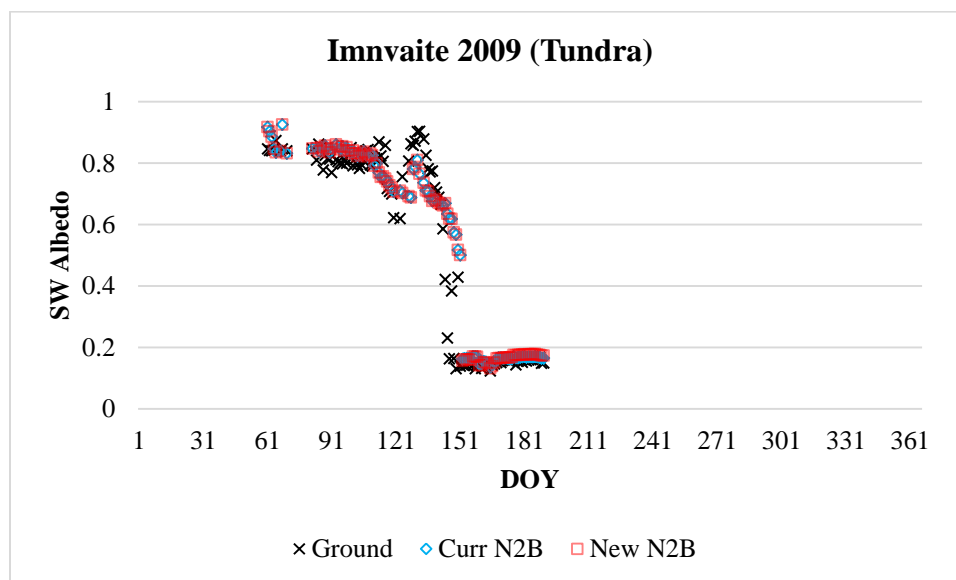
(26)



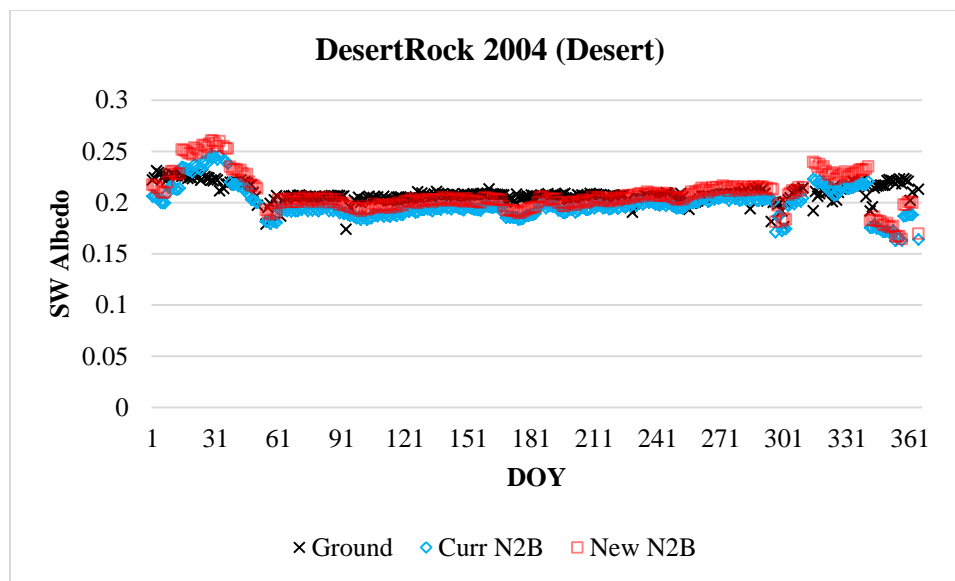
(27)



(28)



(29)



(30)

Figure 23 Ground shortwave albedo VS. MODIS N2B albedo

3.5 Discussion

The new N2B coefficients based on Hyperion values perform well as compared to field measurements and the results are very close to the current operational N2B coefficients based on lab spectra. In the growing season the new N2B calculated SW albedos are generally slightly higher than the current N2B results (Figure 23).

Further researches are needed to fully investigate the causes of the branches in the scatter plots of the regression results. The N2B coefficients are determined by the spectral shape of the surface reflectance and the spectral distribution of downward flux. Different land cover types are characterized by different reflectance curves, so theoretically we could develop N2B conversion coefficients separately for each land cover type to see if they are the same or different. However this would mean we would have to first classify

satellite data by land cover. Therefore, for ease-of-use, we need to develop a group of universal coefficients for all the land cover types (or actually separate things into two separate coefficients for snow-free and snow situations).

The advantage of using satellite data to derive the N2B coefficients is the spatial representativeness of the hyperspectral signals from satellite sensors which observe the earth from the space. However, a disadvantage is that it also introduces additional error due to the atmospheric correction. In this study we run MODTRAN for each data scene using the actual sun-view geometry but climatological AOD, water vapor column, and ozone information. In the future, we can utilize MODIS Aerosol Product (MOD04), MODIS Atmospheric Profile product (MOD07), and DEM data to improve the atmospheric correction accuracy of the Hyperion data and further improve the N2B coefficients.

Given the performance of the satellite derived N2B is similar to the laboratory spectra based N2B, we are also working on developing the VIIRS N2B coefficients using the same methods.

CHAPTER FOUR

4. DATA FUSION OF MODIS, MISR, AND VIIRS

By increasing the number of high quality retrievals available, the overall quality of the gap filled dataset will also be increased. The MODIS V006 product has become a daily product (still using all possible looks over a 16day period but weighting and emphasizing the day in question to produce a daily product). While this will help considerably to produce gap filled results on a weekly or monthly basis, the MODIS satellites are aging and by 2018 or so, only the MODIS Aqua is expected to be operating. This will be analogous to the period from 2000 – mid 2002 before the launch of Aqua, when only Terra was available. Salomon et al., (2006) showed that while the quality of the high quality retrievals remained consistent, the number of high quality retrievals globally was considerably less than when both MODIS Aqua and Terra observations were available. Therefore additional strategies are needed to produce sufficient high quality BRDF, albedo and NBAR retrievals worldwide after the demise of Terra.

One strategy is to merge additional data from other satellites into the processing stream. Combining data from multiple sensors can improve the BRDF retrievals by adding complementary viewing geometries (Jin et al., 2002; Samain et al., 2006). Jin et al. (2002) developed a synergistic approach of integrating BRDF parameters derived from MISR as *a priori* information with MODIS observations to derive *a posteriori* BRDF parameters. This method can reduce the relative BRF prediction error by up to 10% (Jin et al., 2002). In this study, we use this method plus a direct synergistic method

to fuse MODIS-Terra and MISR data to enhance the gap-filled snow-free dataset for the time period when only MODIS-Terra information was available.

As Terra and Aqua age and are no longer available, VIIRS data from Suomi-NPP will be the only multi-angle moderate resolution data available. Therefore to further extend the gap-filled dataset into the future, we can also combine MODIS and VIIRS directional observations to improve the data quality and increase the number of high-quality pixels, especially for the later years when the Terra data are no longer available.

4.1 Data

MISR, onboard the same platform as MODIS-Terra, acquires multi-angle observations using nine discrete cameras at fixed angles: a nadir plus 26.1, 45.6, 60.0, and 70.5 degrees in both forward and afterward directions along the orbit track. Its global coverage is achieved every nine days at the Equator and it acquires three or four overlaps in higher latitudes over a 16-day period. MISR has four bands in the visible and near infrared (NIR) (Table 3), which are similar to MODIS bands 1 to 4. For this study, the MISR Level 2 Land BRDF data (MIL2ASLS) in a Space Oblique Mercator (SOM) projection with a 1.1km resolution are re-projected to the Sinusoidal projection in tiles and resampled to 1km. The MISR Level 2 aerosol product (MIL2ASAE) is re-projected as well to provide cloud, cloud shadow and other information to weight the BRDF retrieval. The MODIS 500m surface reflectance data (MOD09GA-light) will be aggregated to 1km for the data fusion.

Table 3 Spectral specifications of MODIS, MISR, and VIIRS

MODIS		MISR		VIIRS	
No.	Interval (nm)	No.	Interval (nm)	No.	Interval (nm)
1	620 - 670	3	661 - 683	I1	600 - 680
2	841 - 876	4	847 - 886	I2, M7	846 - 885
3	459 - 479	1	425 - 467	M3	478 - 498
4	545 - 565	2	543 - 572	M4	545 - 565
5	1230 - 1250			M8	1230 - 1250
6	1628 - 1652			I3, M10	1580 - 1640
7	2105 - 2155			M11	2225 - 2275

The VIIRS sensor, onboard the Suomi National Polar orbiting Partnership (NPP) satellite, also has similar spectral bands to MODIS in visible and NIR (Table 3). The spatial resolution for the Moderate (M) bands is 750m, and is 375m for the Imagery (I). The NPP L2G-light 500m surface reflectance product NPP_DSRFLD_L2GD has three 500m Imagery bands: I1, I2, and I3, and nine 1km Moderate bands including the six bands M3, M4, M7, M8, M10, and M11 corresponding to MODIS. The 500m NPP data will be aggregated to 1km to produce a 1km fused product. Data fusion of MODIS+MISR and MODIS+VIIRS is processed tile by tile, and the tiles are mosaicked to global and re-projected to the 30arc second CMG grid to improve the gap-filled product.

4.2 Methods

To invert the RTLSR model, the eq. (2) can be written as (Li et al., 2001; Twomey et al., 1997):

$$M_{n \times 1} = K_{n \times 3} X_{3 \times 1} + E_{n \times 1} \quad (23)$$

Where M is the observation vector, K is the kernels, X is the model parameters to be derived, and E is the errors. The cost function of the *a priori* synergistic method (Jin et al., 2002) is:

$$cost(X) = (KX - M)'(KX - M) + \gamma(X - X_p)'(X - X_p) \quad (24)$$

Where X_p is the parameters derived from MISR/VIIRS, and γ is the weight of the *a priori* information. By comparing eq. (24) with eq. (23) we can see that, the *a priori* synergism method includes two pieces of information: the data fitting information from the MODIS observations, and the difference between the derived parameters and the *a priori* parameters. The γ controls the balance of the two parts of the information and thus it is an important subjective parameter. Jin et al. (2002) developed an information index based on eigenvalues of the kernel matrix, and based γ on the ratio of the information index between MODIS and MISR. But here, we use the ratio of the weight of determination (Lucht, W., and P. Lewis, 2000b) between MODIS and MISR/VIIRS observations to serve as the weight of the *a priori* information. The *a priori* synergistic method is only applied when MISR (or VIIRS) can produce a full inversion and MODIS also has sufficient observations (more than 7).

If the *a priori* synergistic approach fails due to insufficient MODIS observations or no MISR (or VIIRS) full inversions, then the direct synergism method, which directly combines MODIS and MISR (or VIIRS) directional observations, is attempted to avoid using the backup inversion algorithm.

These synergistic methods are introduced only if a full inversion cannot be retrieved based on MODIS observations alone. Due to multiple reasons, such as the differences of the spectral responses, spatial co-registration, the size of the footprints, and atmospheric correction methods, the errors introduced by the additional sensors may be larger than the information content they provide. Therefore, the same criteria (RMSE, weights of determination, etc.) as the MODIS operational BRDF product are used to check the synergistic results, and if a full inversion cannot be retrieved based on the criteria, the pixel will be rolled back to the poorer quality MODIS back-up magnitude inversion.

For the fusion of MODIS and MISR data, the MISR daily swath data in the SOM projection are first converted to Sinusoidal tiles and resampled to 1km. Then the cumulated MISR observations from a 16-day period are combined with the MODIS aggregated 1km surface reflectances to derive BRDF parameters. Only high-quality MISR BRFs (according to the QA in MIL2ASLS) will be used to derive *a priori* BRDF parameters, and observations for each camera are weighted by the per-camera cloud mask in MIL2ASAE.

As described in the Jin et al. (2002) paper, the differences in the blue bands of MODIS and MISR is very large due to their spectral specifications, so only the MISR bands 2, 3, and 4 are used for the MODIS and MISR data fusion.

This same method is used when combining MODIS and VIIRS (as the *a priori* information). There are two pairs of identical spectral ranges between the VIIRS

Imagery band and Moderate band: I2 to M7 and I3 to M10. Because the purpose of this research is to improve the 30arc second (about 1km at Equator) gap-filled product, only the moderate bands are selected to combine with MODIS data.

4.3 Discussion

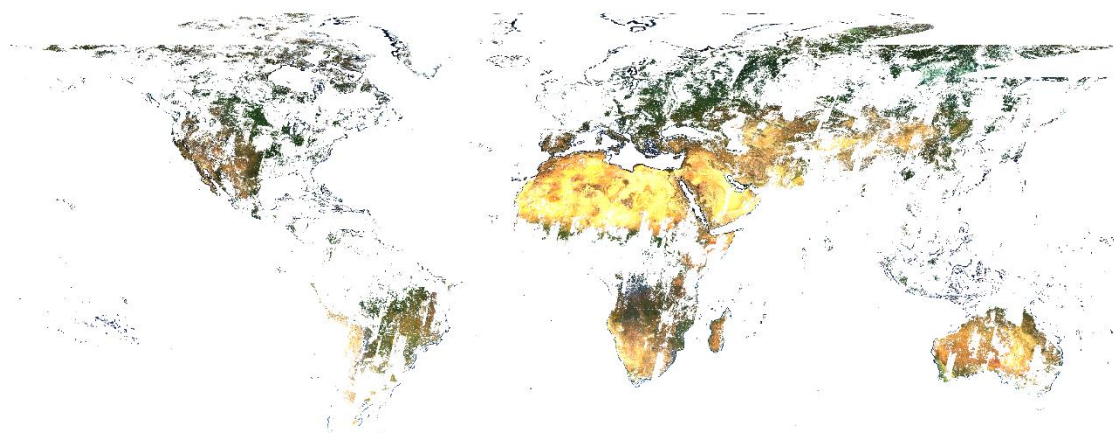
MODIS + MISR

To evaluate the ability of MISR to improve the MODIS BRDF product for the time period before the launch of Aqua, two days in 2001 are processed: Day of Year 025 (using observations from 025 to 040) and DOY 185 (185 to 200). The MODIS Terra-only and the MODIS Terra-MISR methods are processed separately to compare the QA flags. The number of improved pixels (magnitude inversion or fill value turned to full inversion) and an accounting of which synergistic method was used (*a priori* or direct synergism) is accumulated in Table 4. The “Potentially improved” column in Table 4 indicates instances when a full inversion is not possible from MODIS Terra-only but there are available MISR observations to potentially improve the MODIS BRDF retrieval.

The number of improved pixels changes between the different bands and the day of year, but the percentage of improvement is consistently around 28%, which means, in the case of MODIS Terra-only occasions where it is not possible to get a full inversion, adding MISR observations are 28% more likely to improve the BRDF retrieval (if there are MISR observations available).

Table 4 Statistics of MODIS (Terra)-MISR data fusion

DOY	MODIS band	Potentially improved	Improved by <i>a priori</i>	Improved by direct	Total improved
025	1	32590245	5096310 (15.64%)	4133097 (12.68%)	28.32%
	2	32106013	5013567 (15.62%)	4391203 (13.68%)	29.29%
	4	32223439	5141568 (15.96%)	4123912 (12.80%)	28.75%
185	1	19183717	3733137 (19.46%)	1648989 (8.60%)	28.06%
	2	17409365	3097768 (17.79%)	1813271 (10.42%)	28.21%
	3	18276414	3598157 (19.69%)	1604471 (8.78%)	28.47%

**Figure 24 True color composite of nadir MISR BRF accumulated between 185 and 200, 2001**

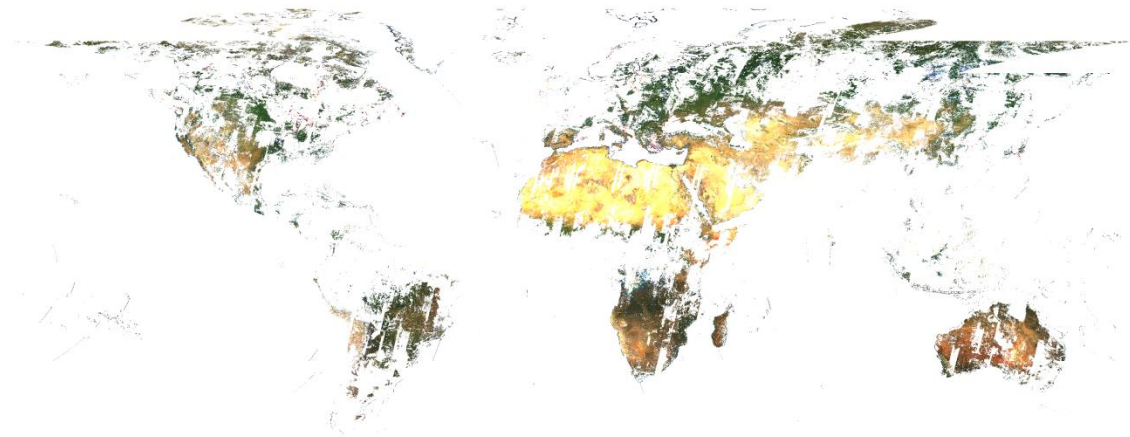


Figure 25 True color composite of MISR derived WSA (full inversion only) for 185, 2001

From Figure 24 we can see how many MISR observations are available during a 16-day period (clouds and snow are eliminated). And by comparing Figure 24 and Figure 25 we can see, for each pixel, that if clear MISR observations are available, it is likely that a full inversion can be retrieved due to MISR's unique 9-observation simultaneous viewing mechanism.

For an understanding of the spatial distribution of the MISR improved BRDF retrievals, QA flags and synergistic flags (indicating which synergistic method was used) are plotted in Figure 26. We can see more improvements in the winter than in the summer (northern hemisphere), and more improvements are distributed in Eurasia and Africa.

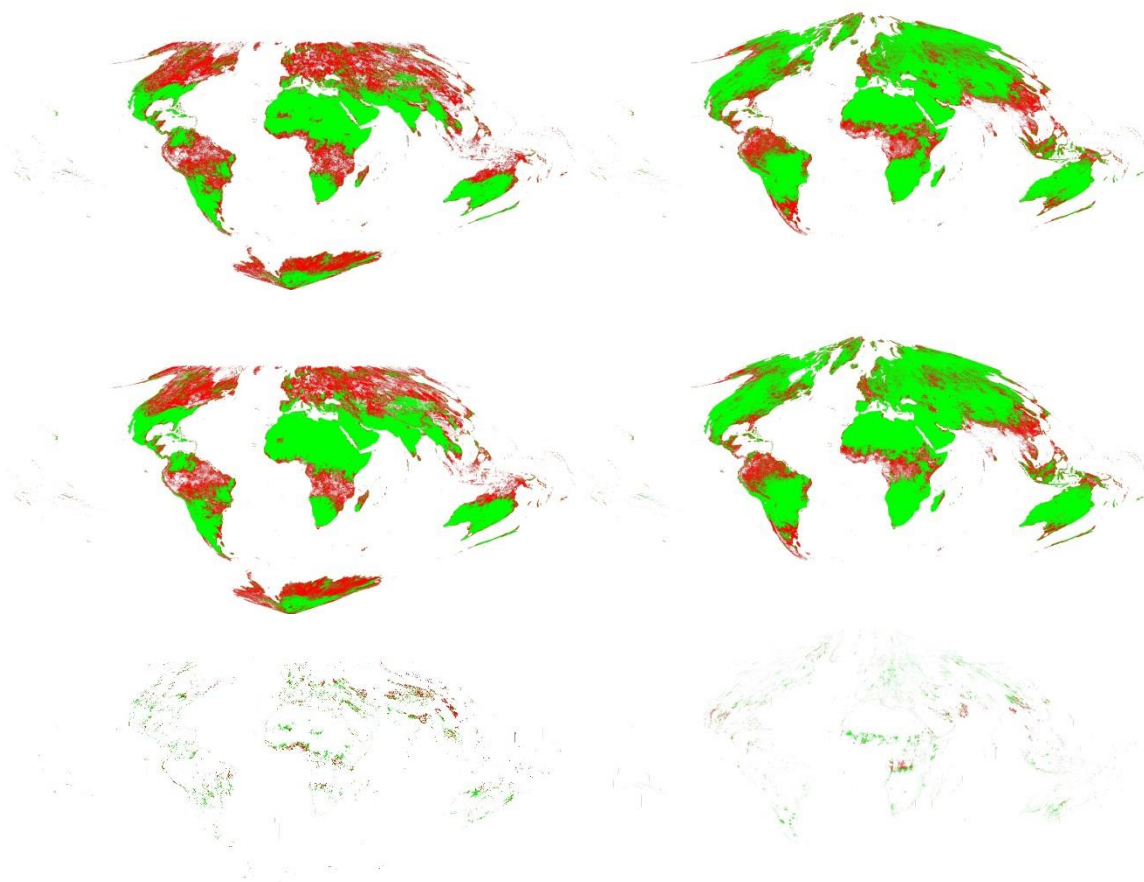


Figure 26 QA flags for MODIS Terra-only (top) and MODIS-MISR (middle), and synergistic flags (bottom) for MODIS band 1. QA Green: full inversion, Red: magnitude inversion. Synergistic flags Green: *a priori* synergism, Red: direct synergism. Left column: DOY 025, right: 185.

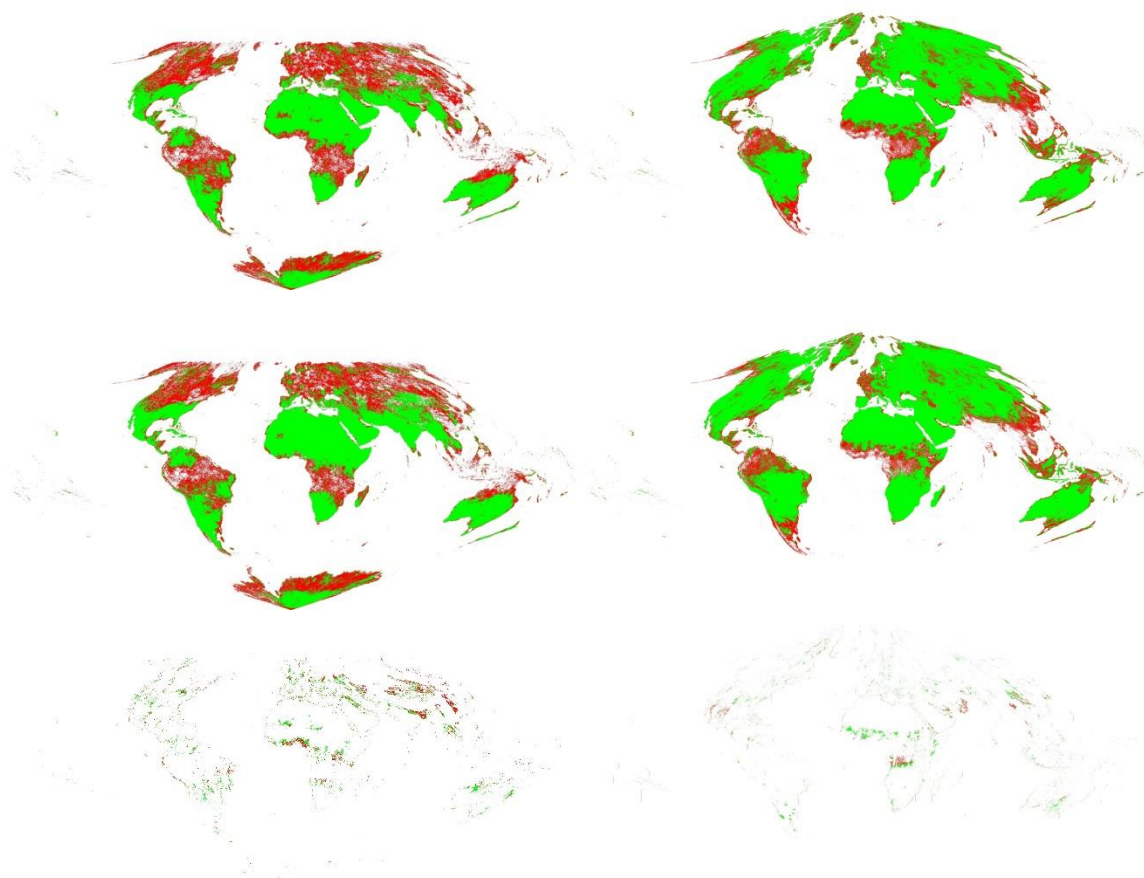


Figure 26 continued for MODIS band 2.

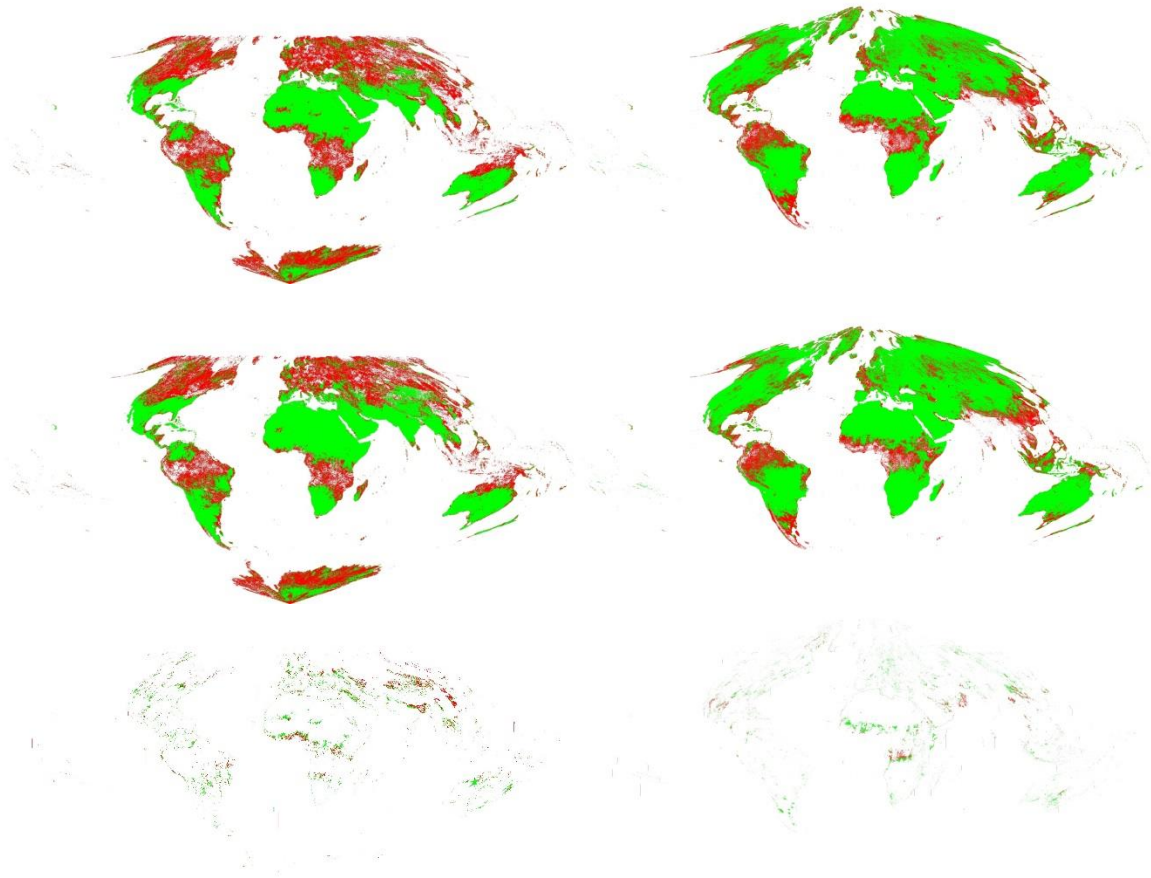


Figure 26 continued for MODIS band 4.

MODIS + VIIRS

VIIRS has a similar flight orbit, scan mechanism, footprint size, and spectral bands with MODIS, and as shown in Table 5, actually has more potential than MISR to improve the MODIS BRDF product when only MODIS Aqua is available. Although both Aqua and Suomi NPP are on an ascending sun synchronous orbit with an Equator crossing time of 13:30, and therefore the observations of MODIS Aqua and VIIRS are on the same viewing plane, they are not overlapping, and thus can be as supplements to each other to enrich the observation plane (Figure 27).

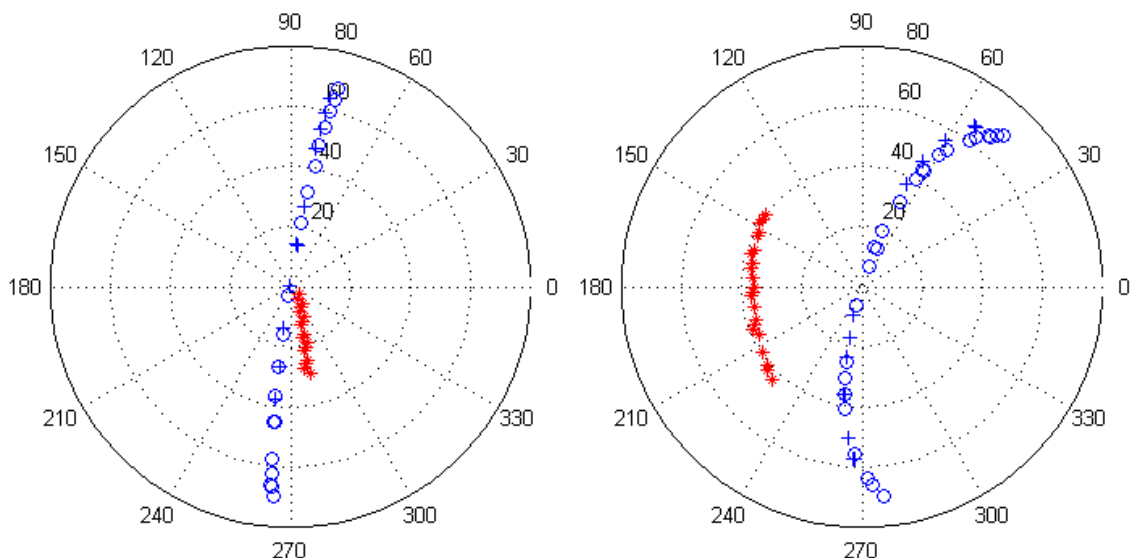


Figure 27 Observations of MODIS Aqua (plus) and VIIRS (circle) accumulated between 185 and 200, 2012. Red stars are sun positions. Left is selected from tile h19v07, and right is tile h12v03

Table 5 Statistics of the MODIS (Aqua)-VIIRS data fusion

DOY	MODIS band	Potentially improved	Improved by <i>a priori</i>	Improved by direct	Total improved
025	1	84838763	19155063 (22.58%)	19180729 (22.61%)	45.19%
	2	81183572	13286421 (16.37%)	17207236 (21.20%)	37.56%
	3	88176207	15336781 (17.39%)	17137546 (19.44%)	36.83%
	4	83896130	13882097 (16.55%)	17728131 (21.13%)	37.68%
	5	74564186	15306748 (20.53%)	18222815 (24.44%)	44.97%
	6	75622460	16139234 (21.34%)	20240886 (26.77%)	48.11%
	7	75282575	17617509 (23.40%)	19688339 (26.15%)	49.55%
185	1	54539298	18021098 (33.04%)	13562780 (24.87%)	57.91%
	2	49891055	11018789 (22.09%)	12055283 (24.16%)	46.25%
	3	61298730	17374168 (28.34%)	11568911 (18.87%)	47.22%
	4	53014937	13049077 (24.61%)	12133876 (22.89%)	47.50%
	5	49408940	10657441 (21.57%)	12178893 (24.65%)	46.22%
	6	52323876	11627348 (22.22%)	13822183 (26.42%)	48.64%
	7	50737823	12208694 (24.06%)	12775439 (25.18%)	49.24%

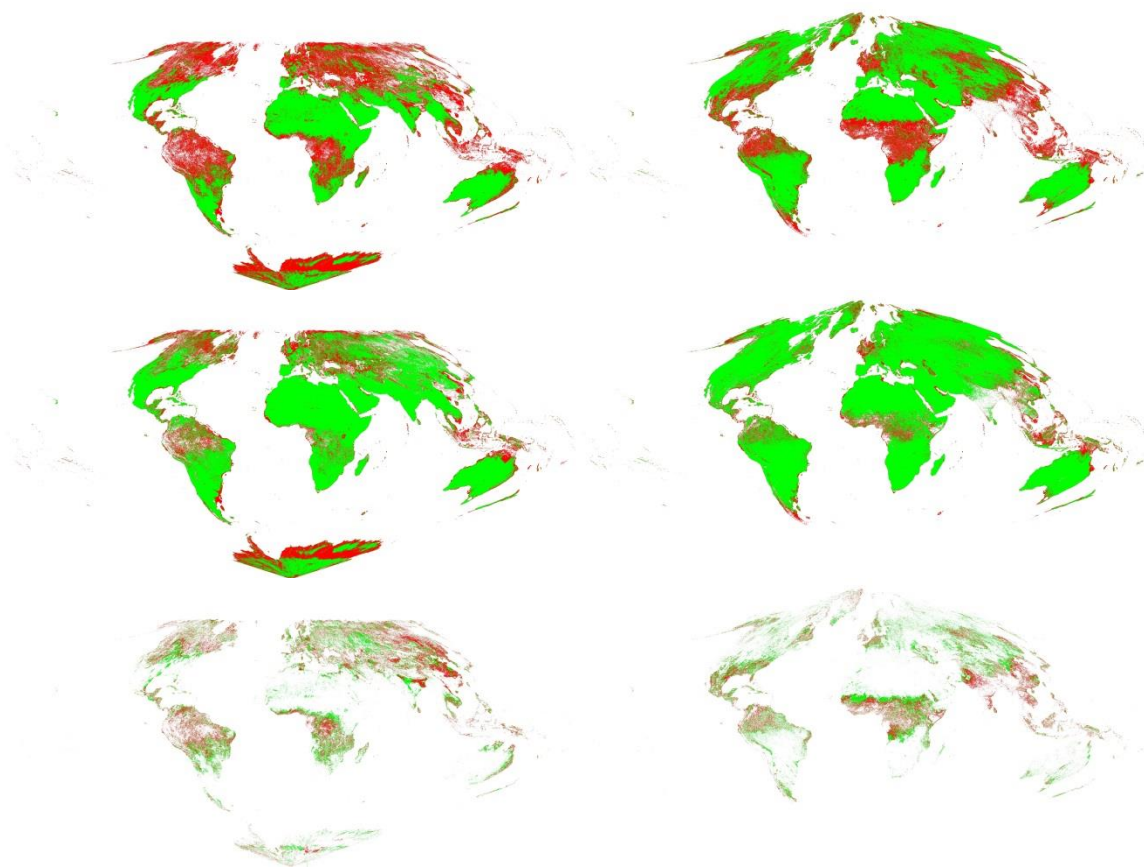


Figure 28 QA and synergistic flags for MODIS-VIIRS band 1. Left: DOY 025, right: 185

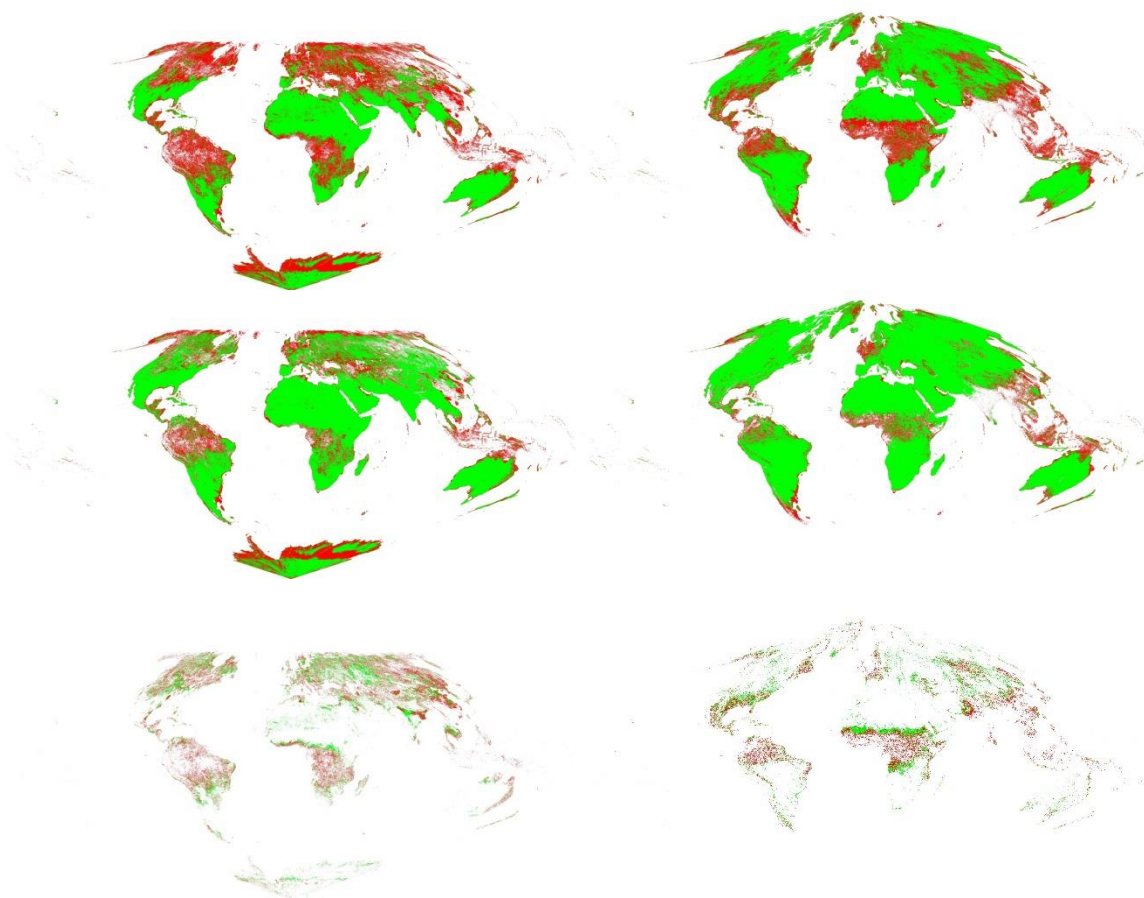


Figure 28 continued for MODIS band 2

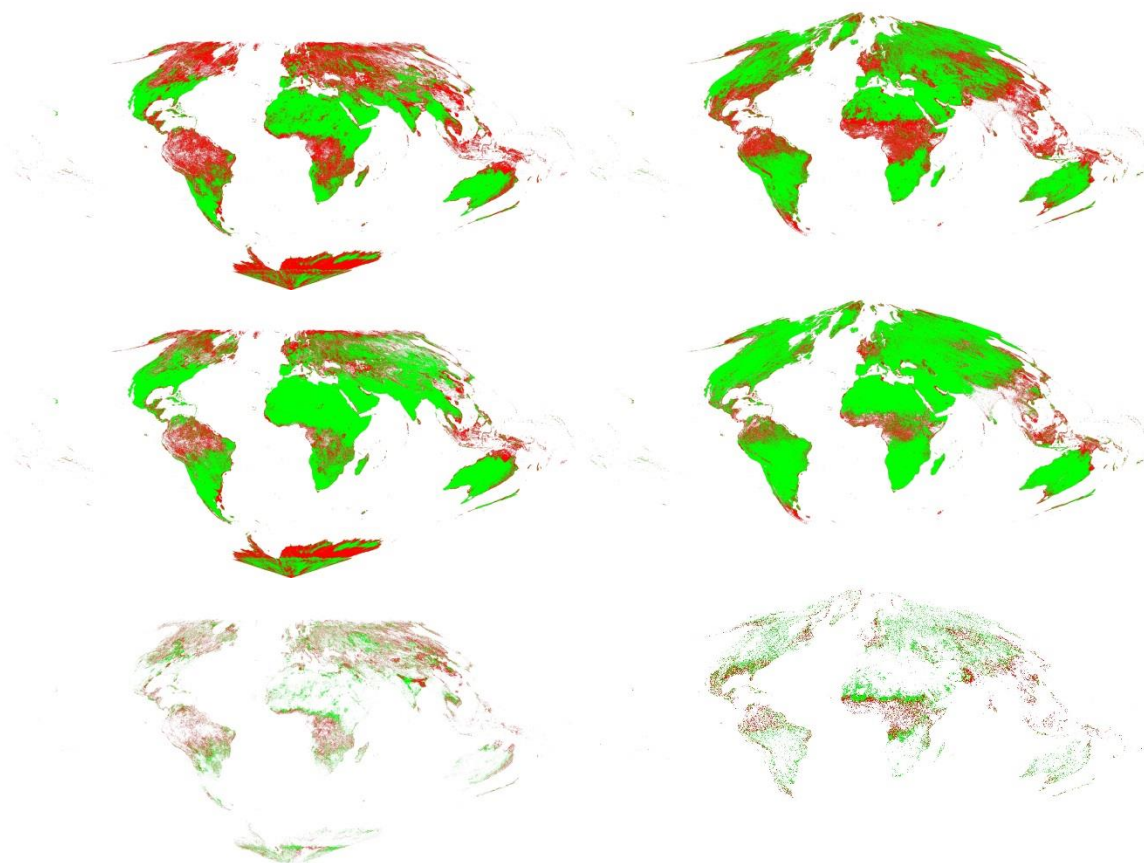


Figure 28 continued for MODIS band 3

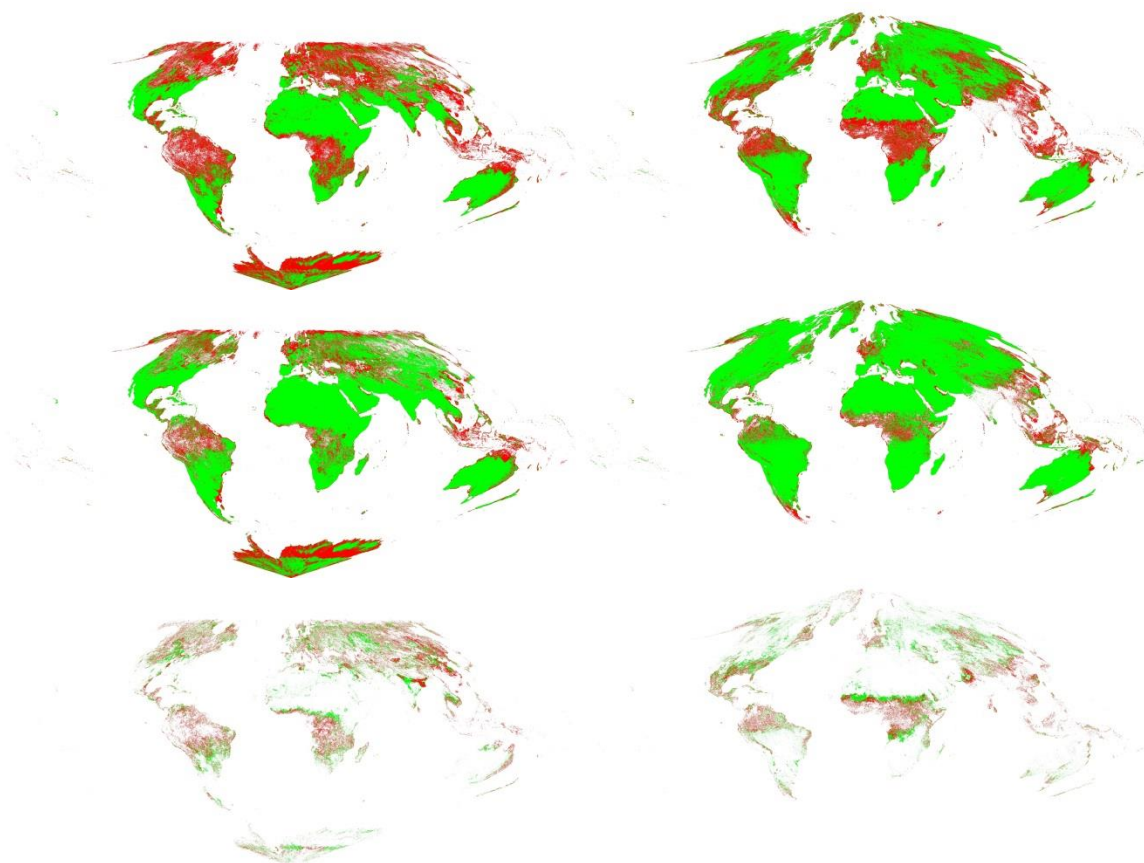


Figure 28 continued for MODIS band 4

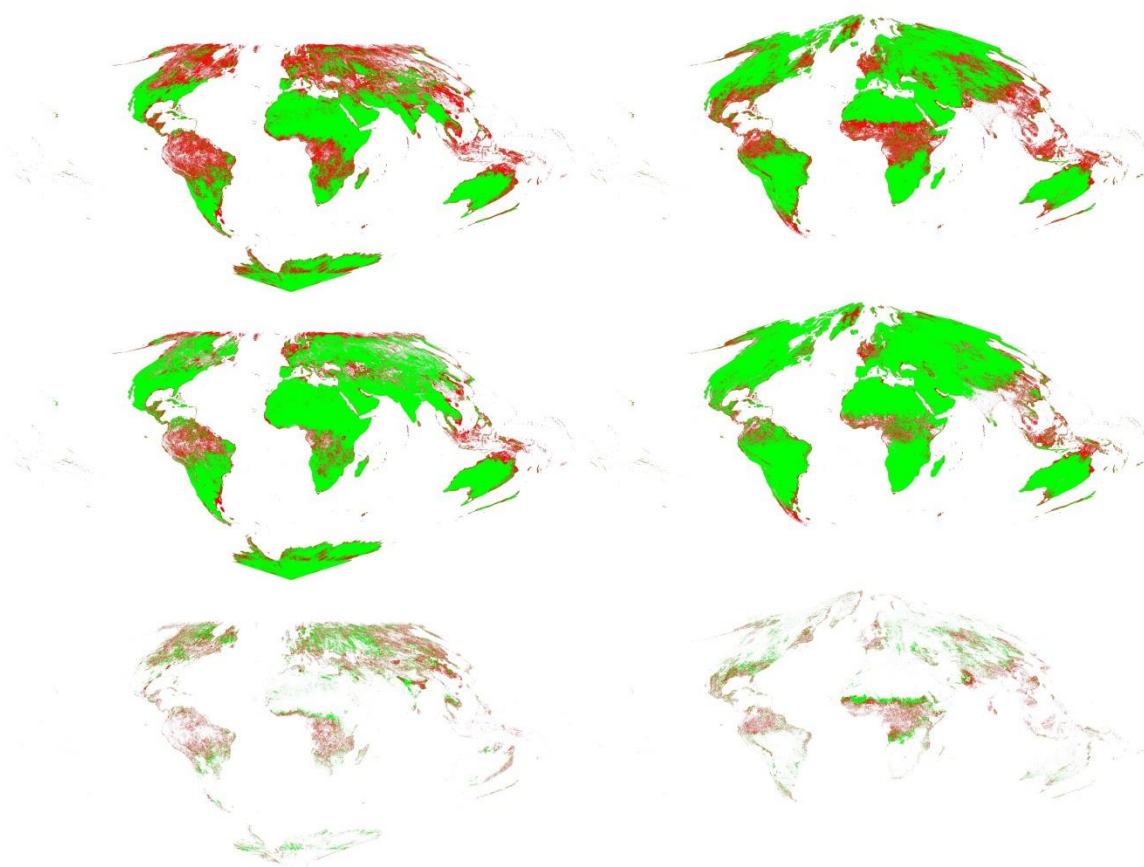


Figure 28 continued for MODIS band 5

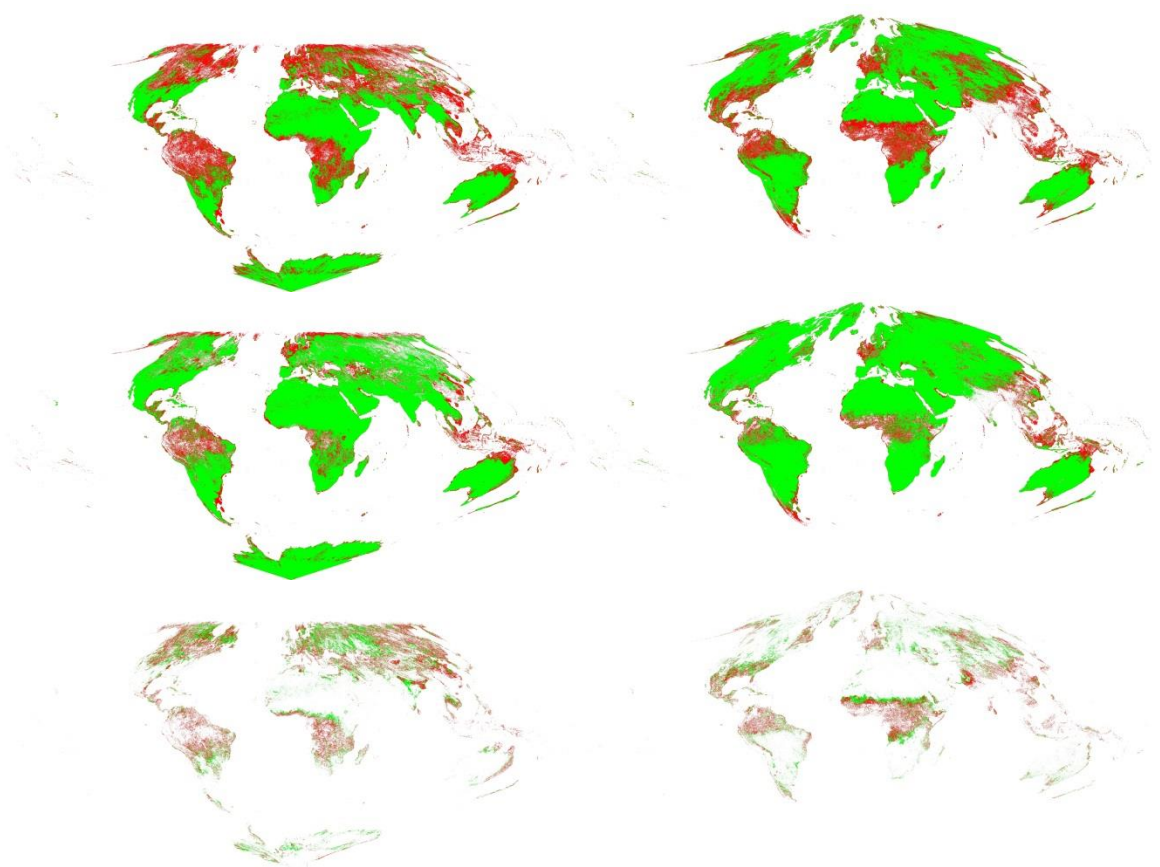


Figure 28 continued for MODIS band 6

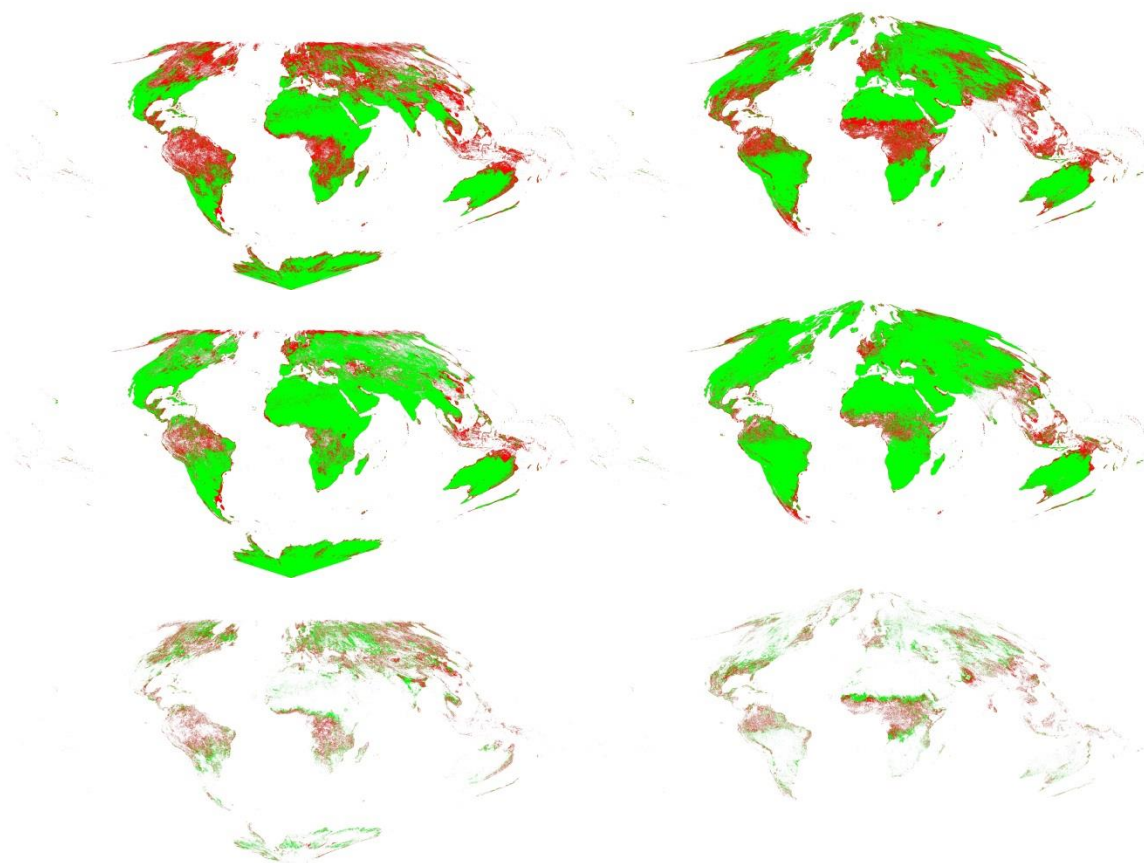


Figure 28 continued for MODIS band 7

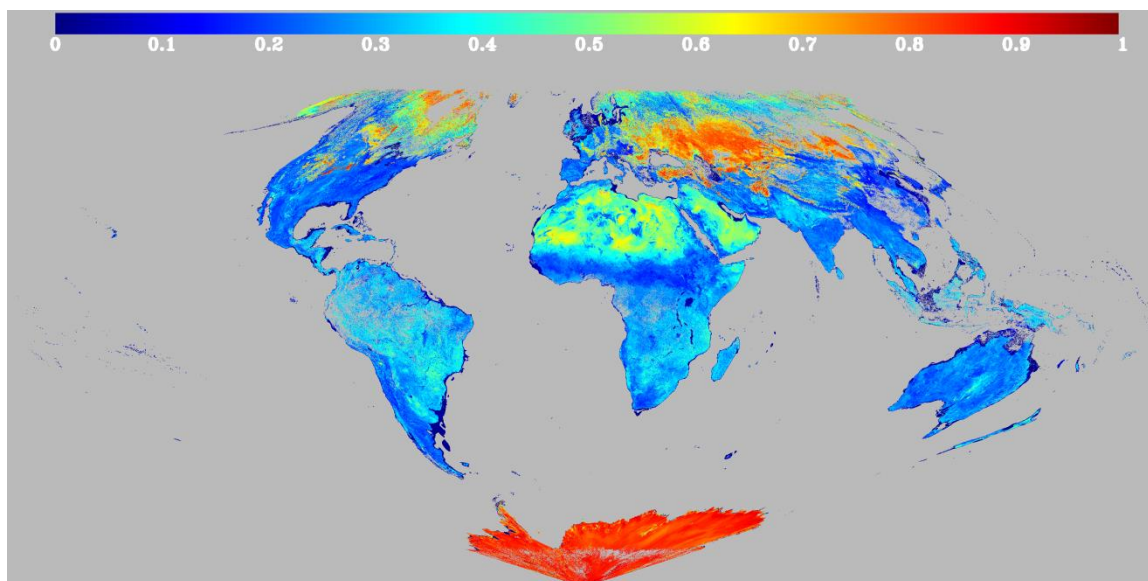


Figure 29 WSA NIR (band 2) derived from MODIS Aqua-only for 025, 2012

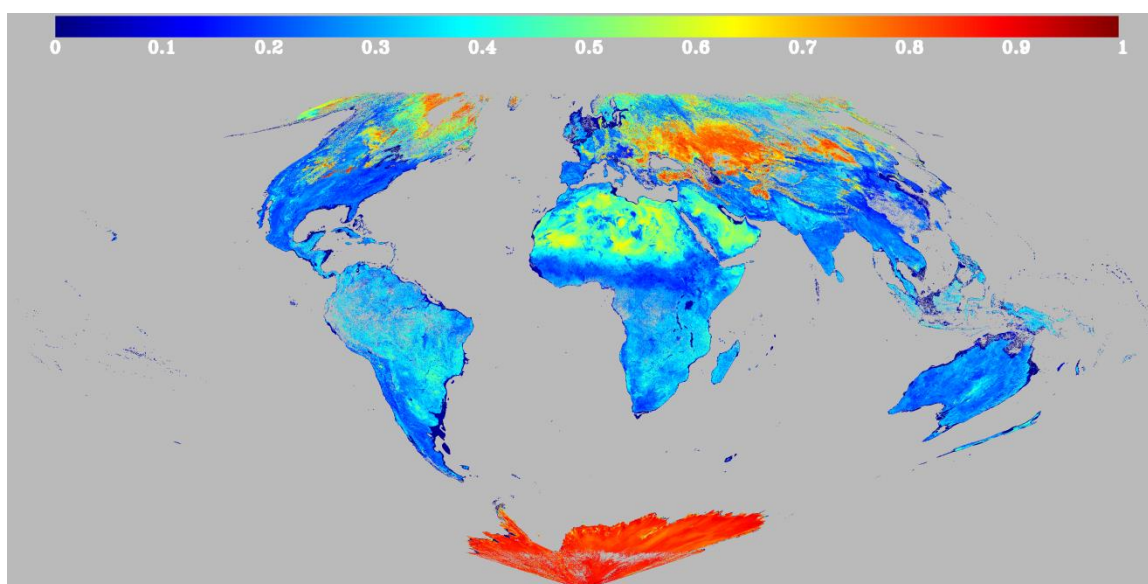


Figure 30 WSA NIR derived from MODIS Aqua and VIIRS for 025, 2012

Thus it is clear that adding VIIRS observations can significantly improve the MODIS Aqua-only BRDF retrievals. It transforms many pixels from low quality magnitude inversions into high quality full inversions (Figure 28), and also reduces the number of fill values (comparing Figure 29 and Figure 30, especially for Asia).

To further explore the potential of VIIRS to improve the MODIS BRDF product while MODIS Terra is still available, VIIRS observations are combined with both MODIS Terra and Aqua to retrieve BRDFs (Figure 31). The results show that, even during the MODIS Terra and Aqua era, adding VIIRS observations can still improve the BRDF retrieval quality.

The improvements are primarily concentrated in the equatorial region and in high latitude areas in winter. VIIRS has a wider scan swath with no gaps, so it has more observations than MODIS at the Equator. At high latitudes, large areas may be covered by ephemeral snow in winter. Because the RTLSR model (in the V005 periodic retrieval mode) only chooses either snow-free or snow observations in the 16-day period (snow covered observations are removed for a snow-free retrieval), ephemeral snow can reduce the quantities of observations significantly. Adding VIIRS observations (even potentially similar ones) can restore the number of observations required to meet the minimum requirement of the RTLSR model and thus potentially improve chances of a high quality full inversion BRDF retrieval.

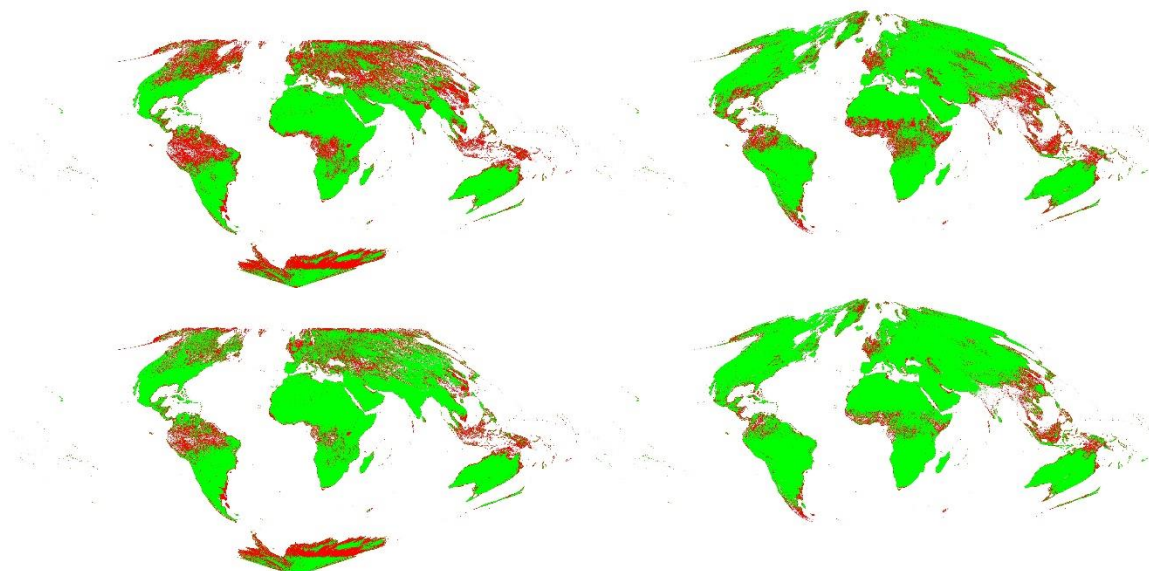


Figure 31 QA flags for Terra-Aqua (top) and Terra-Aqua-VIIRS (bottom) BRDF retrieval for band 2. Left: 025, 2012, Right: 185, 2012.

4.4 Conclusion

The *a priori* synergistic approach, which makes a balance between data fitting and *a priori* information, has been shown to be more accurate in some situations and stable to noise as compared to the direct synergistic approach (Jin et al., 2002). For MISR, this approach is guaranteed by its nine almost simultaneous observations which make sure that, as long as MISR clear observations are available, they are much more likely to be able to provide *a priori* BRDF parameters, especially when the observations are in the principal plane. The advantage of direct synergism is that it may increase the overall number of high-quality pixels. The *a priori* synergism involves data fitting solely on MODIS data but adjusted by *a priori* MISR/VIIRS parameters, which means, a minimum of MODIS observations is required. If a pixel reverts to the backup algorithm in the MODIS-only inversions, it may also fail with the *a priori* synergistic approach.

The direct synergism strategy can address this naturally by simply adding additional observations and thus potentially increase the number of fully inverted pixels. Because of this, we also use direct synergism as a second method to attempt to retrieve in cases where the *a priori* synergism failed.

Combining data from multiple sensors can bring in additional angular samples; however, it can also introduce additional noise due to differences in the spectral specifications, the atmospheric correction methods, spatial resolutions, and geographic co-registration. In this study, we only keep data fusion results when the information brought in is larger than the errors introduced, and thus are able to turn this pixel from a poorer quality magnitude inversion to high quality full inversion. We check both the RMSE and weights of determinations after each synergism attempt and only the synergistic results that meet the full inversion criteria are kept.

In conclusion, both MISR and VIIRS data can improve the MODIS BRDF retrieval significantly for time periods between 2000 to mid-2002 when only Terra was available and in the future when only MODIS Aqua is available. Furthermore, the addition of VIIRS data may improve the number of high quality retrievals when Terra, Aqua and Suomi-NPP are all used together. These data fusion processes can be made operational to aid in the improvement of the gap-filled BRDF product.

CHAPTER FIVE

5. ASSESSMENT OF THE IMPACT OF CHANGES IN THE INTRINSIC LAND SURFACE ALBEDO

While the challenges in producing high quality cloud-free, snow-free land albedo products from a variety of remotely sensed observations cannot be underestimated, the availability of such products for modeling and monitoring ecosystem health is crucial. We utilize the gap filled MODIS database to investigate the seasonal variability of the Amazon. The Amazon rainforests significantly influence the global climate, water, and carbon cycles. Many previous satellite-based studies have indicated that Amazon forests green up during dry seasons (Huete et al., 2006; Brando et al., 2010; Xiao et al., 2006; Myneni et al., 2007) while others (Samanta et al., 2010) have suggested that the majority of this greening signal is due to residual clouds in the satellite images. Most recently Morton et al., 2014 have suggested that the episodes of greening shown by the satellite-based studies are in fact artefacts due to variations in sun-view geometry. They went on to conclude that the Amazon forests are seasonally invariant in canopy structure and greenness. This unlikely conclusion is based on phenologies derived from a gap filling methodology (Vermote et al., 2009) that relates BRDF to NDVI and over-smoothes (and over simplifies) the dynamics of the Amazon forests. This paper highlights the importance of understanding the actual information content of extrapolated or gap filled datasets and utilizing quality flags appropriately. In this study, we will analyze the seasonal Nadir BRDF-Adjusted Reflectance (NBAR) derived Enhanced Vegetation Index (EVI) changes of Amazon forests at fixed solar zenith angles using both the gap-filled

BRDF/Albedo dataset prepared from MODIS V005 data and the MODIS V006 daily BRDF/Albedo high quality data, and assess the ability of the gap-filled datasets in maintaining the physical information and quality of the original data.

5.1 Data

MODIS V006 500m BRDF/Albedo product (MCD43A) is processed daily for the year 2005 for tiles h11v09 and h12v09 (Figure 32). Due to strong cloud contamination, only a very limited number of high quality pixels of NBAR can be found during each single time period. Monthly composites of the high quality data are generated for monthly comparisons. Even for monthly composites, during the wet seasons when the Intertropical Convergence Zone is over the Amazon, there are very few available high quality pixels obtained, so only June (the beginning of dry season) to September (the end of dry season) are analyzed (Figure 33 to Figure 36).

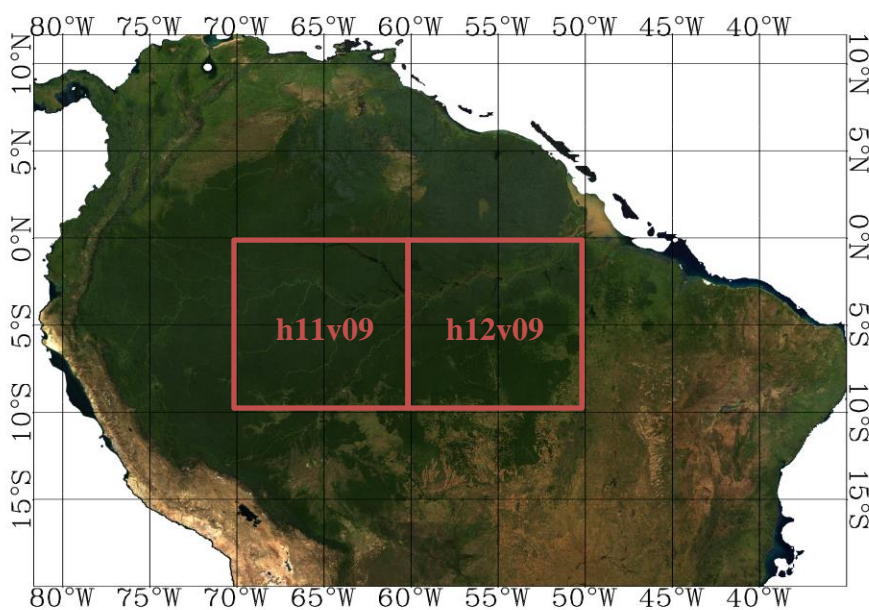


Figure 32 Location of the tiles h11v09 and h12v09

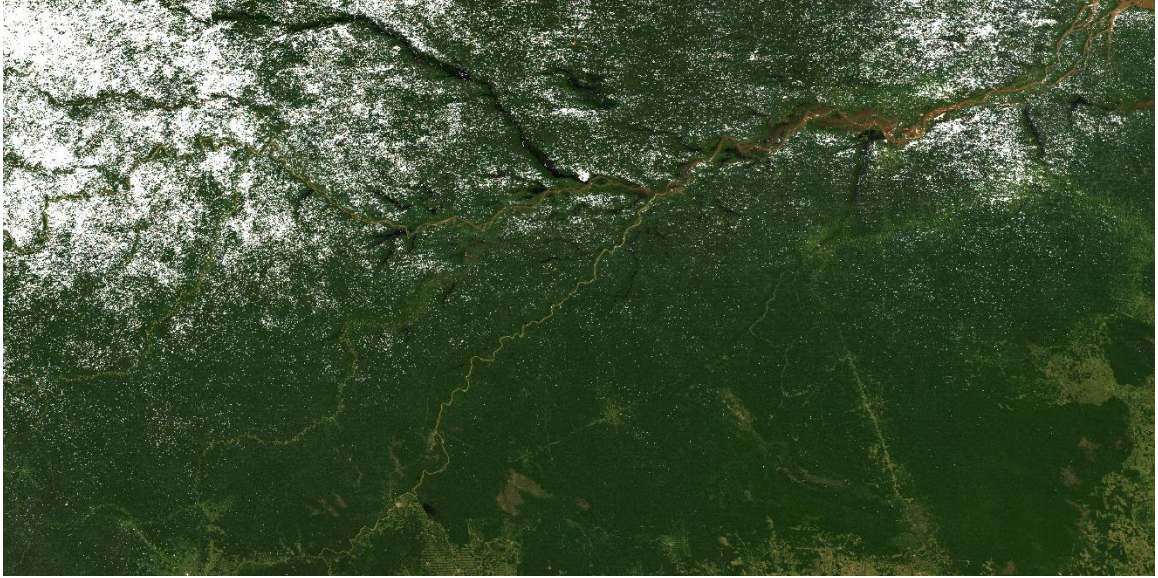


Figure 33 Monthly composite of daily V006 MCD43A NBAR at a solar zenith angle of 30 degree for tiles h11v09 & h12v09 for DOY 151-180 (June), 2005



Figure 34 Monthly composite of daily V006 MCD43A NBAR at a solar zenith angle of 30 degree for tiles h11v09 & h12v09 for DOY 181-210 (July), 2005



Figure 35 Monthly composite of daily V006 MCD43A NBAR at a solar zenith angle of 30 degree for tiles h11v09 & h12v09 for DOY 211-240 (August), 2005



Figure 36 Monthly composite of daily V006 MCD43A NBAR at a solar zenith angle of 30 degree for tiles h11v09 & h12v09 for DOY 241-270 (Sept.), 2005

5.2 Discussion

Enhanced vegetation index (EVI) is an index of canopy photosynthetic capacity and is calculated by eq. (25). (Huete et al., 2002).

$$EVI = 2.5 \times \frac{\rho_{nir} - \rho_{red}}{\rho_{nir} + 6 \times \rho_{red} - 7.5 \times \rho_{blue} + 1} \quad (25)$$

Where ρ_{nir} , ρ_{red} , ρ_{blue} here are NBAR for NIR, red, and blue band respectively. We use MODIS BRDF parameters to calculate NBAR at a fixed solar zenith angle of 30 degree (instead of the usual local solar noon provided in MCD43A4) to eliminate any so called “artefacts” of sun-view geometry.

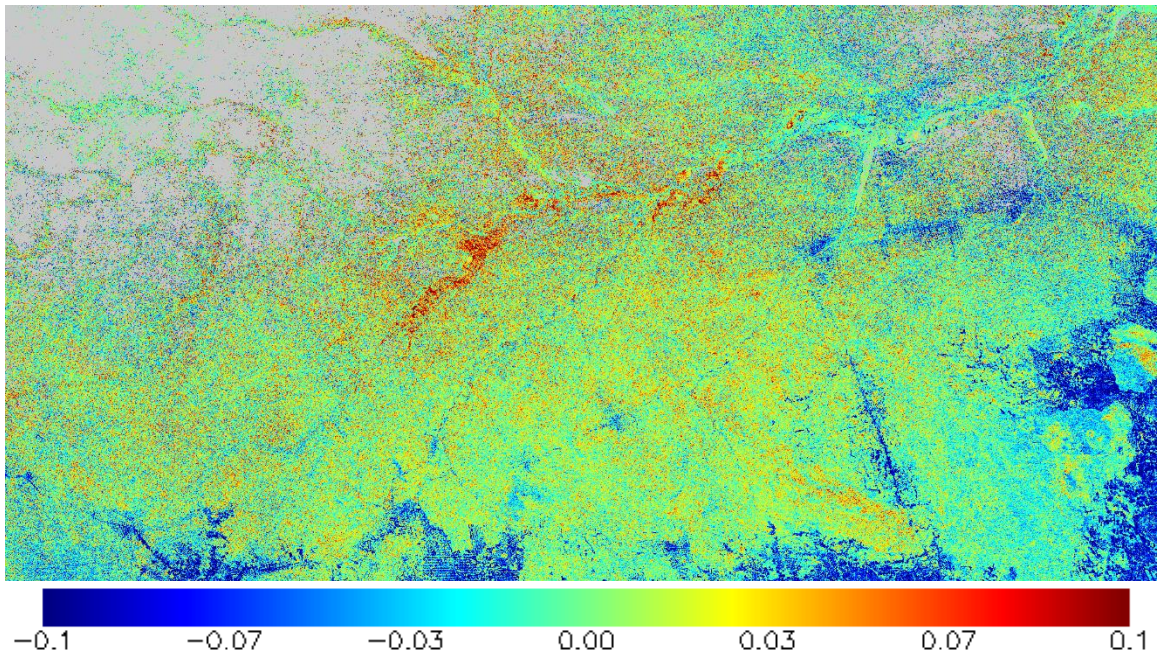
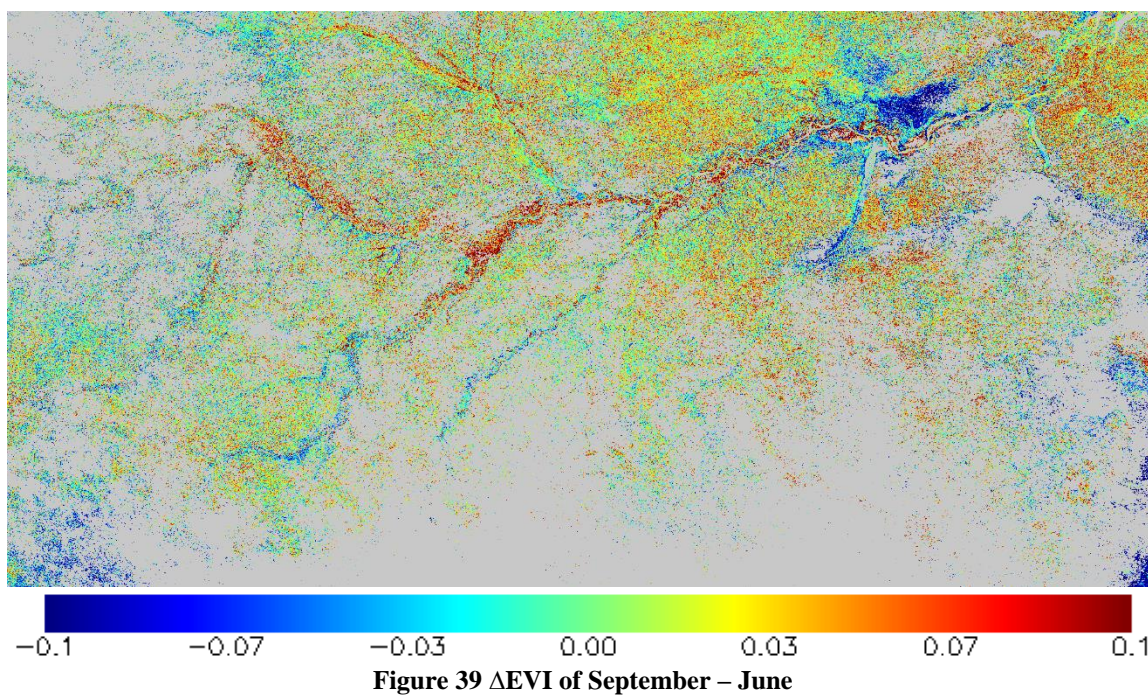
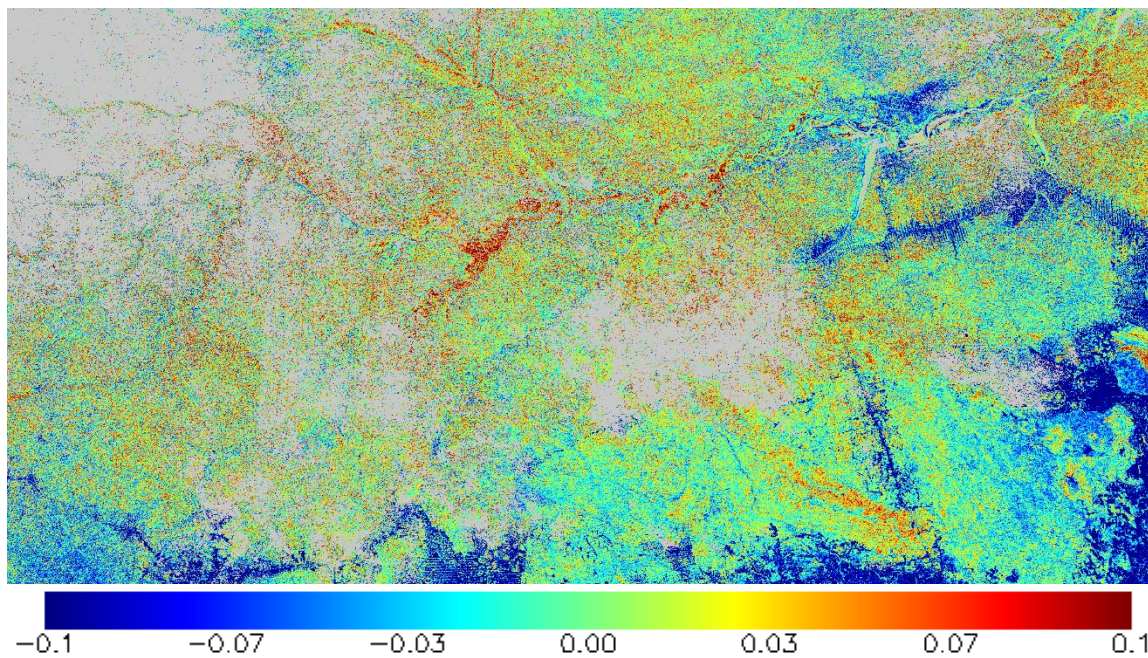


Figure 37 Δ EVI of July – June



For visual comparison, Δ EVI between the monthly composites are generated. We can see, except for land cover disturbed areas, the forest pixels to the north of the region

are generally greening up between June and September. For a quantitative analysis, however, it is not appropriate to simply compare the whole tile averages because the availability of high quality pixels in the different monthly composites is quite different, and the spatial distribution of the topography and precipitation regimes is very uneven throughout the Amazon forest. To address this problem, Davies et al. analyzed the EVI temporal variation in an equatorial transect using a 6-year composite of NBAR- EVI calculated from high quality V005 MCD43A1 with a fixed solar zenith angle (SZN) of 30 degree (Davies et al., 2014). We repeated the process of Davies et al., 2014 but using the V005 gap-filled BRDF/Albedo dataset instead of Davies et al.'s multi-year composite to see if we still retain similar trends of forest greening during dry seasons. Davies et al., 2014 uses 2003 – 2008 high quality composite dataset, so in this study we chose the 2005 gap-filled dataset for comparison. Furthermore 2005 experienced a major drought in the Amazon forests, which led to low streamflows and high fire frequency (Zeng et al., 2008).

A subset of the global gap-filled dataset is investigated between 12 °N and 20 °S, and 82 °W and 30 °W (Figure 40). The V005 MODIS land cover product MCD12Q1 (the IGBP layer) is used to exclude the non-forest pixels. The NBAR-EVI profiles are calculated for each latitude and longitude at 1 degree resolution with Non-forest pixels masked. Considering the spatial distribution of available forest pixels, longitude profiles are taken between -77 °W and -52 °W, and latitude profiles are taken from 5 °N to 13 °S.

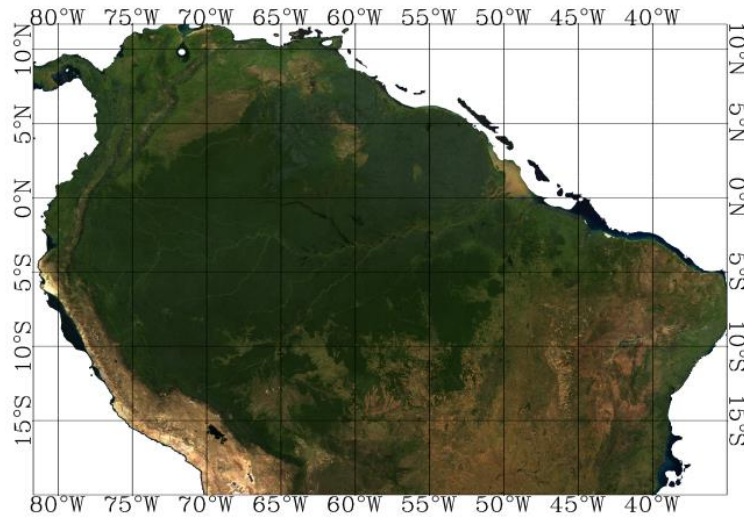


Figure 40 Subset of study area.

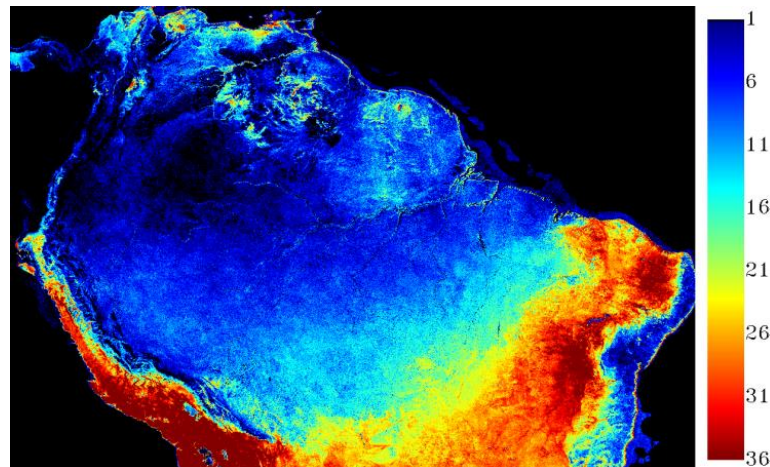


Figure 41 Number of high quality retrievals of V005 MCD43D through the year 2005

According to previous studies, the magnitude of the forest greening is related to the number of dry months in a year (Huete et al., 2002; Xiao et al., 2006). During dry seasons, the evaporation is limited and clouds are fewer so MODIS can collect more clear sky observations to derive high quality BRDF retrievals. Therefore, the number of periods with high quality pixels in one year should be roughly correlated to the number of dry months. A map of counts of high quality periods in 2005 (Figure 41) is generated for reference while analyzing the EVI variations along longitudinal or latitudinal transects.

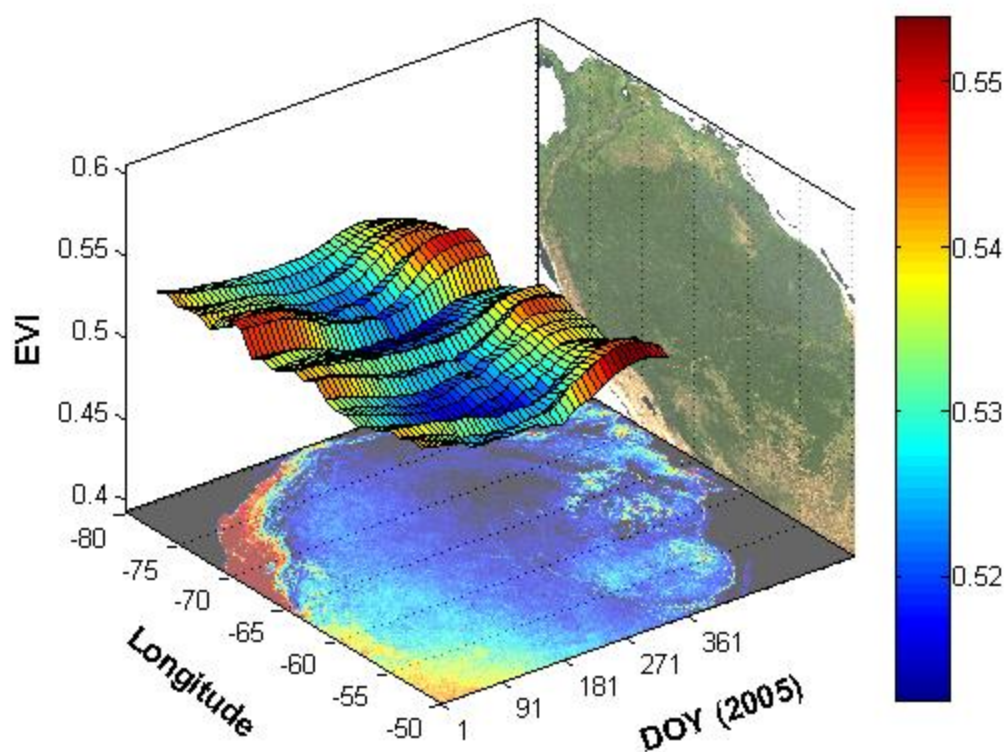


Figure 42 Longitude EVI profiles of the gap-filled dataset for Amazon forests. Figure 41 is projected to the XY plane, and the Amazon NBAR map is projected to the YZ plane for reference. From the XY plane we can roughly see how many dry months are in the year for a profile, and from the YZ plane we can see where a profile is located and what forest pixels it crosses.

Since we have enough valid pixels in the temporally and spatially complete gap-filled dataset, we can select one year of the gap-filled dataset and compare with high quality composites made over multiple years of previous satellite based studies. From the longitude NBAR-EVI profiles of the 2005 gap-filled dataset at a fixed solar zenith angle of 30 degree (Figure 42) we can see, when the profile crosses forests with short dry periods (west parts), the temporal curves are steep, which means the forests start greening up late and stop greening up early. The Figure 42 shows that western Amazon forest has shorter dry periods while the eastern has longer dry periods, which agrees with Davies et

al., 2014, Sombroek et al., 2001, and Xiao et al., 2006. From the maximum EVI values of Figure 42 we clearly see three domes from west to east, which means the central forests have lowest maximum annual EVI. This phenomenon coincides with the compositing results of Davies et al., 2014 and Xiao et al., 2006.

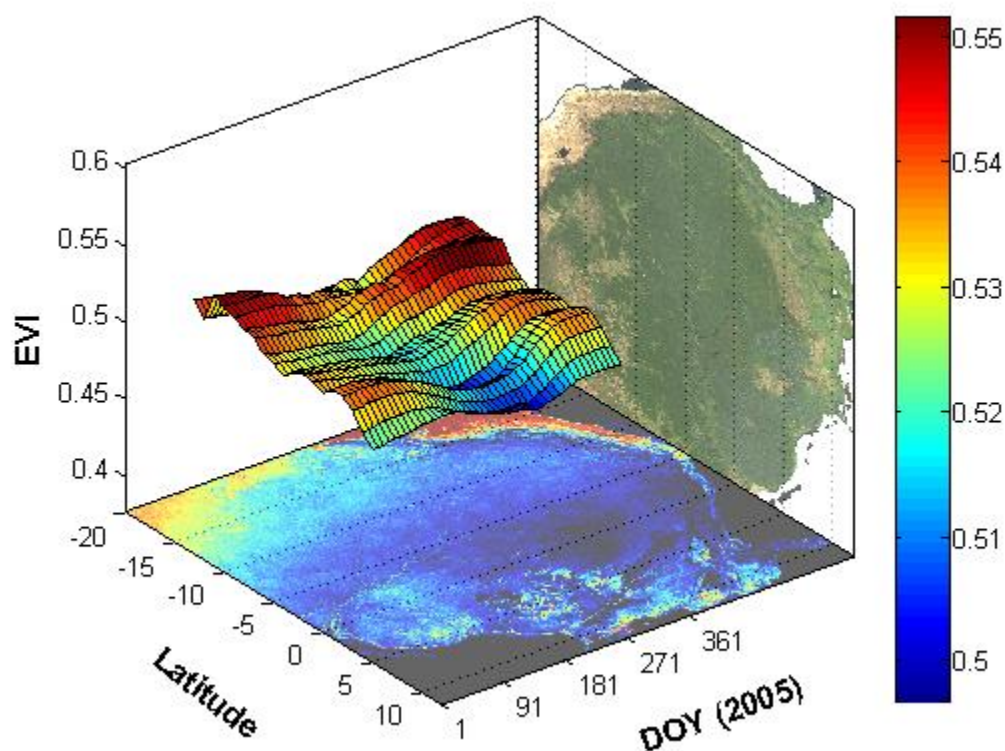


Figure 43 Latitude EVI profiles of Amazon forests

Latitudinal NBAR EVI profiles are also investigated (Figure 43). At higher latitudes (0° - 5° N), the lower parts of the curves are wide, which means the forests at these latitude bands green up later than lower latitudes. This is because the first dry period starts in September for the northeast part of the Amazon forest while for the other parts of the forest it usually starts in June or July (Xiao et al., 2006, fig. 3a). At lower latitudes (-5° S to -15° S), the NBAR EVIs are apparently greater than at higher latitudes,

which coincides with the longer length of the dry periods in the southern part (Sombroek et al., 2001 fig. 2; Xiao et al., 2006 fig. 2).

The Amazon forest experienced a severe drought in 2005 (Aragao et al., 2007). The gap-filled dataset EVI for multiple years can be used to investigate the impact of the 2005 drought. From Figure 44 we can see the annual EVI changes between 2003 and 2004 are not significant, and the time series curves are flat. But from Figure 45 we can see an apparent EVI increase in 2005 during the dry season, especially for the western part, which is coincident with that the drought intensity peaked mainly in southwest and central forest (Saleska et al., 2007). But after that, the EVI drops rapidly in the wet seasons in both 2005 and 2006. An interesting phenomenon is that, during subsequent 2006 dry seasons, the EVI were significantly increased again (Figure 46, Figure 48), which is consistent with the terrestrial water storage change (Chen et al., 2009, Fig. 3) and might be caused by higher precipitation in June 2006 (Figure 49): after the severe drought in 2005, the Amazon forest became more water-limited, and the rich rainfall in Jun 2006 (52.8% increase than the mean of 2004 and 2005) relieved the drought situation and stimulated the Amazon forest greening up significantly. The long term impact of the 2005 drought is further exhibited in 2007, when the situation has returned to normal and the EVIs are lower than 2005 in both the wet seasons and dry seasons (Figure 48).

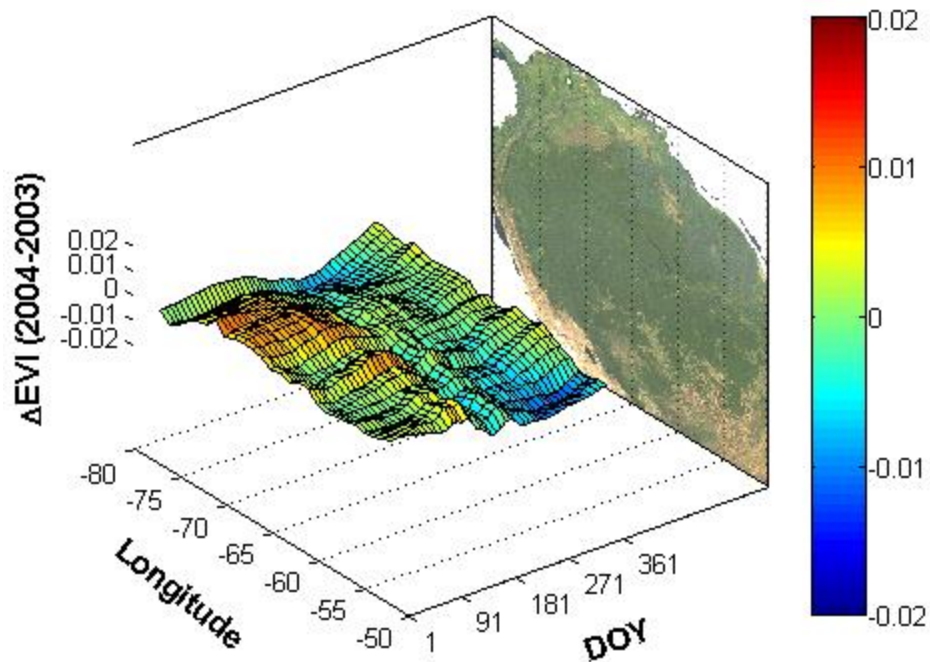


Figure 44 ΔEVI of 2004 – 2003 for longitude profiles

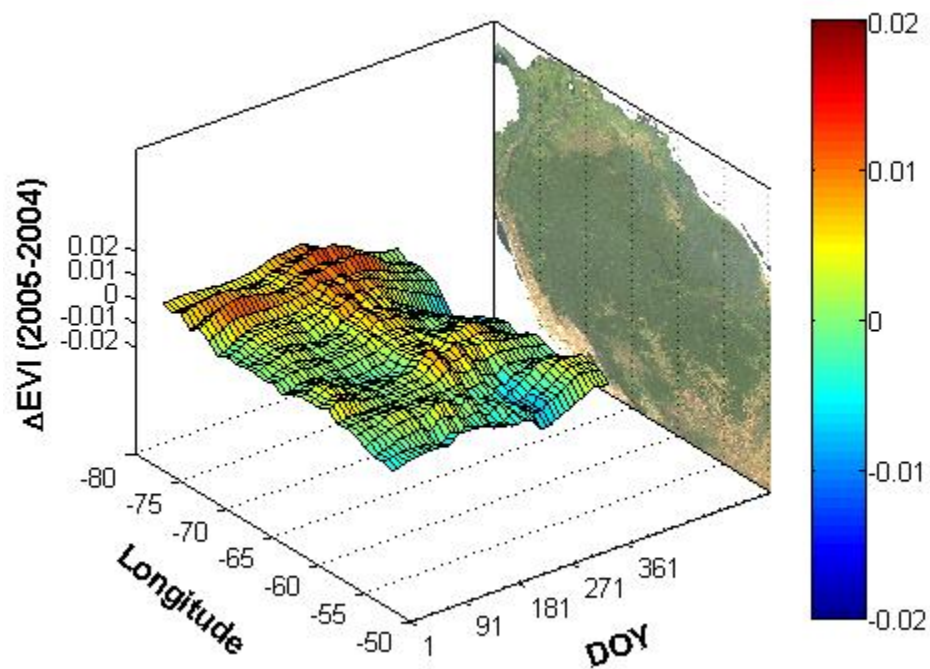


Figure 45 ΔEVI of 2005 – 2004 for longitude profiles

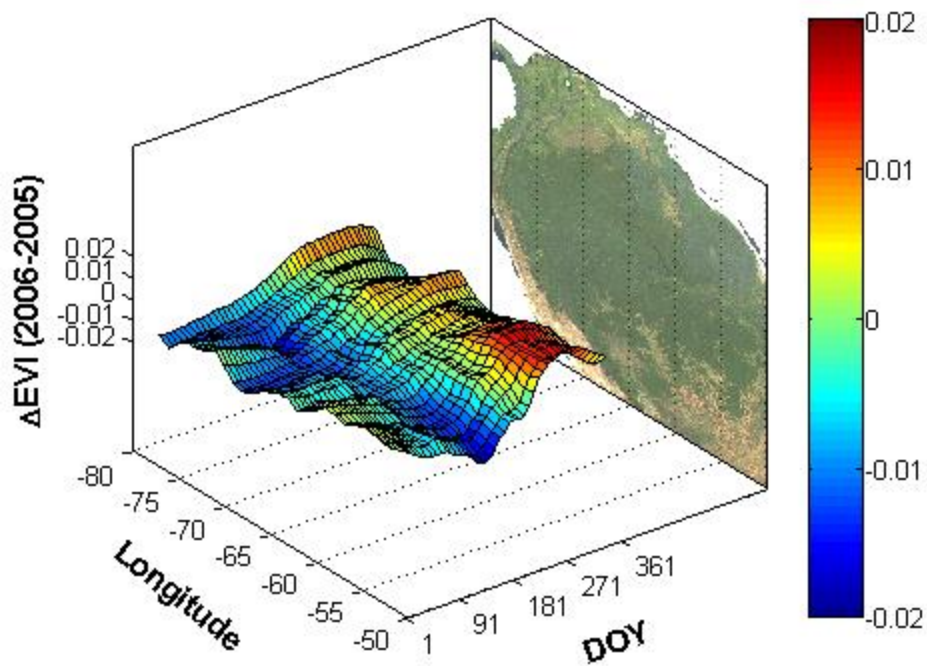


Figure 46 ΔEVI of 2006 – 2005 for longitude profiles

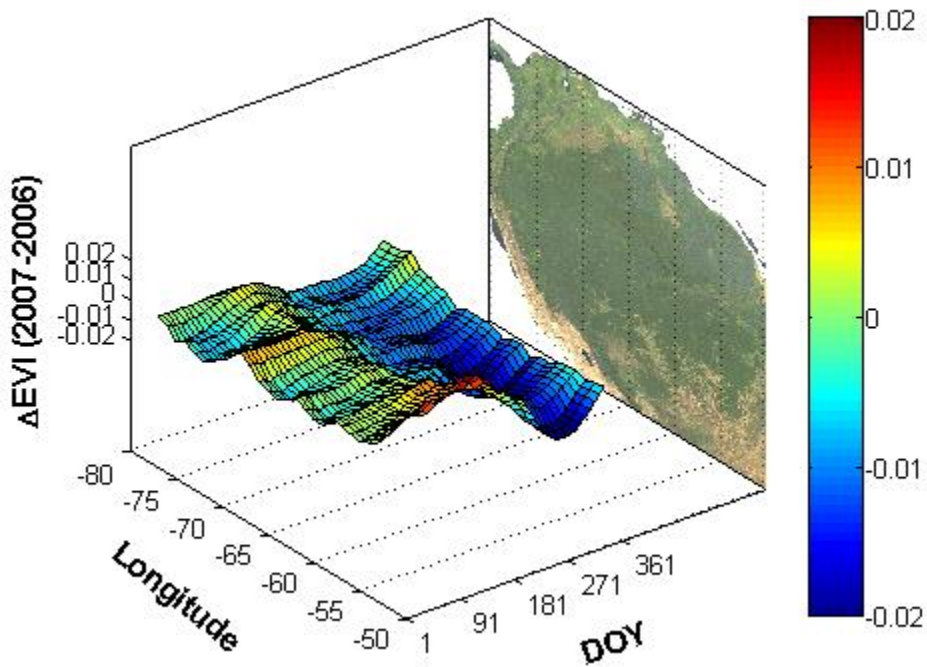


Figure 47 ΔEVI of 2007 – 2006 for longitude profiles



Figure 48 Time series of average EVI of the entire Amazon forest of the gap filled dataset

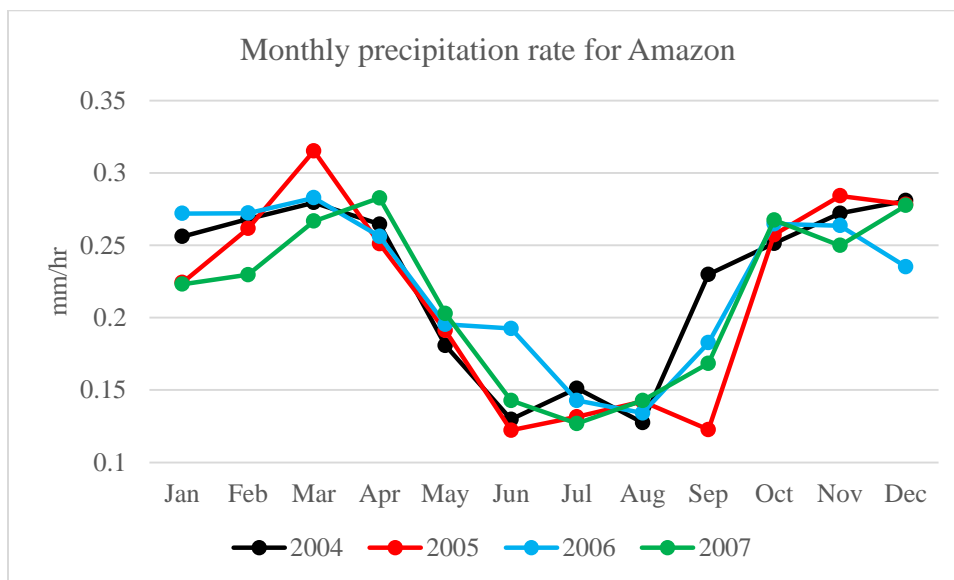


Figure 49 Monthly precipitation rate for Amazon. Data are from The Tropical Rainfall Measuring Mission (TRMM) Monthly 0.5 x 0.5 3A12 (v007). Each time period is averaged from area between 5° N - 15° S, and 75° W - 50° W.

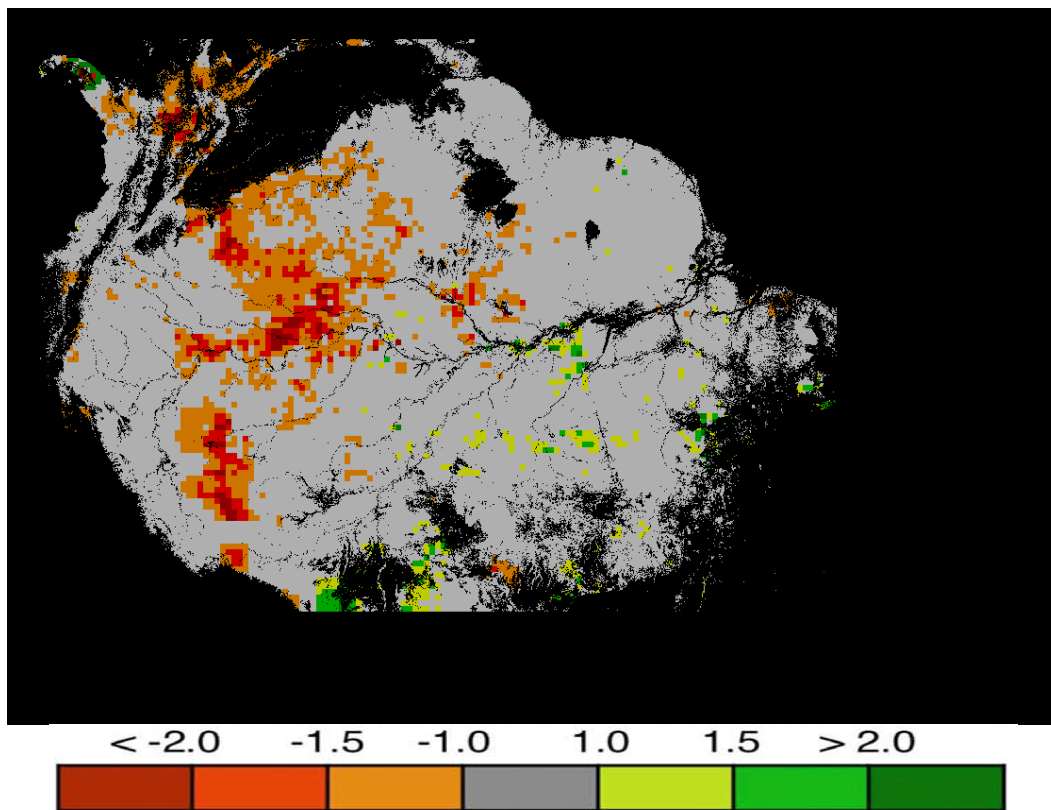


Figure 50 Precipitation 2005 JAS standardized anomalies. Data are from TRMM monthly precipitation data (3B43) of 2001-2005.

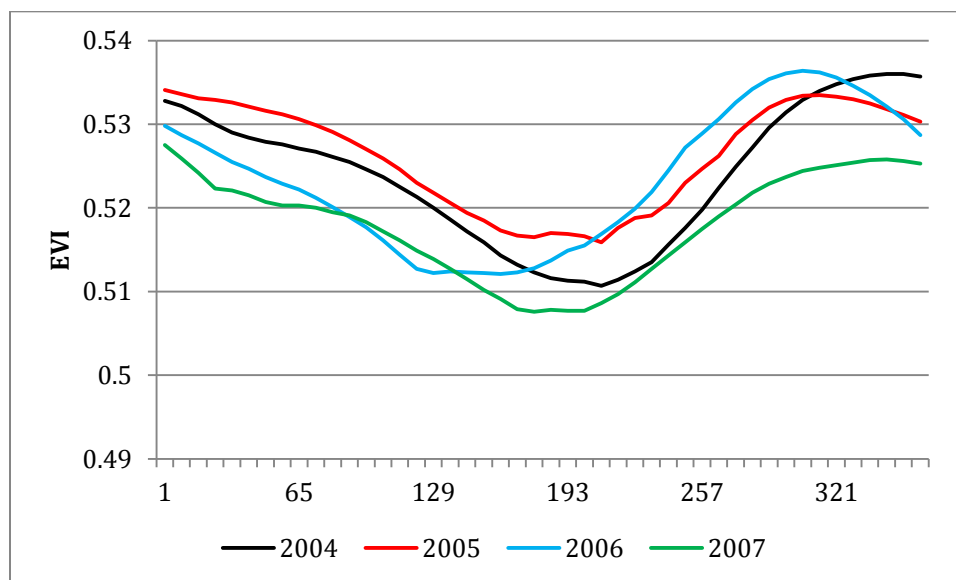


Figure 51 Time series of average EVI of the drought-stricken pixels.

The precipitation 2005 July to September (JAS) standardized anomalies (Figure 50) are calculated for the Amazon forests using monthly precipitation data of 2001-2005 from TRMM. We can see the drought-stricken pixels are concentrated in the western forests. Similar EVI variation trends as those EVI averages obtained for the entire Amazon forest are produced (Figure 51) when the analysis is based only on the drought-stricken areas (pixels with precipitation JAS standardized anomalies < -1.0).

We also analyzed the mean WSA in the NIR band pixel for the entire Amazon forest s, and obtained similar seasonal variation trends as found with the EVI (Figure 52).

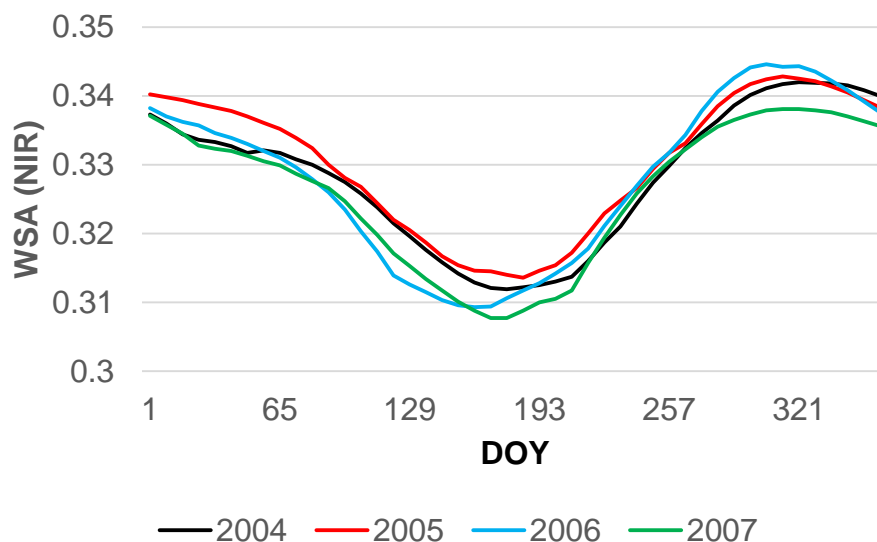


Figure 52 Time series of average WSA in NIR band of the entire Amazon forest of the gap filled dataset.

5.3 Conclusion

Similar trends of NBAR EVI variation for a fixed solar zenith angle are obtained over the Amazon Forest when using the temporally and spatially gap-filled

BRDF/Albedo dataset as compared to using high-quality-only multi-year composite data. Both of these strategies indicate that small but significant EVI variations occur during the dry and drought seasons and are consistent with previous satellite-based studies and in-situ measurements from eddy covariance towers (Huete et al., 2006; Restrepo-Coupe et al., 2013).

In addition, by investigating the gap-filled dataset averaged for the entire Amazon forest for the years 2004 – 2007, the 2005 drought is detected and the spatial distribution of the drought agrees with other studies. The small green-up during the initial portion of the dry season illustrates that normally the Amazon forest growth is mainly driven by sunlight. However, this research also shows that the main limitation factor can be shifted to precipitation under some situations such as during a severe drought. But in all of these cases the Amazon forest is not invariant as Morton et al., 2014 claim.

Therefore, this assessment results show that the gap-filled BRDF/Albedo dataset prepared here maintains the quality of the original MODIS BRDF/Albedo product (unlike the oversmoothing achieved with the Vermote et al., 2009 method used by Morton et al. 2014). However, use of the QA of the gap-filled dataset is still highly recommended given the accuracy differences of the different gap-filling methods discussed in chapter 2.

This gap-filled dataset is developed based on the V005 MODIS MCD43D product. The MODIS BRDF/Albedo product will be processed daily (still using 16 days of observations for each retrieval) in V006, however, the gap-filling techniques developed here for V005 will still all be applicable to the V006.

CHAPTER SIX

6. SUMMARY

Given the significance of the satellite based land surface anisotropy product for climate studies, and the general requirements for high quality gap free snow free albedo datasets, this study has developed a global spatially and temporally complete, cloud free, snow free BRDF, Albedo and NBAR dataset. This dataset is provided with 7 MODIS land bands and 3 broadbands, at 30 arc second spatial resolution and 8-day temporal resolution. Temporal fitting techniques (augmented with spatial fitting, and spatial smoothing methods for less than 3% of the global land pixels) are utilized to make the MODIS MCD43D product temporally and spatially complete, and QA flags are provided for each pixel for each band to indicate which method was used and what the quality level was. Extensive assessments show a good agreement between the filled values and original high quality values excluded for testing. However different gap filling methods have different accuracy levels, so it is important to check the QA flags when using the dataset.

To enhance this gap-filled dataset, we also developed new N2B conversion coefficients based on satellite hyperspectral data. We were interested in evaluating if it was possible to improve the broadband albedo values of the gap-filled dataset by improving the MODIS N2B because the N2B coefficients we currently use for satellite data were developed based primarily on laboratory spectra. However, we only found minor improvements when comparing satellite derived broadband albedos developed with the new N2B coefficients with actual broadband field measurements at multiple

ground flux tower sites in multiple land cover types. The converted shortwave broadband albedo is very close to that converted by the currently operationally used N2B coefficients, even though the two sets of coefficients themselves are completely different. There are still some potential to improve the satellite based N2B method, and we will work on that in the future as these coefficients are need for the use of MISR and/or VIIRS data.

We also explore the option of the improving the gap-filled data sets by combining MODIS with MISR, or MODIS with VIIRS data to improve the data quality and to increase the number of high quality pixels available. The MODIS and MISR data are combined to improve the dataset for the period between 2000 and 2002, when the MODIS Aqua had not yet launched. MODIS Aqua and VIIRS are combined to evaluate the product's quality in the future when the MODIS Terra will no longer available. A direct synergism method and an *a priori* synergism method are used to combine these MODIS, MISR, and VIIRS observations. Combining data from multiple sensors can introduce additional angular samples; however, it can also introduce additional noise due to differences in the spectral specifications, the atmospheric correction methods, spatial resolutions, and geographic co-registration. Here we use a simple criterion to check if the additional information is greater than the additional error: whether adding the additional observations can turn the pixel from a poor quality magnitude inversion or fill value to a high quality full inversion. The results show that, adding MISR can improve the MODIS Terra BRDF retrieval, especially for the winter when the number of MODIS observations is reduced due to snow. Furthermore the results indicate that adding VIIRS can not only

significantly improve the MODIS Aqua-only case, but also has potential to improve the retrieval quality when both Terra and Aqua are still available. Because of its wide scan swath and no gaps between two adjacent swathes, VIIRS improves the availability of pixels in the equatorial areas.

With the new gap filled products established, we applied the gap filled product to a tropical Amazon case to evaluate whether the gap-filled BRDF/Albedo dataset can maintain the quality of the original high quality data and still capture the EVI variation. Due to persistent cloud cover the Amazon represent an extremely stressing case for optical sensor data. The variation over Amazon forests, we retrieved is also compared with other previous satellite based studies. The results show that, after correcting for sun-view geometry influences, the EVI still reveals seasonal variations. The EVI variation trends we get from the gap-filled dataset agree well with Davies et al., 2014's results, which use a multi-year composite of high quality MODIS BRDF data. The EVI averages of the gap-filled dataset for the entire Amazon forest are investigated, and the 2005 Amazon drought is clearly detected when comparing the annual time series of mean EVI for 2004, 2005, 2006, and 2007. Also, the significant increase of the EVI in the second half 2006 that is observed in the mean EVI time series is coincident with the rich rainfall at the beginning of this dry season. These results hold even when only the drought affected pixels are investigated (not just averages of the Amazon forest). This study shows that the gap-filled dataset is capable of capturing inter annual EVI changes even for the ITCZ area, which is strongly contaminated by clouds and where only very limited satellite observations are available. This is an advantage of the gap-filled dataset over the

multi-year composite dataset that the latter cannot be used to analyze annual variations because the results are from multiple years. However, using single year satellite data with gaps is simply impossible for Amazon not only because of the limited observations, but also because the availability of observations in different time periods is quite different in spatial distribution, which makes it inappropriate for comparison between different periods.

The MODIS BRDF product has been proven as a high quality product by various efforts, and this assessment (in chapter 5) shows the gap-filled dataset maintains the quality of the original MODIS BRDF product. The gap-filled dataset provides an alternative data source beyond the multi-year composites that researchers usually use, and it can be used to do analyses that the multi-year composite datasets cannot be used for, particularly in regions of excessive cloud contamination such as the Amazon forest. Therefore, the gap-filled dataset provides good data source for the ecological community and has a potential to help researchers quantify the dynamics of regions such as the tropical forest ecosystems.

The importance of this research rests not only the production of global BRDF and albedo time series, uncontaminated by cloud and snow effects, to serve as initialization fields for climate and biogeochemical models at higher spatial and temporal resolutions, but in an identification and assessment of key intrinsic land surface albedo and vegetation phenology variations that have occurred over the Earth (and particularly the tropics) during the past decade and a half.

BIBLIOGRAPHY

- Aragao, L. E. O., Malhi, Y., Roman-Cuesta, R. M., Saatchi, S., Anderson, L. O., & Shimabukuro, Y. E. (2007). Spatial patterns and fire response of recent Amazonian droughts. *Geophysical Research Letters*, 34(7), L07701. doi: 10.1029/2006GL028946
- Brando, P. M., Goetz, S. J., Baccini, A., Nepstad, D. C., Beck, P. S., & Christman, M. C. (2010). Seasonal and interannual variability of climate and vegetation indices across the Amazon. *Proceedings of the National Academy of Sciences of the United States of America* 107(33), 14685–14690.
- Cescatti, A., B. Marcolla, S. K. S. Vannan, J. Y. Pan, M. O. Román, X. Yang, P. Ciais, R. B. Cook, B. E. Law, G. Matteucci, M. Migliavacca, E. Moors, A. D. Richardson, G. Seufert, C. B. Schaaf (2012). Intercomparison of MODIS albedo retrievals and in situ measurements across the global FLUXNET network, *Remote Sensing of Environment*, 121, 323–334.
- Charney, J., W. J. Quirk, S. H. Chow, and J. Kornfield (1977). A comparative study of the effects of albedo change on drought in semi-arid regions, *Journal of the Atmospheric Sciences*, 34, 1366–1385.
- Chen, J. L., Wilson, C. R., Tapley, B. D., Yang, Z. L., & Niu, G. Y. (2009). 2005 drought event in the Amazon River basin as measured by GRACE and estimated by climate models. *Journal of Geophysical Research: Solid Earth* (1978–2012), 114(B5). doi: 10.1029/2008JB006056
- Chopping, M. Schaaf, C.B., Zhao, F. Wang, Z., Nolin, A.W., Moisen, G.G., Martonchik, J.V., and Bull, M. (2010). Forest Structure and aboveground biomass in the southwestern United States from NASA moderate resolution remote sensing, in review.
- Chopping, M., C. B. Schaaf, F. Zhao, Z. Wang, A.W. Nolin, G.G. Moisen, J. V. Martonchik, M. Bull (2011). Forest structure and aboveground biomass in the southwestern United States from MODIS and MISR. *Remote Sensing of Environment*, 115, 2943–2953.
- Davies, K., Huete A., Restrepo-Coupe, N., Sun, Q., Schaaf, C (2014). Amazon Rainforest Greening Across a Longitudinal Equatorial Transect (manuscript in preparation).
- d'Entremont, R. P., Schaaf, C. B., Lucht, W., & Strahler, A. H. (1999). Retrieval of red spectral albedo and bidirectional reflectance using AVHRR HRPT and GOES satellite observations of the New England region. *Journal of Geophysical Research: Atmospheres* (1984–2012), 104(D6), 6229–6239.

Dickinson, R. E., and B. Hanson (1984). Vegetation-albedo feedbacks, in *Climate Processes and Climate Sensitivity*, Geophysical Monograph Series, vol. 29, edited by J. E. Hanson and T. Takahashi, pp. 180–186, American Geophysical Union, Washington, D.C.

Ellwood ER, Temple SA, Primack RB, Bradley NL, Davis CC (2013). Record-Breaking Early Flowering in the Eastern United States. *PLoS One* 8(1): e53788. doi:10.1371/journal.pone.0053788.

Fang, H., S. Liang, H. Kim, J.R. Townshend, C.B. Schaaf, A.H. Strahler, and R.E. Dickinson (2007). Developing a spatially continuous 1 km surface albedo data set over North America from Terra MODIS products. *Journal of Geophysical Research*, 112, D20206.

Friedl, M.A., McIver, D.K., Hodges, J.C.F., Zhang, X.Y., Muchoney, D., Strahler, A.H., Woodcock, C.E., Gopal, S., Schneider, A., Cooper, A., Baccini, A., Gao, F. and C. Schaaf (2002). Global land cover mapping from MODIS: algorithms and early results. *Remote Sensing of Environment*, 83(1–2), 287–302.

Friedl, M.A., Sulla-Menashe, D., Tan, B., Schneider, A., Ramankutty, N., Sibley, A. and X.M. Huang (2010). MODIS Collection 5 global land cover: Algorithm refinements and characterization of new datasets. *Remote Sensing of Environment*, 114(1), 168–182.

Gao, F., J. T. Morisette, R. E. Wolfe, G. Ederer, J. Pedelty, Ed. Masuoka, R. Myneni, B. Tan and J. Nightingale (2008). An Algorithm to Produce Temporally and Spatially Continuous MODIS LAI Time Series, *IEEE Geoscience and Remote Sensing Letters*, 5(1), 60–64.

Griffin, M K, Burke, H K (2003). Compensation of hyperspectral data for atmospheric effects. *Lincoln Laboratory Journal*, 14(1), 29–54.

Hill, M.J., C. Averill, Z. Jiao, C. B. Schaaf, and J. D. Armston (2008). Relationship of MISR RPV parameters and MODIS BRDF shape indicators to surface vegetation patterns in an Australian tropical savanna, *Canadian Journal of Remote Sensing*, 34(Suppl. 2), S247–S267.

Hill, M. J., M. O. Román, C. B. Schaaf (2011a). Dynamics of vegetation indices in tropical and subtropical savannas defined by ecoregions and Moderate Resolution Imaging Spectroradiometer (MODIS) land cover, *Geocarto International*, 1–39, doi:10.1080/10106049.2011.626529.

Hill, M., M. O. Román, C. B. Schaaf, L. Hutley, C. Brannstrom (2011b). Characterizing vegetation cover in global savannas with an annual foliage clumping index derived from the MODIS BRDF product, *Remote Sensing of Environment*, 115, 2008–2024.

Hu, B., W. Lucht, A. Strahler, C. Schaaf, and M. Smith (2000). Surface albedos and angle-corrected NDVI from AVHRR observations of South America, *Remote Sensing of Environment*, 71, 119–132.

Huete, A., Didan, K., Miura, T., Rodriguez, E. P., Gao, X., & Ferreira, L. G. (2002). Overview of the radiometric and biophysical performance of the MODIS vegetation indices. *Remote Sensing of Environment*, 83(1), 195–213.

Huete, A. R., Didan, K., Shimabukuro, Y. E., Ratana, P., Saleska, S. R., Hutya, L. R., Yang, W., Nemani, R and Myneni, R. (2006). Amazon rainforests green-up with sunlight in dry season. *Geophysical Research Letters*, 33(6), L06405.

Jiao, Z., Hill, M. J., Schaaf, C. B., Zhang, H., Wang, Z., & Li, X. (2014). An Anisotropic Flat Index (AFX) to derive BRDF archetypes from MODIS. *Remote Sensing of Environment*, 141, 168–187.

Jin, Y., Gao, F., Schaaf, C. B., Li, X., Strahler, A. H., Bruegge, C. J., & Martonchik, J.V. (2002). Improving MODIS surface BRDF/albedo retrieval with MISR multiangle observations. *IEEE Transactions on Geoscience and Remote Sensing*, 40(7), 1593–1604.

Jin, Y., C. B. Schaaf, C. E. Woodcock, F. Gao, X. Li, A. H. Strahler, W. Lucht, and S. Liang (2003a). Consistency of MODIS surface BRDF/Albedo retrievals: 1. Algorithm performance, *Journal of Geophysical Research*, 108(D5), 4158, doi:10.1029/2002JD002803.

Jin, Y., C. B. Schaaf, C. E. Woodcock, F. Gao, X. Li, A. H. Strahler, W. Lucht, and S. Liang (2003b). Consistency of MODIS surface BRDF/Albedo retrievals: 2. Validation, *Journal of Geophysical Research*, 108(D5), 4159, doi:10.1029/2002JD002804.

Jonsson, P. and L. Eklundh (2002). Seasonality extraction by function fitting to time-series of satellite sensor data, *IEEE Transactions on Geoscience and Remote Sensing*, 40(8), 1824–1832.

Jönsson, P., and L. Eklundh (2004). TIMESAT—a program for analyzing time-series of satellite sensor data. *Computers & Geosciences*, 30(8), 833–845.

Knorr, W., K. G. Schnitzler, and Y. Govaerts (2001). The role of bright desert regions in shaping North African climate. *Geophysical Research Letters*, 28, 3489–3492.

Lacaze, R., & Maignan, F. (2006). POLDER-3/PARASOL Land Surface Algorithms Description. Retrieved from http://smc.cnes.fr/PARASOL/PARASOL_TE_AlgorithmDescription_I3.00.pdf

Lawrence, Peter J., Thomas N. Chase (2007). Representing new MODIS consistent land surface in the Community Land Model (CLM 3.0). *Journal of Geophysical Research: Biogeochemical Cycles*, 112, G01023, doi 10.1029/2006JG000168.

Lawrence, Peter J. and Thomas N. Chase (2009). Climate impacts on the Community Climate System Model (CCSM 3.0) of making the surface hydrology of the Community Land Model (CLM 3.0) consistent with the Simple Biosphere (SiB 2.0). *Journal of Hydrometeorology*, 10(2), 374–394, doi: 10.1175/2008JHM987

Lawrence, P. J., & Chase, T. N. (2010). Investigating the climate impacts of global land cover change in the community climate system model. *International Journal of Climatology*, 30(13), 2066–2087.

Leroy, M., J. L. Deuzé, F. M. Bréon, O. Hautecoeur, M. Herman, J. C. Buriez, D. Tanré, S. Bouffies, P. Chazette, and J. L. Roujean (1997). Retrieval of atmospheric properties and surface bidirectional reflectances over land from POLDER/ADEOS, *Journal of Geophysical Research*, 102, 17023–17037.

Leys, C., et al. (2013). Detecting outliers: Do not use standard deviation around the mean, use absolute deviation around the median. *Journal of Experimental Social Psychology* 49, 746–766. <http://dx.doi.org/10.1016/j.jesp.2013.03.013>.

Li, X., & Strahler, A. H. (1992). Geometric-optical bidirectional reflectance modeling of the discrete crown vegetation canopy: Effect of crown shape and mutual shadowing. *IEEE Transactions on Geoscience and Remote Sensing*, 30(2), 276–292.

Li, X., Gao, F., Wang, J., & Strahler, A. (2001). A priori knowledge accumulation and its application to linear BRDF model inversion. *Journal of Geophysical Research: Atmospheres* (1984–2012), 106(D11), 11925–11935.

Liang, S., Strahler, A., & Walthall, C. (1998, July). Retrieval of land surface albedo from satellite observations: A simulation study. In 1998 IEEE International Geoscience and Remote Sensing Symposium Proceedings, 1998. IGARSS'98. (Vol. 3, 1286–1288). IEEE.

Liang, S. (2000). Narrowband to broadband conversions of land surface albedo I Algorithms. *Remote Sensing of Environment*, 76, 213–238.

Liou, K. N. (1980). *An introduction to atmospheric radiation*. New York: Academic Press.

Lucht, W., Schaaf, C. B., & Strahler, A. H. (2000). An algorithm for the retrieval of albedo from space using semiempirical BRDF models. *IEEE Transactions on Geoscience and Remote Sensing*, 38(2), 977–998.

- Lucht, W., & Lewis, P. (2000). Theoretical noise sensitivity of BRDF and albedo retrieval from the EOS-MODIS and MISR sensors with respect to angular sampling. *International Journal of Remote Sensing*, 21(1), 81–98.
- Maignan, F., F-M. Breon, and R. Lacaze (2004). "Bidirectional reflectance of Earth targets: Evaluation of analytical models using a large set of spaceborne measurements with emphasis on the Hot Spot." *Remote Sensing of Environment* 90(2), 210–220.
- Moody, E. G., M. D. King, S. Platnick, C. B. Schaaf, and F. Gao (2005), Spatially complete global spectral surface albedos: Value-added datasets derived from Terra MODIS land products, *IEEE Transactions on Geoscience and Remote Sensing*, 43, 144–158.
- Moody, E. G., M. D. King, C. B. Schaaf, and S. Platnick (2008). MODIS-Derived Spatially Complete Surface Albedo Products: Spatial and Temporal Pixel Distribution and Zonal Averages, *Journal of Applied Meteorology and Climatology*, 47, 2879–2894.
- Morton, D. C., Nagol, J., Carabajal, C. C., Rosette, J., Palace, M., Cook, B. D., & North, P. R. (2014). Amazon forests maintain consistent canopy structure and greenness during the dry season. *Nature*, 506(7487), 221–4, doi: 10.1038/nature13006.
- Morcrette, J.-J., H. Barker, J. Cole, M. Iacono, and R. Pincus (2008). Impact of a New Radiation Package, McRad, in the ECMWF Integrated Forecasting System, *Monthly Weather Review*, 136, 4773–4798, doi: 10.1175/2008MWR2363.1.
- Myhre, G., Kvalevåg, M. M., & Schaaf, C. B. (2005). Radiative forcing due to anthropogenic vegetation change based on MODIS surface albedo data. *Geophysical Research Letters*, 32(21).
- Myneni, R. B., Yang, W., Nemani, R. R., Huete, A. R., Dickinson, R. E., Knyazikhin, Y., ... & Salomonson, V. V. (2007). Large seasonal swings in leaf area of Amazon rainforests. *Proceedings of the National Academy of Sciences of the United States of America*, 104(12), 4820–4823.
- Nikolakopoulos, K. G., P. I. Tsombos, G. A. Skianis, and D. A. Vaiopoulos (2007). EO-1 Hyperion and ALI bands simulation to Landat 7 ETM+ bands and comparison." In C.M.U. Neale, M. Owe and G. D'Urso, (eds.) *Proceedings of SPIE 6742, Remote Sensing for Agriculture, Ecosystems, and Hydrology IX*, doi:10.1117/12.737941.
- Nikolakopoulos, K. G., Tsombos, P. I., Skianis, G. A., & Vaiopoulos, D. A. (2008, October). EO-1 Hyperion and ALI bands simulation to Landat 7 ETM+ bands for mineral mapping in Milos Island. In *SPIE Remote Sensing* (pp. 711010–711010). International Society for Optics and Photonics.

Oleson, K. W., G. W. Bonan, C. Schaaf, F. Gao, Y.F. Jin, and A. Strahler (2003). Assessment of global climate model land surface albedo using MODIS data, *Geophysical Research Letters*, 30, 1443, doi:10.1029/2002GL016749.

Privette, J. L., Eck, T. F., & Deering, D. W. (1997). Estimating spectral albedo and nadir reflectance through inversion of simple BRDF models with AVHRR/MODIS-like data. *Journal of Geophysical Research: Atmospheres* (1984–2012), 102(D24), 29529–29542.

Rahman, H., Pinty, B. and Verstraete, M.M., (1993). Coupled surface-atmosphere reflectance (CSAR) model 2. Semiempirical surface model usable with NOAA Advanced Very High 93 Resolution Radiometer data. *Journal of Geophysical Research*, 98, 20791–20801.

Restrepo-Coupe, N., da Rocha, H. R., Hutyrá, L. R., da Araujo, A. C., Borma, L. S., Christoffersen, B., ... & Saleska, S. R. (2013). What drives the seasonality of photosynthesis across the Amazon basin? A cross-site analysis of eddy flux tower measurements from the Brasil flux network. *Agricultural and Forest Meteorology*, 182, 128–144.

Roesch, A., C. Schaaf and F. Gao (2004). Use of Moderate-Resolution Imaging Spectroradiometer bidirectional reflectance distribution function products to enhance simulated surface albedos, *Journal of Geophysical Research*, 109, D12105, doi:10.1029/2004JD004552.

Román, M. O., C. B. Schaaf, C. E. Woodcock, A. H. Strahler, X. Yang, R.H. Braswell, P. Curtis, K.J. Davis, D. Dragoni, M. L. Goulden, L. Gu, D. Y. Hollinger, T. E. Kolb, T.P. Meyer, J. W. Munger, J.L. Privette, A.D. Richardson, T.B. Wilson, S. C. Wofsy (2009) The MODIS (Collection V005) BRDF/albedo product: Assessment of spatial representativeness over forested landscapes, *Remote Sensing of Environment*, 113, 2476–2498.

Román, M. O., C. B. Schaaf, P. Lewis, F. Gao, G. P. Anderson, J. L. Privette, A. H. Strahler, C. E. Woodcock, M. Barnsley (2010). Assessing the coupling between surface albedo derived from MODIS and the fraction of diffuse skylight over spatially-characterized landscapes, *Remote Sensing of Environment*, 114, 738–760.

Ross, J. K., *The Radiation Regime and Architecture of Plant Stands*, W. Junk (Ed.). Norwell, MA: Artech House, 1981, p. 392.

Roujean, J. L., Leroy, M., & Deschamps, P. Y. (1992). A bidirectional reflectance model of the Earth's surface for the correction of remote sensing data. *Journal of Geophysical Research: Atmospheres* (1984–2012), 97(D18), 20455–20468.

- Saleska, S. R., Didan, K., Huete, A. R., & Da Rocha, H. R. (2007). Amazon forests green-up during 2005 drought. *Science*, 318(5850), 612–612.
- Salomon, J., C. B. Schaaf, A. H. Strahler, F. Gao, and Y. Jin (2006). Validation of the MODIS bidirectional reflectance distribution function and albedo retrievals using combined observations from the Aqua and Terra platforms, *IEEE Transactions on Geoscience and Remote Sensing*, 44, 1555–1565.
- Samain O. et al. (2006). Spectral normalization and fusion of optical sensors for the retrieval of BRDF and albedo: Application to VEGETATION, MODIS and MERIS datasets, *IEEE Transactions on Geoscience and Remote Sensing* 44 (11): 3166–3179.
- Samanta, A., Ganguly, S., Hashimoto, H., Devadiga, S., Vermote, E., Knyazikhin, Y., Nemani, R and Myneni, R. B. (2010). Amazon forests did not green-up during the 2005 drought. *Geophysical Research Letters*, 37(5).
- Samanta, A., Knyazikhin, Y., Xu, L., Dickinson, R. E., Fu, R., Costa, M. H., & Myneni, R. B. (2012). Seasonal changes in leaf area of Amazon forests from leaf flushing and abscission. *Journal of Geophysical Research: Biogeosciences* (2005–2012), 117(G1).
- Schaaf, C. L., J. Martonchik, B. Pinty, Y. Govaerts, F. Gao, A. Lattanzio, J. Liu, A. H. Strahler, and M. Taberner (2008). Retrieval of Surface Albedo from Satellite Sensors, in *Advances in Land Remote Sensing: System, Modeling, Inversion and Application*, S. Liang (Ed.), Springer: 219–243.
- Schaaf, C. B., F. Gao, A. H. Strahler, W. Lucht, X. Li, T. Tsang, N. C. Strugnell, X. Zhang, Y. Jin, J.-P. Muller, P. Lewis, M. Barnsley, P. Hobson, M. Disney, G. Roberts, M. Dunderdale, C. Doll, R. d'Entremont, B. Hu, S. Liang, and J. L. Privette (2002). First Operational BRDF, Albedo and Nadir Reflectance Products from MODIS, *Remote Sensing of Environment*, 83, 135–148.
- Sombroek, W. (2001). Spatial and temporal patterns of Amazon rainfall: consequences for the planning of agricultural occupation and the protection of primary forests. *AMBIO: A Journal of the Human Environment*, 30(7), 388–396.
- Stroeve, J., J. Box, F. Gao, S. Liang, A. Nolin, C. Schaaf (2005). Accuracy Assessment of the MODIS 16-day Albedo Product for Snow: Comparisons with Greenland in situ Measurements, *Remote Sensing of Environment*, 94, 46–60, doi:10.1016/j.rse.2004.09.001.
- Strugnell, N., W. Lucht, and C. Schaaf (2001). A global albedo data set derived from AVHRR data for use in climate simulations, *Geophysical Research Letters*, 28, 191–194.

- Strugnell, N., and W. Lucht (2001). An algorithm to infer continental-scale albedo from AVHRR data, land cover class and field observations of typical BRDFs, *Journal of Climate*, 14, 1360–1376.
- Tian, Y., R. E. Dickinson, L. Zhou, R. B. Myneni, M. Friedl, C. B. Schaaf, M. Carroll, and F. Gao (2004). Land boundary conditions from MODIS data and consequences for the albedo of a climate model, *Geophysical Research Letters*, 31, L05504, doi:10.1029/2003GL019104
- Twomey, S, *Introduction to the Mathematics of Inversion in Remote Sensing and Indirect Measurement*. New York: Dover, 1977.
- Verhoef W, Bach H. (2003). Simulation of hyperspectral and directional radiance images using coupled biophysical and atmospheric radiative transfer models. *Remote Sensing of Environment*, 87(1), 23–41.
- Vermote, E., Justice, C. O., & Breon, F. M. (2009). Towards a generalized approach for correction of the BRDF effect in MODIS directional reflectances. *IEEE Transactions on Geoscience and Remote Sensing*, 47(3), 898–908.
- Wang, Z., X. Zeng, M. Barlage, R. E. Dickinson, F. Gao, and C. Schaaf (2004). Using MODIS BRDF and Albedo Data to Evaluate Global Model Land Surface Albedo. *Journal of Hydrometeorology*, 5, 3–14.
- Wang, Z., C.B. Schaaf, M.J. Chopping, A.H. Strahler, J. Wang, M.O. Román, A.V. Rocha, C.E. Woodcock, Y. Shuai (2012). Evaluation of Moderate-resolution Imaging Spectroradiometer (MODIS) snow albedo product (MCD43A) over tundra, *Remote Sensing of Environment*, 117, 264–280, 2012.
- Wang, Z., C.B. Schaaf, A.H. Strahler, M.J. Chopping, M.O. Román, Y. Shuai, C.E. Woodcock, D.Y. Hollinger, D.R. Fitzjarrald (2014). Evaluation of MODIS albedo product (MCD43A) over grassland, agriculture and forest surface types during dormant and snow-covered periods. *Remote Sensing of Environment*, 140, 60–77.
- Wanner, W., A.H. Strahler, B. Hu, P. Lewis, J.-P. Muller, X. Li, C.L. Barker Schaaf, and M.J. Barnsley (1997). Global retrieval of bidirectional reflectance and albedo over land from EOS MODIS and MISR data: Theory and algorithm. *Journal of Geophysical Research: Atmospheres*, 102, 17143–17162.
- Wu, A., & Xiong, X. (2012). NPP VIIRS and Aqua MODIS RSB comparison using observations from simultaneous nadir overpasses (SNO). In J.J. Butler, X. Xiong, and X. Gu (eds.) *Proceedings of SPIE 8510, Earth Observing Systems XVII*, 85100P (15 October 2012); doi: 10.1117/12.931011

- Xiao, X., Hagen, S., Zhang, Q., Keller, M., & Moore III, B. (2006). Detecting leaf phenology of seasonally moist tropical forests in South America with multi-temporal MODIS images. *Remote Sensing of Environment*, 103(4), 465–473.
- Zeng, N., Yoon, J. H., Marengo, J. A., Subramaniam, A., Nobre, C. A., Mariotti, A., & Neelin, J. D. (2008). Causes and impacts of the 2005 Amazon drought. *Environmental Research Letters*, 3(1), 014002.
- Zhang, Q. (2009). A global spatially and temporally complete reflectance anisotropy database to improve surface characterization for environmental modeling. Thesis (Ph.D.)-Boston University, Dissertation Abstracts International, Volume: 70-01, Section: B, page: 0180.
- Zhou, L., et al. (2003). Comparison of seasonal and spatial variations of albedos from Moderate-Resolution Imaging Spectroradiometer (MODIS) and Common Land Model, *Journal of Geophysical Research*, 108(D15), 4488, doi:10.1029/2002JD003326.

CURRICULUM VITAE

QINGSONG SUN

(Born in 1982)

Ph. D Candidate, Earth & Environment, Boston University
675 Commonwealth Ave, Rm 406, Boston, MA 02215
857-445-8989, sqs@bu.edu

EDUCATION

2006, B.S, Cartography and GIS, Qingdao Technological University.
2010, M.S, Remote Sensing and GIS, Beijing Normal University.
2010-Present, Geography (Remote Sensing), Boston University

RESEARCH EXPERIENCE

2010 Sept. – Present, Research Assistant
Earth & Environment, Boston University, Boston, MA

2007 Sept. – 2010 Jul, Research Assistant
Geography, Beijing Normal University, Beijing, China

PAPERS / PRESENTATIONS

SUN Qingsong, QU Yonghua, WANG Jindi et al. The Implementation of the OPeNDAP based Remote Sensing Data Distribution System. Remote Sensing Technology and Application, 2010, 25(6): 782-787.

Shuai, Y.; Schaaf, C.; **Sun, Q.**; Wang, Z.; Erb, A.; Masek, J. G. Land Surface 30-m Albedo product by Integrating Landsat & LDCM directional reflectance with MODIS anisotropic information. American Geophysical Union, Fall Meeting 2013, abstract #B41D-0431.

COMPUTER SKILLS

C, C++, Fortran, Python, ENVI, ArcGIS, Matlab.

PROFESSIONAL SOCIETIES

IEEE, Geoscience and Remote Sensing Society.

RESEARCH INTERESTS

I have been working on the gap-filling of the MODIS V005 30 arc second BRDF/Albedo product using temporal fitting techniques, and developing new Narrow to Broad band conversion parameters based on satellite data. I am also interested in combining MODIS with MISR, and MODIS with VIIRS to improve BRDF retrievals.